A SEARCH FOR DARK MATTER WITH THE ZEPLIN II DETECTOR

A Dissertation

by

JIANTING GAO

Submitted to the Office of Graduate Studies of
Texas A&M University
in partial fulfillment of the requirements for the degree of

DOCTOR OF PHILOSOPHY

August 2009

Major Subject: Physics

A SEARCH FOR DARK MATTER WITH THE ZEPLIN II DETECTOR

A Dissertation

by

JIANTING GAO

Submitted to the Office of Graduate Studies of
Texas A&M University
in partial fulfillment of the requirements for the degree of

DOCTOR OF PHILOSOPHY

Approved by:

Chair of Committee,	James T. White
Committee Members,	Richard L. Arnowitt
	Leslie A. Braby
	Robert C. Webb
Head of Department,	Edward Fry

August 2009

Major Subject: Physics

ABSTRACT

A Search for Dark Matter with the ZEPLIN II Detector. (August 2009)

Jianting Gao, B.S., Nanjing University;

M.S., Institute of High Energy Physics, Chinese Academy of Sciences

Chair of Advisory Committee: Dr. James T. White

Galaxies and clusters of galaxies are believed to be dominated by non-luminous non-baryonic dark matter. A favored candidate is a new type of Weakly Interacting Massive Particle (WIMP) with a mass of order 100 GeV/c^2. The ZEPLIN II experiment is a WIMP search experiment that attempts to directly detect WIMP interactions using the two-phase xenon approach. The detector measures both scintillation and ionization generated by interactions in a 31 kg liquid xenon target. This approach provides a powerful discrimination between nuclear recoils, as expected from WIMPs, and background electron recoils.

In this work, we develop a new $\chi 2$ approach to determine the three dimensional event positions in an attempt to improve the background rejection. The optical properties of the PTFE reflectors and the grids of the detector were determined using the Geant4 simulation, and event positions were obtained by finding the best match to the amount of light in each photomultiplier. This was found to greatly improve the position resolution.

The approach was then applied to the WIMP search data. It was found that one of the dominating background sources was events from the gas above the anode grid and not from the PTFE walls caused by the small signals as previously thought. WIMP

search results were then obtained from the first 31 days of stable ZEPLIN II data using two methods. Although the $\chi 2$ method greatly improved position resolution, the number of background events was not significantly altered and the new limit agreed well with the limit published by the collaboration.

ACKNOWLEDGEMENTS

I would like to thank Dr. James T. White, my dissertation advisor, for his guidance and encouragement. This study would never be possible without his support, insightful talks and important help in writing the dissertation. I am also thankful to Dr. Bhaskar Dutta for his wonderful lectures on Quantum Field Theory and other committee members, Dr. Richard Arnowitt, Dr. Leslie A. Braby, and Dr. Robert C. Webb, for their interest and patience.

I owe many thanks to the ZEPLIN II collaboration. It was a pleasure to discuss data analysis with Barbara Camanzi, data acquisition with Mike J. Carson, detailed data reduction with Matthew Robison, and detector construction and performance with Dr. Hanguo Wang. I also wish to thank Dr. Nigel J.T. Smith for his leadership.

I would like to thank fellow graduate students in the physics department of Texas A&M University, Lijun Qin, Xinfeng Chen, Ty Stiegler, and Dr. Zhiqiang Chen, for their help in data analysis tools and Geant4 simulation. Thanks also go to undergraduate students Gabe Salinas and Robert Blessitt for the detailed description of detector construction and study of PTFE materials.

I am so grateful to Sandi Smith, Senior Academic Advisor I of the Physics Department, and ISS advisors Amanda Brinlee, Katy Britton, Eunice Overton, Bill Taylor and other faculty and staff for making my time at Texas A&M University a great experience.

Finally, I would like to thank my wife Lili Zeng and my parents for their support, encouragement, and patience during all the years.

TABLE OF CONTENTS

CHAPTER Page

Page

LIST OF FIGURES

FIGURE Page

FIGURE Page

LIST OF TABLES

CHAPTER I

INTRODUCTION

A. Introduction

Einstein's theory of General Relativity forms the basis of modern cosmology. The theory may be summarized in these terms: spacetime is a manifold on which there is defined a metric $g_{\mu\nu}$. The curvature of spacetime is related to the matter and energy distribution in the Einstein equations:

$$G_{\mu\nu} \equiv R_{\mu\nu} - \tfrac{1}{2} R g_{\mu\nu} = 8\pi G T_{\mu\nu} \tag{1.1}$$

where $G_{\mu\nu}$ is the Einstein tensor, $R_{\mu\nu}$ is the Ricci tensor associated with the metric $g_{\mu\nu}$, R is the scalar curvature, defined as the trace of $R_{\mu\nu}$, G is the gravitational constant, and $T_{\mu\nu}$ is the stress tensor of matter in the universe. Recent observations indicate that a cosmological constant identified with a non-zero vacuum energy density has to be present:

$$G_{\mu\nu} = 8\pi G T_{\mu\nu} + \Lambda g_{\mu\nu} \tag{1.2}$$

We assume the Universe is homogeneous and isotropic. The spacetime metric takes the form depending on three spatial geometries:

$$ds^2 = dt^2 - a^2(t)\begin{cases} d\psi^2 + \sin^2\psi(d\theta^2 + \sin^2\theta d\phi^2) & \textit{SPHERE} \\ d\psi^2 + \psi^2(d\theta^2 + \sin^2\theta d\phi^2) & \textit{FLAT} \\ d\psi^2 + \sinh^2\psi(d\theta^2 + \sin^2\theta d\phi^2) & \textit{HYPERBOLOIDS} \end{cases} \tag{1.3}$$

This dissertation follows the style of Physical Review D.

where a is the scale factor, t is time, and (ψ, θ, ϕ) are spherical coordinates.

The metric can be expressed in the form:

$$ds^2 = dt^2 - a^2(t)\left[\frac{dr^2}{1-kr^2} + r^2\left(d\theta^2 + \sin^2\theta d\phi^2\right)\right] \tag{1.4}$$

where k = -1, 0, or 1 for open, flat or closed geometry, respectively. This metric is called the Friedmann-Robertson-Walker metric; (t, r, θ, ϕ) are comoving coordinates. Since $ds^2 = \sum_{\mu\nu} g_{\mu\nu} dx^\mu dx^\nu$, $g_{\mu\nu}$ is symmetric. Assuming the stress tensor takes the perfect fluid form, the Einstein field equation for this metric gives rise to the Friedmann equations:

$$\frac{\dot{a}^2}{a^2} + \frac{k}{a^2} - \frac{\Lambda}{3} = \frac{8\pi G\rho}{3} \tag{1.5}$$

$$2\frac{\ddot{a}}{a} + \frac{\dot{a}^2}{a^2} + \frac{k}{a^2} - \Lambda = -8\pi G p \tag{1.6}$$

where ρ is the mass density of matter and p is the pressure of matter and energy. Using equation (1.5), we may rewrite equation (1.6) as:

$$3\frac{\ddot{a}}{a} = -4\pi G(\rho + 3p) + \Lambda \tag{1.7}$$

Equations (1.5) and (1.7) are the general evolution equations for a homogenous and isotropic cosmology. We need to know initial values and boundary conditions from cosmological observations to solve the equations.

The key to understanding the universe is Hubble's law:

$$v = Hr \tag{1.8}$$

where *v*, *r* are the velocity of recession and the distance between two isotropic observers, and $H = \dot{a}/a$, is Hubble parameter. Hubble's law indicates the Universe is expanding. Equation (1.7) shows how matter slows down the expansion of the Universe while the cosmological constant accelerates it. Define the critical density

$$\rho_c = \frac{3H_0^2}{8\pi G} \tag{1.9}$$

where H_0 is the present day value of Hubble parameter. The density can be written as:

$$\rho = \frac{3H_0^2}{8\pi G}\left[\Omega_r\left(\frac{a_0}{a}\right)^4 + \Omega_m\left(\frac{a_0}{a}\right)^3 + \Omega_\Lambda\right] \tag{1.10}$$

where a_0 is the present day value of the scale parameter; Ω_r, Ω_m, and Ω_Λ are the fractions of the critical energy density for radiation, matter and vacuum energy, respectively. It shows that at early stage of the Universe when *a* was small the radiation density dominates the expansion of the Universe. The Firedmann equation can be rewritten as:

$$k/a_0^2 = H_0^2\left(\Omega_r + \Omega_m + \Omega_\Lambda - 1\right) \tag{1.11}$$

The density of the cosmic microwave radiation background (CMB) is $\sim a_B T^4$, with the CMB temperature T = 2.725 K. The total energy density in radiation is negligible compared to the critical mass density. Equation (1.11) reduces to:

$$\Omega_m + \Omega_k + \Omega_\Lambda = 1 \tag{1.12}$$

$$\Omega_k = \frac{-k}{a_0^2 H_0^2} \tag{1.13}$$

Hence, evolution of the Universe is determined by the two parameters Ω_m and Ω_Λ. The total matter/energy density $\Omega = \Omega_m + \Omega_\Lambda = 1$ for a flat universe; $\Omega > 1$ for a closed universe and $\Omega < 1$ for an open universe.

Our current picture of the Universe is that the Universe is very close to flat; about 73% of the content of the Universe is dark energy, associated with Ω_Λ; while the matter content is about 27% (Ω_m). The baryonic matter density Ω_b is about 0.044 and the luminous component Ω_{lum} makes up only 0.005. The striking result is that most of the matter and energy in the Universe is exotic and non-luminous. The experimental observations pointing to this conclusion will be presented in subsequent sections.

B. Observational Evidences for Existence of Dark Matter

1. Clusters of Galaxies

The existence of the unseen matter is revealed by gravitational effects. The dark matter hypothesis was first invoked by Fritz Zwicky in 1933. Zwicky estimated the velocities of outlying galaxies in the Coma Cluster and found the dispersion to be 1000 km/sec. He also estimated the masses of the galaxies in the cluster based on their light and added them up to get a total cluster mass. Then he applied the virial theorem to check the total mass in an independent way.

a. Virial Theorem

The virial theorem states that for a statistically steady, self-gravitating cluster of objects (stars or galaxies), the total kinetic energy equals to -1/2 of the total gravitational potential energy. For N objects of mass m with average distance r and typical random velocity v, the gravitational potential energy of each pair is $-Gm^2/r$. There are $N(N\text{-}1)/2$

possible pairings, thus the total gravitational potential energy is $-GN(N\text{-}1)m^2/2r$. The virial theorem can be written as

$$Nmv^2/2 = GN(N-1)m^2/4r \tag{1.14}$$

For N>>1, the total mass M of a rich spherical cluster of galaxies can be determined by

$$M = 2rv^2/G \tag{1.15}$$

It was found that the cluster required about 10 times more mass than the obseverd optically luminous matter to bind the galaxies. Thus there must be more matter out there in the cluster than visible matter.

b. Gravitational Lensing

The application of virial theorem above requires the assumptions of symmetry and equilibrium, which are not exactly true. To learn how much mass the galaxies actually contained, one can search for gravitational lensing effects, which do not rely on the understanding of the dynamics in the clusters. When light from a distant galaxy passes through a cluster of galaxies it is deflected by the gravitational field and images of the distant galaxies are distorted into curving arcs. The amount of the distortion depends on the mass of the cluster (the lens) and on the relative positions of the lens and the distant galaxy. The observer may see multiple and strongly distorted images, single distorted images with elliptical shape, or weakly distorted images with almost invisible individual elongation. Clowe *et al.* reconstructed the mass of the interacting cluster 1E 0657-558 from weak lensing effect [1]. They found the mass-to-light ratio $M/L_B > 200$ $M_\odot/L_\odot$, where L_B is the rest frame B luminosity, $M_\odot$ and $L_\odot$ are the mass and luminosity of the sun. Since stars typically have a mass-to-light ratio less than 10 $M_\odot/L_\odot$, it implies

a large fraction of the matter in the cluster does not emit visible light, hence the existence of dark matter.

c. X-ray

X-ray studies have revealed that the distribution of X-ray sources is spatially extended and the spectra are most consistent with thermal bremsstrahlung from hot gas. Hence there exist large amounts of hot gas with temperatures between 10^7 K -10^8 K (1 - 10 keV) and low density (10^{-2}-10^{-4} atoms/cm^3) between the galaxies in rich clusters. The intra-cluster gas is assumed to be at hydrostatic equilibrium with surface brightness and density [2]

$$I(r) \propto \left[1+\left(\frac{r}{r_c}\right)^2\right]^{-3\beta+1/2} \tag{1.16}$$

$$\rho_g(r) \propto \left[1+\left(\frac{r}{r_x}\right)^2\right]^{-3/2} \tag{1.17}$$

where r is the radius from the cluster center, r_c is the core radius of the cluster, r_x is the X-ray core radius and β is the galaxy-to-gas velocity dispersion

$$\beta \equiv \frac{\mu m_p \sigma_r^2}{kT_g} \tag{1.18}$$

where μ is the mean molecular weight in amu, μ = 0.63 if solar abundances are assumed, m_p is the proton mass, σ_r is the one-dimensional velocity dispersion, T_g is the gas temperature. The self-gravitating isothermal model has the same surface brightness distribution if one takes β = 1 and $r_c = r_x$. The equation of hydrostatic equilibrium is

$$\nabla P = -\rho_g \nabla \phi(r) \tag{1.19}$$

where $P = \rho_g kT_g/\mu m_p = nkT_g$ is the pressure, and $\varphi(r)$ is the gravitational potential of the cluster. For spherically symmetric cluster equation (1.19) is reduced to

$$\frac{1}{\rho_g}\frac{dP}{dr} = -\frac{d\phi}{dr} = -\frac{GM(r)}{r^2} \tag{1.20}$$

where *M(r)* is the total cluster mass within *r*.

$$M(r) = -\frac{rkT_g}{G\mu m_p}\frac{d\ln(nT_g)}{d\ln r} \tag{1.21}$$

The cluster mass can be determined if the density and temperature of the intracluster gas are known. The mass depends mainly on the gas temperature, but only weakly on the gas density. Girardi *et al* evaluated in a homogeneous way the optical masses of 170 nearby clusters and computed the mass of each cluster by applying the virial theorem to the member galaxies [3]. After rescaling to the X-ray radii, the optical mass estimates were compared to those derived from X-ray analyses compiled from the literature (for 66 clusters) [4]. Girardi *et al.* found good overall agreement between the two methods.

2. Galaxies

a. Spiral Galaxies

Existence of dark matter is strongly supported by the study of rotation curves of spiral galaxies. The rotation curve is a graph that plots the orbital velocity of the stars and gas clouds in the galaxy on the y-axis against the distance from the center of the galaxy on the x-axis. The velocity is measured using the red-shift of atomic lines for stars or the 21 cm line for the hydrogen clouds. The circular velocity is given by

$$v(r) = \sqrt{\frac{GM(r)}{r}} \tag{1.22}$$

where *M(r)* is the galactic mass within *r*,

$$v(r) \propto \begin{cases} r & if\ \ M(r) \propto r^3 (uniform) \\ 1/\sqrt{r} & if\ \ M(r)\ is\ const.(core) \\ cons\tan t & if\ \ M(r) \propto r(halo) \end{cases} \qquad (1.23)$$

Beyond the luminous matter distribution it was expected that the orbital velocity would decline as the distance from the galaxy center increase ($v(r) \propto 1/\sqrt{r}$) if visible matter is the dominant component of the galaxy. However it is well know that rotation curves (RCs) of spiral galaxies do not show any fall-off feature [5-7]. Persic, Salucci, and Stel investigated about 1100 RCs of spiral galaxies, over a range of 6 mag (absolute magnitudes from -16 to -22) and out to 1.5-2 optical radii[8]. They found that a single global parameter, luminosity, determines the profile and the amplitude of RCs, resulting in the existence of a universal RC. The most natural explanation to the flattening out of the RC at large distance is the presence of an additional and non-luminous mass halo in the galaxy.

b. Elliptical Galaxies

Elliptical galaxies are smooth and elliptical in appearance. They have much more random star motion than orderly rotational motion. Similarly to the cluster of galaxies, the mass of an elliptical galaxy can be estimated from the temperature of the X-rays emitted by the gases surrounding the galaxy, assuming the hydrostatic equilibrium. Loewenstein and White observed β_{spec}, defined in equation (1.18), was typically ~0.5, implying the stars have 1/2 the velocity dispersion they should have. They inferred that dark matter is an extremely common constituent of elliptical galaxies [9].

Our galaxy, the Milky Way Galaxy, as a typical spiral galaxy, shows that the orbital velocities do not decrease at greater distances. If most of the mass is concentrated within the orbit of the sun as the luminous matter is, then one would expect to see Keplerian motion at distance larger than 8.5 kpc, the orbital radius of the sun. The flatness of the curve at large radii implies the existence of an unseen dark halo in our galaxy [10].

3. Large Scale Structure

The large scale structure of the universe and microwave background radiation provides further evidence that dark matter exists not only in certain galaxies and clusters of galaxies, but also throughout the universe. Since the discovery of the largest structure of cosmos, the “Great Wall”, by Margaret Geller and John Huchra based on a redshift survey in 1989 [11]. The structure of the universe has now been mapped extensively as is seem to contain large narrow filaments and walls separated by giant voids that are nearly empty of galaxies (Fig. 1). However, observations made by the Cosmic Background Explorer (COBE) project indicate that the cosmic microwave background radiation is almost the same in all directions [12-14]. The isotropy of cosmic microwave background radiation (CMBR) was confirmed later by the Wilkinson Microwave Anisotropy Probe (WMAP) data [15]. CMBR is evidence that big bang did occur and matter was once distributed highly uniform in the universe. Study of N-body simulations reveals that fluctuations of density can cause matter to clump together and the evolution epoch of the system depends on the density of the matter [16]. Structure formation of the universe from a highly uniform state to the large filaments and voids we observe today

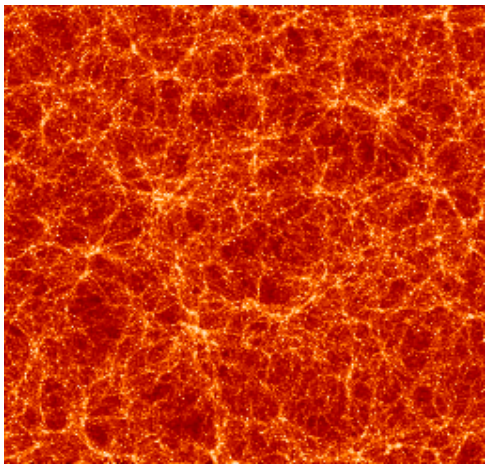

Figure 1: Density plot of N-body simulation [16].

implies the matter density of the universe to be $\Omega \approx 0.3$ [17]. This is much larger than the luminous density of spiral galaxies with $\Omega \approx 0.01$ and thus larger than the density of visible matter in the whole universe. This is evidence that dark matter dominates the mass of the universe.

C. Dark Matter Candidates

The nature of dark matter is as yet unknown. Although huge hydrogen clouds, black holes, and neutron stars in the galaxies do not emit visible light, they cannot be the "dark" matter. Hydrogen clouds emit 21 cm radiation from electron spin flip and are therefore observable. Also the X-rays emitted from black holes and neutron stars are easily detected and surveys show that there cannot be enough matter in this form to account for dark matter. Massive compact halo objects (MACHOs) such as low mass stars, brown dwarfs or planets can be detected by a micro lensing effect. The MACHO project has searched for MACHOs in the direction toward the Milky Way Galaxy bulge

and found no evidence for enough brown dwarfs to make up a significant part of the dark matter [18].

It turns out that ordinary baryonic matter in any form is not sufficient to account for dark matter in the scale of galaxies and clusters of galaxies. It is possible to estimate the baryon density in the universe today using Big Bang nucleosynthesis [19]. The neutrons and protons started to form deuterium when the temperature of the universe dropped to10^9 K, and deuterium further build up helium-4. The process chain ended there because the lack of stable nuclei with atomic weight of 5 and the rapid decline of baryon density. The ratio of deuterium to hydrogen could not change after the end of nucleosynthesis and its value depended on the baryon density. By measuring the fraction of deuterium in the galaxy today, the baryon density at a temperature of 10^9 K can be calculated. Applying the conservation of baryon number ($\rho(T) / T^3 = \text{const}$), it's straightforward to find the baryon density at current universe temperature $T \approx 2.735$ K [20]. This consideration gives baryon density $\rho_b = 5\times10^{-31}$ gm/cm^3. The critical density is $\rho_c = 1.88h^2\times10^{-29}$ g/cm^3, where h parameterizes the Hubble constant, $H_0 = 100$ h km/s/Mpc. The most recent result of H_0 was obtained from WMAP in 2003, $H_0 = 71 \pm 4$ km/s/Mpc [21]. Therefor $\rho_c \approx 9.5\times10^{-30}$ gm/cm^3, which is much larger than ρ_b.

Thus the cosmological baryonic density of the university today is $\Omega_b \approx 0.05$, too small to account for the non-luminous dark matter ($\Omega \leq 0.3$). Among the non-baryonic dark matter candidates, light neutrinos, sometimes referred to as hot dark matter (HDM), move too fast to clump together on galactic scales to stimulate the formation of galaxies and clusters of galaxies. Thus, dark matter is best explained as cold dark matter (CDM).

Axions and weakly interacting massive particles (WIMPs) are the most favored CDM candidates. The axion is a hypothetical boson proposed to explain the absence of an electrical dipole moment for the neutron [22]. The experimental method of detecting axions is made through conversion of axions to microwave photons in a strong magnetic field. One detector based on this idea, the Axion Dark Matter Experiment (ADMX), is carrying out a search for axions [23], and recent results indicate that the mass of axion is constrained to be less than 10^{-5} eV [24]. The most promising candidate to solve the dark matter problem is the WIMP. Having a large mass, such a particle would be slow moving, and N-body simulations with such objects produces structure similar to what has been observed. WIMP constitutes an entire class of candidates predicted by theories that extend beyond the Standard Model. The stable lightest supersymmetric particle (LSP), neutralino, is an ideally motivated WIMP candidate. They are predicted to be stable particles with masses in the range 10 GeV to a few TeV and interact with matter only though weak and gravitational interactions. The direct detection of such WIMPs could provide strong evidence for the existence of supersymmetry and lead to a better understanding of the dynamics of dark matter halo in our galaxy as well.

D. Direct WIMP Detection

It may be possible to experimentally detect WIMPs via WIMP-nucleus elastic scattering. The Milky Way galaxy, as a typical spiral galaxy, contains ~10 times more dark matter than luminous matter [25]. The motion of the Sun and the Earth with respect to the galaxy are shown in Fig. 2. The velocity distribution and density of WIMPs passing near the Earth is halo model dependent, but the standard Maxwellian halo model

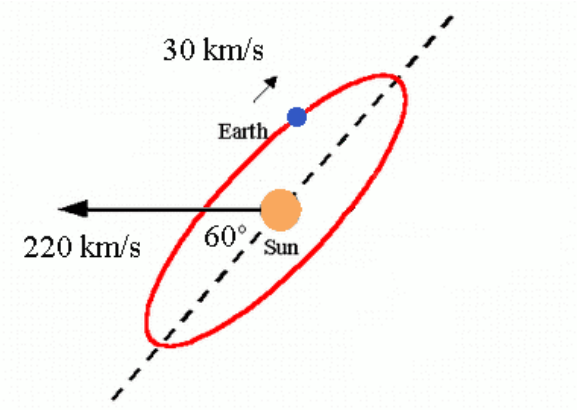

Figure 2: The motion of the Sun and the Earth with respect to the galaxy. The Earth is orbiting around the Sun with 60^o tilt from the galactic plane.

assumes a spherical and isotropic distribution of WIMPs with flux proportional to $1/r^2$, where r is the distance to the galactic center. A simple estimation of the density of WIMPs based on the standard halo model yields the average density $\rho_o \approx 0.3$ GeV/cm^3 [26]. These WIMPs will occasionally scatter elastically off nuclei producing nuclear recoils with energy E_r in the range ≤100 keV. The recoil rate per nucleus depends on the density ρ_o and the velocity distribution f(v) of WIMPs near the Earth: $R \approx n\sigma\langle v\rangle$, where the WIMP number density $n = \rho_o/m_x$, m_x is mass of WIMP particle, σ is the elastic scattering cross section, and <v> is the average speed of the WIMP near the Earth. It is of experimental interest to know the nuclear recoil spectrum from WIMP elastic scattering $\frac{dR}{dE_R} \propto \sigma\rho_0 \int_{v_{\min}}^{\infty} \frac{f(v)}{v} dv$, where $v_{\min} = \left(\frac{(m_x + m_N)^2}{2m_x^2 m_N} E_r \right)^{1/2}$ is the minimal velocity to produce detectable recoil energy. In the halo model of Maxwellian distribution, the recoil spectrum can be further written as [27]:

$$\frac{dR}{dE_R} = \frac{\sigma_0 \rho_0}{4 v_e m_x m_r^2} F^2(E_R) \left[erf\left(\frac{v_{\min} + v_e}{v_0} \right) - erf\left(\frac{v_{\min} - v_e}{v_0} \right) \right] \tag{1.24}$$

where $m_r = m_N m_x / (m_N + m_x)$ is the reduced mass, v_e and v_0 are Earth velocity and Sun velocity with respect to galactic center, separately, $F(E_R)$ is the nuclear form factor, and σ_0 is the cross section at zero momentum transfer. σ_{0spin} is much smaller than $\sigma_{0scalar}$ for a target nucleus with A > 20, so $\sigma_0 \approx \sigma_{0scalar}$. $\sigma_{0scakar} = \frac{4 m_r^2}{\pi} \left[Z f_p + (A - Z) f_n \right]^2$, where f_p and f_n are effective couplings of neutralinos to protons and neutrons, and Z is the atomic number of the target nuclei. In most cases $f_p \approx f_n$, so $\sigma_{0scalar} \propto m_r^2 A^2$. The form factor suggested by Engel [28] is:

$$F(E_R) = \left[\frac{3 j_1(q R_1)}{q R_1} \right]^2 \exp\left[-(qs)^2 \right] \tag{1.25}$$

where j_1 is a spherical Bessel function $q = \sqrt{2 m_r E_R}$ is the momentum transfer, $R_1 = \left(R^2 - 5 s^2 \right)^{1/2}$, $R \approx 1.2 A^{1/3}$ fm, and s≈1 fm. Figure 3 is an example of nuclear recoil spectra in xenon from WIMP with masses of 50 and 100 GeV. It shows that in xenon most of the recoils have transfer energies less than 50 keV because of the form factor.

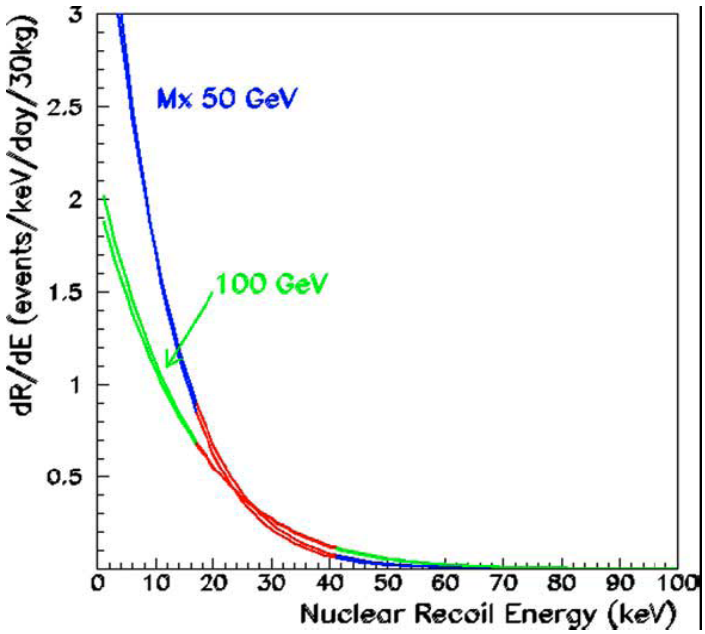

Figure 3: Nuclear recoil spectra from WIMP with masses of 50 and 100 GeV.

E. WIMP Detection Experiments

In models in which R-parity ($R=(-1)^{3(B-L)+2S}$, with baryon number B, lepton number L and spin S) is conserved the lightest supersymmetric particle (LSP) is stable. In the minimal supersymmetric model (MSSM), the LSP is the lightest neutralino, a linear combination of the SUSY partner of the Z boson (zino), the photon (photino), and the neutral higgs (higgsino). While a WIMP has not yet been detected experimentally, there is a general agreement that the LSP, as a natural WIMP dark matter candidate, can be either detected directly by studying the WIMPs scattering off ordinary atoms or by indirect detection methods that search for the signals from WIMP annihilation.

1. Indirect Detection Experiments

The neutralino is a Majorana particle and therefore its own antiparticle, thus

WIMPs annihilate each other. The annihilation rate is proportional to the square of the WIMP density, since the process requires two WIMPs. There are a number of WIMP annihilation channels, among which $\chi\chi \rightarrow f\bar{f}$, $\chi\chi \rightarrow Z\gamma$, $\chi\chi \rightarrow \gamma\gamma$, $\chi\chi \rightarrow \nu\nu$ can be used to probe the WIMP, since the decay products (gamma γ, neutrinos ν, and antiparticle such as positrons and antiprotons) can reach us to be detected and are distinguishable from background events of the same type either by using peculiar spectrum or locating the place where WIMP annihilations occur. Indirect searches for WIMP can be categorized based on the products of WIMP pair annihilations.

a. Neutrinos

As WIMPs pass through a large celestial body, such as the Sun and the Earth, they can scatter off nuclei in there, losing energy. If the velocity of a WIMP falls below the escape velocity, it becomes gravitationally bound to the body. This WIMP will undergo more scatterings and lose its kinetic energy gradually, thus WIMPs will accumulate in the core of the Sun and the Earth until the rate of capture equals twice the rate of annihilation. Since the WIMP annihilation rate $\propto \rho_{\chi}^{2}$, the enhancement of density increases the possibility of finding WIMPs. Detectable neutrino rates from the Earth and Sun are expected to be much larger than from the galactic center because of the solid angle. When WIMPs annihilate at the center of the Earth and Sun, the majority of the annihilation products are absorbed immediately except the neutrinos. The mean neutrino energy ranges from 1/3 to 1/2 the mass of the WIMP. Among the known three neutrino flavors, only the muon neutrino is of interest for indirect detection. Electron neutrinos would be undetectable because electrons are easily stopped in ordinary matter; Tau

neutrinos are produced much less abundantly than muon neutrinos, for the production rates are greatly suppressed by the mass of the tau.

The muon neutrinos could undergo charged-current interaction in the rock around the detector producing muons, which are well collimated with the incident neutrino direction (mean deviation angle = $0.7^{\circ} \times (E_{\nu}/\mathrm{TeV})^{-0.7}$ [29]) and have much of the neutrino energy (a few GeVs). Thus, one can search for the upward-going muon signal with a high energy threshold. The neutrinos from WIMP annihilation in the Sun are easily discriminated from the solar neutrinos which have energies of the order MeVs. The mainly known background come from atmospheric neutrinos produced by cosmic rays on the opposite side of the Earth. The excess of neutrinos from the Earth or the Sun has been searched by a number of experiments world wide.

Baksan

The Baksan [30] Neutrino Observatory (BNO) is situated in the Baksan gorge in the Caucasus, Russia. It has a Baksan Underground Scintillation Telescope located 300 m below the surface and a Gallium-Germanium Neutrino Telescope 3,500 m deep. The Lithium-Beryllium and Chlorine-Argon Neutrino Telescopes are under construction.

MACRO

The MACRO (Monopole, Astrophysics and Cosmic Ray Observatory) [31] was located in the Gran Sasso Underground Laboratory (depth 3,800 mwe) of the Italian Istituto Nazionale di Fisica Nucleare (INFN) in Italy. The detector contains streamer tube system for tracking and roughly 600 tons of liquid scintillator for timing. It has

angular resolution ~0.5° and time resolution ~0.5ns. The overall dimensions of the detector are 12 m$\times$77 m$\times$9 m consisting six units referred to as “supermodules”, each of which can operate while other parts modules are under construction. The threshold for vertical muons crossing the detector is about 1 GeV.

Super-Kamiokande

The super-Kamiokande [32] is a neutrino observatory designed to search for proton decay and study for atmospheric and solar neutrinos. The detector is a 50,000 ton pure water Cherenkov detector, located in the Kamioka-Mozumi mine in Japan with 1000 m rock overburden. The 41.4m tall and 39.3m across sylindrical water is surrounded by about 11,200 photomultiplier tubes. The effective detector area for upward through-going muons is ~1200 m^2. The muons are required to have at least 7 meters measured track length in the water, corresponding to a threshold of 1.6 GeV.

Amanda II

The Amanda II [33] detector contains 677 optical modules attached to 19 strings located between 1500 m and 2000 m under the South Pole ice cap. The optical module is a glass pressure vessel with a photomultiplier tube inside. The strings are arranged in three concentric circles with radius of 30 m, 60 m and 100 m, respectively. Cherenkov light created by muons passing through the nearby ice can be detected with at least 24 modules were hit with a time window of 2.5 μs.

Up to now, none of the experiments has observed excess of muon-neutrinos from WIMP annihilations in the Earth or the Sun. The AMANDA II has the potential to improve the sensitivity to the WIMP annihilation neutrinos by two orders of magnitude.

b. Gamma Rays

Gamma rays can be produced by WIMP annihilation via $\chi\chi \rightarrow Z\gamma$ and $\chi\chi \rightarrow \gamma\gamma$. Because of the non-relativistic nature of WIMPs as discussed in Chapter I, the gamma rays are monoenergetic, with $E_\gamma = M_\chi$ or $E_\gamma = M_\chi(1\text{-}M_Z^2/4\ M_\chi^2)$ for $\chi\chi \rightarrow \gamma\gamma$ or $\chi\chi \rightarrow Z\gamma$, respectively. Thus searching for these gamma lines (tens to hundreds of GeV) from galactic center can be used to detect theWIMPs. The gamma ray flux may be detected by space-based detectors such as EGRET or ground-based atmospheric Cherenkov telescopes that detect Cherenkov light emitted by the the air shower produced by the gamma ray. However, none of the ground-based experiments is ideal for WIMP search. Because of one or more of the below reasons: poor energy resolution of order 30%; incapability of distinguishing showers caused by gamma rays or cosmic rays; constraints of looking at gamma rays from the galactic center.

The satellite based EGRET (Energetic Gamma Ray Experiment Telescope) experiment has identified an excess of gamma-ray at the galactic center [34]. The spectral features of this gamma-ray source were pointed out to be compatible with the WIMP-induced gamma-ray. However, G. Zaharijas and D. Hooper have showed a bright astrophysical gamma source has recently discovered in the region of the galactic center. This source constitutes a significant background and puts a constraint on the detection of WIMP in the galactic center [35].

The GLAST (the Gamma-ray Large Area Space Telescope), as a next generation high-energy gamma-ray observatory following the EGRET experiment, is designed to observe gamma rays in the energy band from 10 MeV to 100 GeV. GLAST employs a

CsI(Tl) based calorimeter and silicon-strip detectors that can precisely track the electron or positron purduced from the gamma ray, hence is expected to have better energy and angular resolutions than EGRET.

c. Cosmic Antimatter

The antimatter produced in WIMP annihilation, mainly anti-protons and positrons, is sought to be detected by balloon or space based experiments, for the background flux is small. Antiprotons have been searched by the balloon-based experiment BESS (Balloon-borne Experiment with a Superconducting Spectrometer) experiment and the flux of positrons has been searched by the HEAT (High Energy Antimatter Telescope) experiment [36-37]. However the source of the protons is yet unknown, and it is unclear if antiproton flux measurement will constrain WIMP models due to the large uncertainties on the production and propagation of secondary anti-protons [38].

2. Direct Detection Experiments

Direct detections look for signals from the WIMP-nucleon elastic scattering. There are a number of experiments underway to detect the neutralino through the nuclear recoils from ordinary matter. Due to the low event rate as showed in Chapter I, these experiments are carried out in deep underground to obtain low background rate. Direct detection experiments are categorized either by the detection media, such as NaI, germanium, xenon and argon, or whether using event by event discrimination. Two major experiments, for example, are DAMA and CDMS.

a. **DAMA**

The DAMA (DArk MAtter) experiment at Gran Sasso of the INFN Italy uses 100 kg NaI(Tl) as the detection target. This experiment has a first claim of a possible discovery of WIMP dark matter after a few years running (from 1995 to 2002 for a total exposure of ~ 1.08×10^5 kg-days) [39]. Their approach was to detect an annual modulation signature based on the seasonal event rate variation caused by the Earth's motion around the sun. A cosine fitting can be imposed on the event rate plotted as a function of time. The significance of the modulation is 6.3 σ and the period is one year. The residual rate reaches its maximum in June and minimum in December with a fluctuation of ±1.6%. Background discrimination is done through pulse shape discrimination, which is not effective for low energies on an event by event basis but can be exploited on a statistical basis. The problem with DAMA result is that it contains all possible unfiltered background events such as gammas and betas, and furthermore, the result has been disputed by other experiments such as CDMS and Edelweiss, so the DAMA result is not yet accepted as a definite WIMP signal.

b. CDMS

The CDMS (Cryogenic Dark Matter Search) experiment uses germanium and silicon crystals in its dark matter search. Ge (250 g) is used for the WIMP target, while Si (100 g) for neutron background estimation. The sizes of the cylindrical crystals are 1 cm thick and 7.6 cm in diameter. The detector records both phonon and ionization signals produced from the nucleon-WIMP collision and can identify particles on an event by event basis. The sensitivity of the detector is compatible with the DAMA

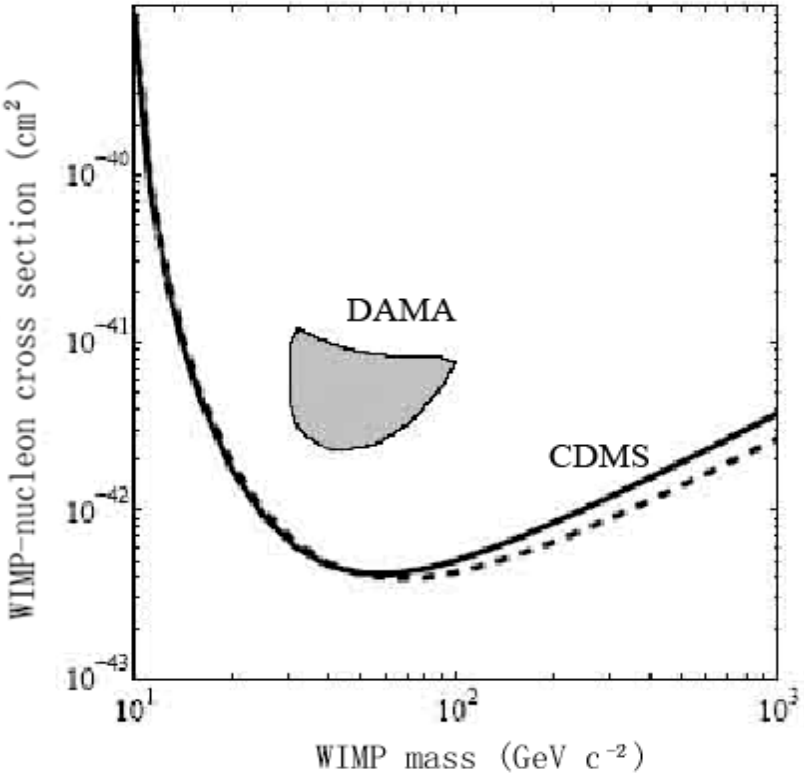

Figure 4: The DAMA WIMP-nucleon cross section result and the CDMS limits. The 3σ DAMA region is shown in gray. The region above the solid (dashed) black curves are excluded at 90% confidence by the current (initial) analysis of the CDMS-II Soudan WIMP search.

experiment. The CDMS collaboration produced a null result and placed a limit on the WIMP-nucleus cross section [40]. The DAMA result is in the exclusion region of the CDMS as shown in Fig. 4. Although the CDMS result is model depended but the DAMA is not, the conflict cannot be resolved other than for particular models and assumptions [41]. The CDMS and DAMA results clearly do not agree with each other.

Both DAMA and CDMS are running now with larger mass detectors to continue this investigation. A number of other experiments based on different targets are now

running or in progress as well.

c. EDELWEISS

The EDELEWISS (Exp´erience pour Detecter Les WIMPs en Site Souterrain) experiment is located in the Laboratoire Souterrain de Moudane at a depth of 4800 mwe beneath the French-Italian Alps. The detector employs same WIMP target and technology as CDMS does but with a smaller size of 20 mm thick and 70 mm in diameter. No WIMP was observed for an 11.7 kg-days exposure over data taken in 2000 and 2002. The limit based on the standard halo and WIMP assumptions is incompatible with the DAMA results at more than a 99.8% CL [42-43].

d. ZEPLIN I

The ZEPLIN (ZonEd Proportional scintillation in Liquid Noble gases) I detector consists of a fiducial mass of 3.1 kg liquid xenon target viewed by 3 photomultiplier tubes. The detector is operated by UKDMC (UK Dark Matter Collaboration) at Boulby Mine in UK. Their results based on 90 days run in 2001-2002 found no WIMP events and the limits excluded DAMA results [44].

e. Other Experiments

There are a few other competitive experiments based on various techniques. Some of these experiments have the potential to lead the direct WIMP detection in the future.

The CRESST (Cryogenic Rare Event Search using Super conducting Thermometers) experiment, located in the Gran Sasso underground laboratory, uses cryogenic detectors based on scintillating $CaWO_4$ crystals. The detector module consists

of $CaWO_4$ target as a calorimeter measuring the recoil energy (phonons) and a nearby cryogenic detector optimized for detecting the scintillation light, which differ substantially for nucleus, electron or gamma elastic scatterings of the same energy. The combination of phonon and light signal can be used to discriminate nuclear recoils from backgrounds. Data of an exposure of 20.5 kg days with two 300 g CRESS-II prototype had been analyzed [45]. Their exclusion limit is comparable to DAMA and CDMS I.

The DRIFT (Directional Recoil Identification From Tracks) detector is a gaseous time projection chamber (TPC) operated by UKDMC group at Boulby Mine. Charges produced by interaction within the gas will create a track. The gas currently used is low pressure CS_2, which can easily capture electrons produced in the gas forming a CS_2^- ion. Thus the massive ions are drifted in the TPC instead of electrons, which improves the spatial resolution. The TPC can easily discriminate nuclear recoils from electron recoils because of the track length (electrons travels much longer in the gas than nuclei of the same energy). The advantage of DRIFT detector is it can determine the direction of the track and hence the incident WIMP direction, which is ideally suited for the search of annual modulation. The DRIFT- II detector is an array of DRIFT modules. Each DRIFT-II module has a 1 m^3 CS_2 (167g).

The XENON experiment is aimed to build a 1-ton scale liquid Xe detector (XENON 1T), distributed in 10 identical modules (XENON100), each a two-phase Xe TPC with 100 kg fiducial mass [46]. The detector use scintillation and ionization to discriminate nuclear recoils from backgrounds. Currently they have developed a 15 kg module (XENON10) and installed underground at the Gran Sasso National Laboratory

(LNGS). So far they have achieved very good stability and light collection efficiency (2 p.e./keV). Their first result for an exposure of 135 kg days from the XENON10 prototype yields a limit 6 times better than the best previous limit [47].

The ZEPLIN II experiment is the first one to use the two-phase-Xe approach to detect WIMPs, which will be described in the next chapter.

CHAPTER II

THE ZEPLIN II DETECTOR

The ZEPLIN II experiment is one of the direct WIMP search experiments, built at UCLA, TAMU and RAL (Rutherford Appleton Laboratory, U.K.). The detector was operated at the Boulby Mine underground laboratory in the U.K., aiming to observe WIMP-caused elastic nuclear recoils in liquid xenon. The detector uses the two-phase (gas and liquid) xenon approach, which makes it possible to discriminate background electron recoils from nuclear recoils by measuring both the scintillation and ionization signals.

A. Use of Liquid Xenon

Extensive R&D on searching for dark matter with liquid xenon was carried out by the ICARUS collaboration since the early 90's [48-51]. Liquid xenon has many properties that are ideally suited for WIMP search.

1. Properties of Xenon

Xenon, as a noble gas, exists in the earth's atmosphere in trace amounts. The general physical properties and atomic properties of xenon are listed in Table I [52]. Some important properties related to liquid xenon will be presented below. The isotopes of xenon, including synthetic radioisotopes, are also listed in Table I [53]. Most natural xenon isotopes are stable except ^{124}Xe and ^{136}Xe. The ^{136}Xe can decay into ^{136}Ba through double beta decay [54]. The abundance of ^{136}Xe is 8.9% which could make ^{136}Xe an intrinsic radioactive background source. However, this type background can easily be

Table I: Properties of xenon.

a. General properties.

Atomic Number	54
Standard atomic weight	131.293(6) $g.mol^{-1}$
Electron configuration	$[Kr]4d^{10}5s^{2}5p^{6}$
Density	5.894 g/L (0 °C, 1 atm)
Melting point	161.4 K (-111.7 °C)
Boiling point	165.03 K (-108.12°C)
Triple point	161.405 k, 81.6 kPa
Critical point	289.77K, 5.841 MPa
Heat of fusion	2.27 $kJ{\cdot}mol^{-1}$
Heat of vaporiztion	12.64 $kJ{\cdot}mol^{-1}$
Thermal conductivity	(300 K) 5.65 m $W{\cdot}m^{-1}{\cdot}K^{-1}$
Speed of sound	(liquid) 1090 m/s
Dielectric constant	(liquid) 1.96
Compressibility	1.68 $cm^{2}dyne^{-1}$

b. Atomic properties.

Crystal structure	Cubic face centered
Oxidation states	0, +1, +2, +4, +6, +8 (weakly acdic oxide)
Electronegativity	2.6 (Pauling scale)
Ionization energies	1st: 1170.4 kJ/mol 2nd: 2046.4 kJ/mol 3rd: 3099.4 kJ/mol
Atomic radius	108 pm
Covalent radius	130 pm
Van der Waals radius	216 pm

Table I. Continued

c. Isotopes with their abundances and decay properties.

Isotope	Abundance	Half-life	Decay	Decay E (MeV)	Decay Product
^{124}Xe	0.1%	1.1×10^{17}y	Double e^- capture	(No data)	^{124}Te
^{125}Xe	(Synthetic)	16.9 h	e^- capture	1.652	^{125}I
^{126}Xe	0.09%	(stable)			
^{127}Xe	(Synthetic)	36.4 d	e^- capture	0.662	^{127}I
^{128}Xe	1.91%	(stable)			
^{129}Xe	26.4%	(stable)			
^{130}Xe	4.1%	(stable)			
^{131}Xe	21.29%	(stable)			
^{132}Xe	26.9%	(stable)			
^{133}Xe	(Synthetic)	5.243 d	e^- decay	0.427	^{133}Cs
^{134}Xe	10.4%	(stable)			
^{135}Xe	(Synthetic)	9.10 h	e^- decay	1.16	^{135}Cs
^{136}Xe	8.9%	2.36×10^{21} y	Double e^- decay	(No data)	^{136}Ba

discriminated from nuclear recoil events using the two-phase approach which will be described later.

a. Liquid Xenon Density

For liquid xenon, the density varies with temperatures as shown in Fig. 5. At triple point temperature (161.4 K), the density is 2.98 g/cm^3.

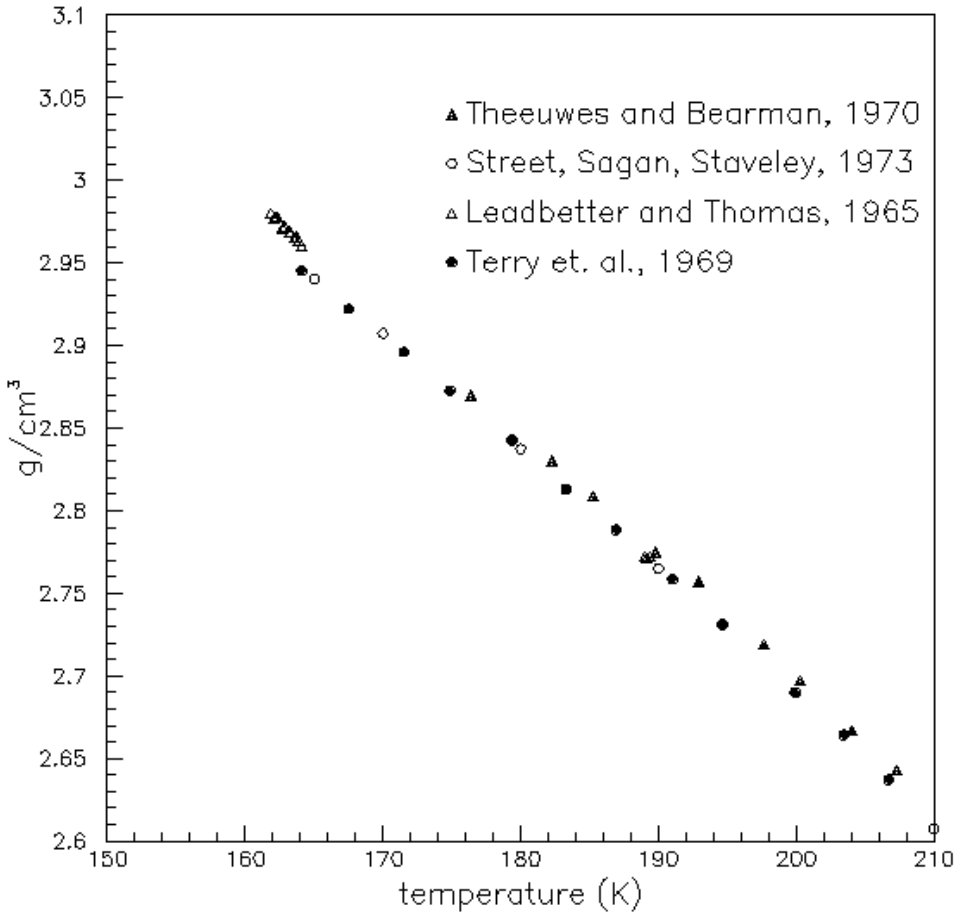

Figure 5: Liquid xenon density as a function of temperature [55-58].

b. Refractive Index

The refractive index of liquid xenon is a function of wavelength. For intrinsic scintillation light with wavelength 180 nm at the triple point (T = 161.4K) the value is 1.5655±0.0024±0.0078 [59]. At temperature 170 K, the value is 1.69±0.02 for light of wavelength 178 nm [60].

Scintillation properties of xenon and other properties related to particle detection will be presented in following sections.

2. Advantages of Liquid Xenon for WIMP Search

a. Availability

Xenon is available in large quantities with both even and odd spin isotopes, including ^{129}Xe (spin 1/2, abundance 26.4%), ^{131}Xe (spin 3/2, 21.2%), and ^{132}Xe (spin 0, 26.9%).

b. High Density and Atomic Number

As shown in Chapter I, the WIMP-Nucleon elastic scattering cross-section is proportional to A^2. Xenon has the largest atomic number (A = 131.29) among commonly used WIMP detection targets such as Na (A = 22.99), Si (A = 28.1), Ge (A = 72.64), and I (A = 126.94). This would be a particularly advantageous if the energy threshold can be driven below 20 keV, although the event rate is suppressed significantly by form factor above 60 keV. From Fig. 5, the density of liquid xenon at 161K is ~3 g/cm^3. The high density ensures small surface exposure that corresponds to low outside backgrounds. Figure 6 shows the X-ray and gamma ray attenuation length in xenon. High gammas interact with xenon in a few centimeters because of the high density of 3 g/cm^3, thus xenon has self-shielding effect against gamma background from ambient materials.

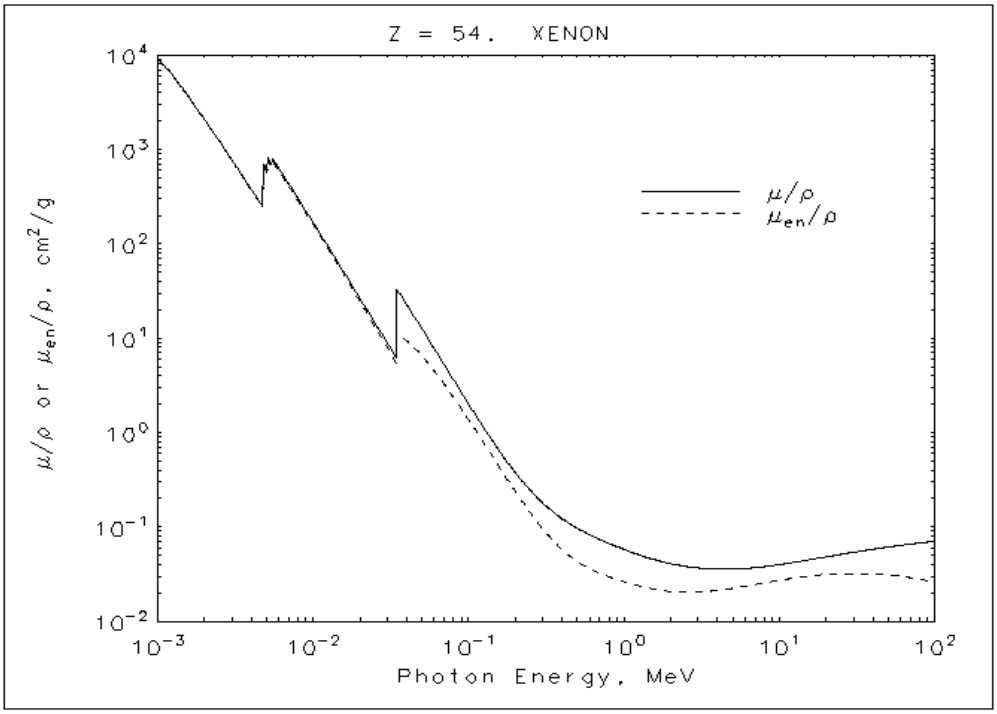

Figure 6: X-ray and gamma ray attenuation length in liquid xenon [61].

c. Purification

Liquid xenon can be highly purified by using an Oxisorb filter and a simple distillation procedure to the order of 0.1 ppb [48]. It's reported that the attenuation length of Xe scintillation light is of order 1 m, and the life time of free electrons is ~5 ms. [49], which is ideal for measuring ionization energy in the liquid Xe. Radioactive contaminations such as ^{85}Kr can be reduced to a very low level by centrifugation. The Xe is virtually background free [50].

d. Small Fano Factor

The Fano Factor is a measure of the dispersion of energy distribution. Theoretical estimation of Fano factor for liquid xenon is 0.041 [62]. Experimental result from J. Seguinot et al. is $F = 0.033 \pm 0.045$ [63].

e. High Scintillation and Ionization Yield

Scintillation efficiency of liquid xenon is close to that of NaI(Tl) and less quenching effect compare to other solid and liquid scintillators. Low energy threshold is possible and good event-by-event background rejection is achievable by measuring both scintillation and ionization [50].

f. Technique

The LXe detector can be operated at temperature 77 K as opposed to 20 mK, at which CDMS is operating. Furthermore, the detector based on LXe can be scaled up to a larger volume without much more difficulty by simply increase the tank size of liquid xenon. In contrast, Ge-based detector, for example, suffers from the difficult fabrication process and large volume impurities, and hence limited scalability.

B. Two-phase Xenon Approach

1. Xenon Scintillation Mechanism

Nuclear or electron recoil in liquid xenon produces both excited Xe^* state and ion Xe^+. The Xe^* immediately forms excited meta-stable excimer Xe_2^* in singlet and triplet states with a Xe atom. The Xe_2^* decays to the ground state with time constants 3 ns (singlet) and 27 ns (triplet), emitting the characteristic 175 nm scintillation photons. The ionized Xe^+ immediately combines with a Xe atom forming Xe_2^+. The Xe_2^+ then recombines with a free thermal electron, again forming Xe_2^* which decays as the same emission process described above. Figure 7 illustrates the xenon scintillation mechanism. The overall time constant of light emission is governed by the recombination process.

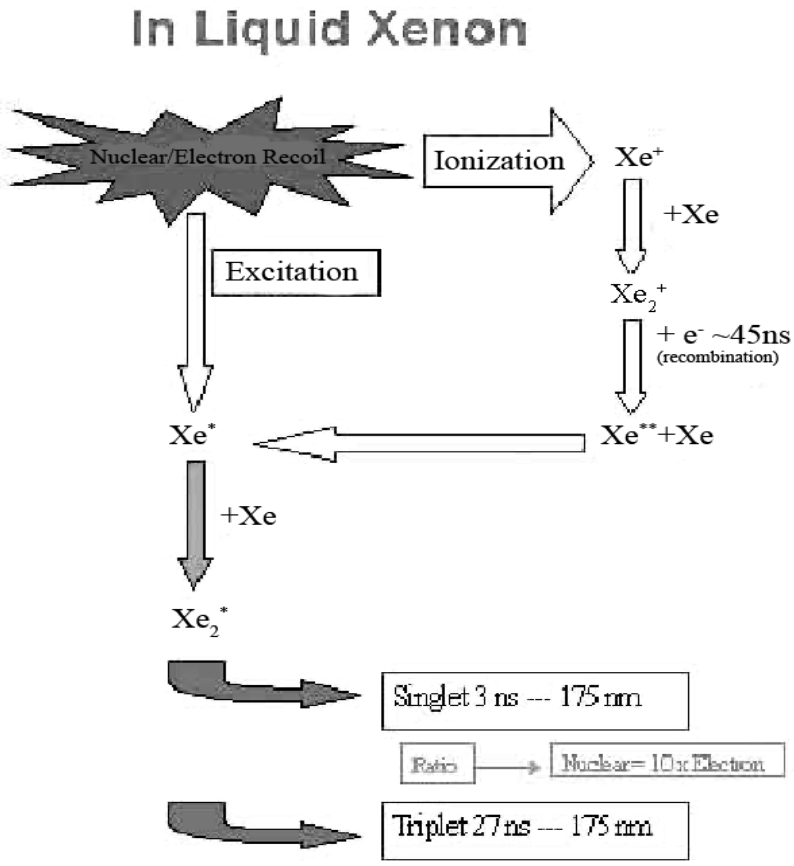

Figure 7: Liquid xenon scintillation processes.

For electron recoils, about 1/4 of the light is emitted from direct scintillation and 3/4 from the ionization process. And 8% of total light comes from the fast singlet component. The time constant for the scintillation light produced by electrons is ~30-40 ns. For alpha collisions the time constant is dominated by the two exponential decays of the two states, and the ratio of singlet to triplet is about 80%. The time constant for alpha produced light is 15-20 ns. The difference in time constants between scintillation light produced by electrons and alphas is caused by the different ionization density left by the two types of particles. Nuclear recoils behavior the same way as alpha collisions. So the

time constant of scintillation light signal can be used to discriminate electron recoils from nuclear recoils. If an external electric field is applied, the ions can be extracted so that both scintillation and ionization can be measured, and hence more powerful discrimination can be achieved.

2. Two-phase Xenon Detector

A detailed description of using two-phase xenon as a detector target has been given in [50]. As shown in Fig 8, two parallel grids in the liquid xenon, one at the base of the target vessel and the other close to the liquid surface, provide an electric field (~1 kV/cm) to cause the ionization electrons to drift toward the liquid surface. A third grid above the surface provides both electron extraction field (~5 kV/cm) in the liquid and electroluminescence field (~10 kV/cm) in the gas. When a xenon nucleus undergoes a collision, the recoiling nucleus excites and ionizes xenon atoms nearby and produces both scintillation light and electro-ion pairs as described in Fig. 7. A fraction of the electron-ion pairs will recombine and form an excited Xe_2^* which gives scintillation light as well. The scintillation light is detected by photo multiplier tubes (PMTs) above the grids and this gives a pulse (the primary pulse S1). The primary signal is proportional to the recoil energy under a certain electric field. The ionized electrons that are not recombined with ions will form an electron cluster and drift upward under the electrical field for a few microseconds to reach the liquid surface. They are emitted from the surface because of the high extraction field. The electron cluster creates electroluminescence light while it passes through the gaseous xenon between the top grid and liquid xenon surface. The luminescence light is detected by the PMTs and gives

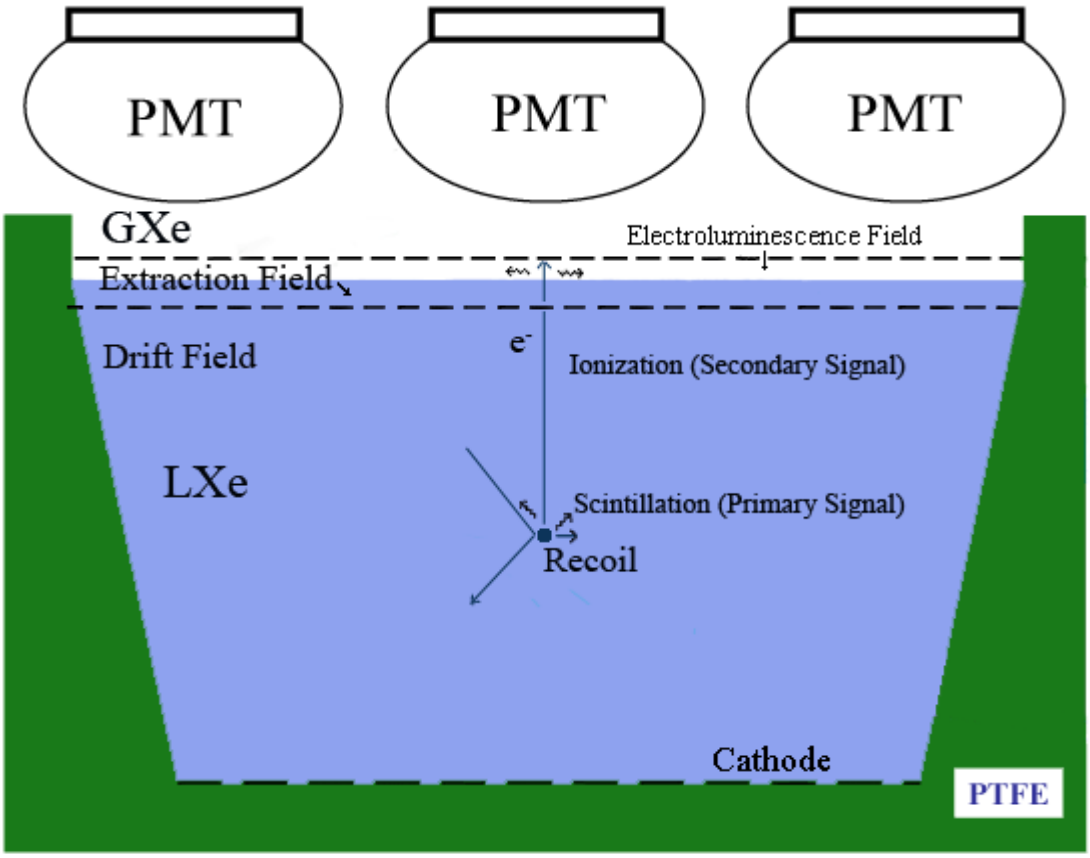

Figure 8: A schematic illustration of the two-phase xenon detector. Recoils in the liquid xenon give both scintillation and ionization. The scintillation light is detected by the photo-tubes. The ionization can be measured by the fluorescence caused by electrons extracted into the gas.

the secondary pulse (S2). The pressure and the electric field in the gas are maintained such that the gas works in proportional mode and the secondary pulse is proportional to the charge and therefore proportional to the recoil energy. Because the ionization density is much larger for a recoiling nucleus than a recoiling electron (as from a gamma interaction), the electron-ion recombination effect is stronger for nuclear recoils than electron recoils. The ratio of ionization to scintillation is much larger for electron recoils.

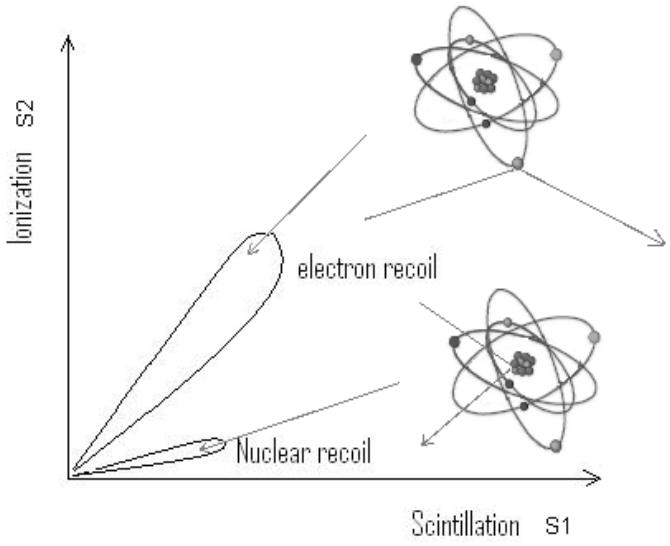

Figure 9: Discrimination of nuclear recoils from electron recoils by measuring both scintillation and ionization.

This can be used to discriminate electron recoil background by measuring both scintillation and ionization in the liquid xenon (Fig. 9). Pulse shape of the signal produced by scintillation can also be used to discriminate nuclear recoil signals from other backgrounds since xenon gives a faster mean pulse decay time for nuclear recoil events than for electron recoil events. The delay between the two pulses (S1 and S2) is the drift time of the charge and thus is a measure of the depth of the recoil event. The relative light intensity of the PMTs can be used to measure the horizontal position of the event.

C. Scintillation (S1) Measurement

1. **Scintillation Photon Yield**

a. W_{ph} Factor

The average energy needed to produce a scintillation photon in liquid xenon is listed in Table II [64].

Table II: Average energy needed to produce a scintillation photon, W_{ph} (eV) in liquid Xe from various measurements and estimations.

Relativistic electrons	α-particles	Relativistic heavy Particles (W'_{ph} (eV))
23.7 ± 2.4	19.6 ± 2.0	14.7 ± 1.5
<35	16.3 ± 0.3	
67 ± 22	39.2	
29.6 ± 1.8		
14.2, 12.5, 12.3		
42 ± 0.6		

In the table, W'_{ph} is the "intrinsic W_{ph} value assuming neither quenching nor escape of electrons occur:

$$W'_{ph} = W/(1+N_{ex}/N_i) \quad (2.1)$$

where W is the average energy needed to produce an electron-ion pair which is described in the following subsection, W = 15.6 eV, N_{ex} and N_i are the number of excited Xe atoms and the number of ion pairs, respectively. The total scintillation photon yield is in the range from 20 k to 80 k photons per MeV. The wild range in W_{ph} is caused by different experimental conditions such as purity and temperature.

b. Quenching Factor for Nuclear Recoil

The quenching factor (or relative scintillation efficiency) for nuclear recoil is the ratio of amount of light produced by a recoil nucleus to the amount of light produced by an electron of the same recoil energy at zero electric field. Theoretical estimation (for example Lindhard theory [65]) predicts the quenching factor is logarithmically related to

the recoil energy with $k = 0.15$. The quenching factor in liquid xenon has been measured by several groups [66-70]. The average value QF = 0.19±0.02 remains constant in the recoil energy range of 10's keV.

2. Effect of External Electric Field

In the scintillation mechanism the ionized electrons and ions may not be able to recombine with each other under external electric field and hence the light is reduced. T. Doke measured the scintillation yields in liquid xenon as a function of electric field using internal conversion electrons from ^{207}Bi. He found that the scintillation light intensities decreases with increase of the external electric field, but even under very strong electric fields the ratio of light yield over that without the electric field is larger the value predicted by Onsager's theory, which governs the recombination process between electrons and ions. This phenomenon is explained by the behavior of recombination free electrons, which are outside the critical distance from their parent ions where the Coulomb energy is equal to thermal energy. The recombination process between recombination free electrons and ions takes a considerably long time (>msec) so that the scintillation produced from such a recombination cannot be observed by the fast pulse detecting techniques. The scintillation and ionization yield in liquid xenon as a function of applied electric field for electron, nuclear, and alpha recoils has been performed by E. Aprile et al [69,71-72]. The ratio of scintillation yield under electric field to that without electron field of electron recoils is larger than the ratio from nuclear recoils or alphas. This is because the scintillation yield per unit absorbed energy due to

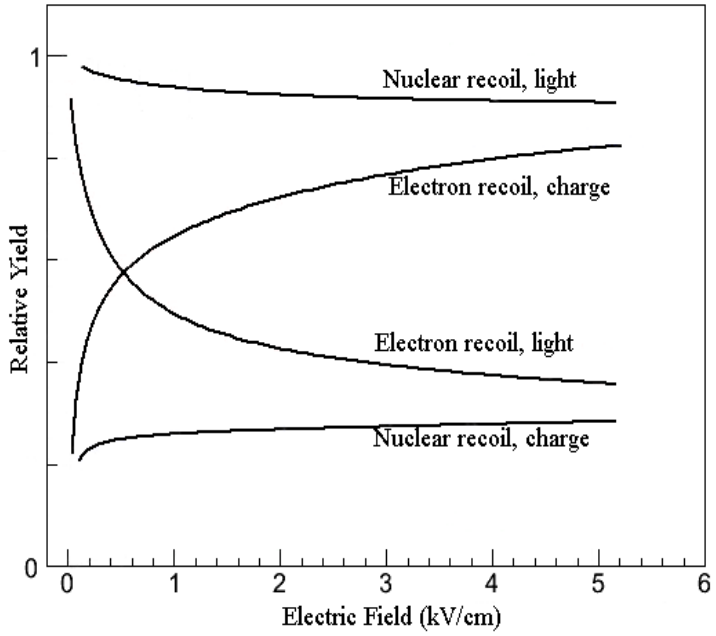

Figure 10: Field dependence of scintillation and ionization yield in liquid xenon for electron recoils and nuclear recoils [69, 71-72].

recombination free electrons is smaller than that due to nuclei and alpha particles, which produce much higher ionization along the track. The relative scintillation and ionization yield for nuclear recoils and electron recoils as a function of electric field is sketched in Fig. 10.

3. Scintillation Light Attenuation Length

Light attenuation can be described by the equation: $I(x) = I_0 e^{-x/\lambda_{att}}$, where λ_{att} is the attenuation length. Two main processes that account for the loss of light are Rayleigh scattering (scattering length λ_{sca}) and absorption by impurities (absorption length λ_{abs}). The attenuation length is related to its two components by: $1/\lambda_{att} = 1/\lambda_{sca} + 1/\lambda_{abs}$. The measurement of scintillation light attenuation length in liquid xenon has been performed by A. Baldini et al. and an absorption length longer than 100 cm has been observed [73].

D. Ionization (S2) Measurement

1. The *W* Factor

The *W* factor in liquid xenon can be accurately evaluated if the band structures and its oscillator strength are known. The band structure of liquid xenon is studied by U. Rossier, G. Keitel, and P. Schreber [74-75]. A schematic illustration is shown in Fig. 11.

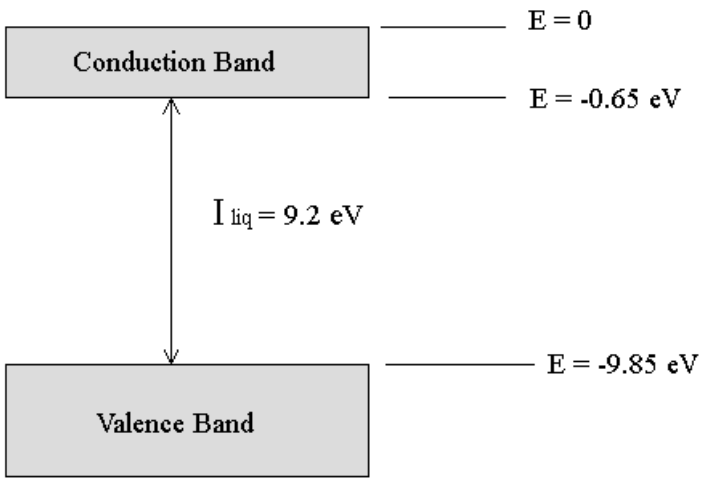

Figure 11: Band structure of liquid xenon.

The *W* factor in liquid xenon can be calculated using the Platzman's energy-balance equation [76]:

$$\frac{W_l}{E_g} = \frac{E_i}{E_g} + \frac{E_{ex}}{E_g}\frac{N_{ex}}{N_i} + \frac{\varepsilon}{E_g} \tag{2.2}$$

where W_l is the *W* value in liquid xenon, E_g is the band gap energy, N_i is the number of electron-ion pairs produced at an average energy expenditure of E_i, N_{ex} is the number of excitons at an average energy expenditure of E_{ex}, and ε is the average kinetic energy of sub-ionization electrons. Assuming the sub-ionization electron have energy less than E_i,

and distribute proportionally to the state density dN/dE for the energy levels (Shockley's model), the quantity ε is given as:

$$\varepsilon = \int_0^{E_1} E \frac{dN}{dE} dE \Big/ \int_0^{E_1} \frac{dN}{dE} dE \tag{2.3}$$

The quantities appearing in equation (3.2) for liquid xenon are given in Table III [12].

Table III: Quantities appearing in the Platzman's energy balance equation for xenon in the liquid state.

Liquid	E_i (eV)	E_{ex} (eV)	N_{ex}/N_i	ε (eV)
Xe	10.5	8.4	0.06	4.65

The calculated W_l/E_g (=1.69) is in good agreement with the experimental value (=1.68) [77], which corresponds to W_l = 15.6 eV.

2. Fano Factor

The Fano factor is a measure of the statistical fluctuation of a probability distribution. Consider a recoil energy *E* absorbed by the liquid xenon. The number of electron-ion pairs produced is *N*. The average energy used to produce a pair is denoted by *W* = *E/N*. The variance in the number of photons created is

$$\sigma_N^2 = \overline{\left(N - \frac{E}{W} \right)^2} = \overline{N} F \tag{2.4}$$

where *F* is the Fano factor. The energy resolution is given by

$$\frac{\sigma_E}{E} = \frac{\sigma_N}{N} = \sqrt{\frac{F}{N}} \tag{2.5}$$

The calculation of *F* can be written as [12]:

$$F = F_1+F_2+F_3$$

$$= \left(N_{ex}/N_i\right)\left[1+\left(N_{ex}/N_i\right)\right]\left(W_{ex}^2/W^2\right)+\left[\overline{\left(\varepsilon_i - W_i\right)^2}/W^2\right] + \left(N_{ex}/N_i\right)\left[\overline{\left(\varepsilon_i - W_i\right)^2}/W^2\right] \quad (2.6)$$

where $W_{ex} = E_{ex}$, $W_i = E_i + \varepsilon$, and ε_i or ε_{ex} are the energy absorbed per ionization collision or per excitation collision in the energy depositing process of an ionizing particle in matter. The first term F_1 is due to redistributions of the numbers of excited and ionized atoms, while F_2 and F_3 are due to the energy loss fluctutations in ionization an excitation, respectively. For liquid xenon E_i =10.5 eV, E_{ex} = 8.4 eV, N_{ex}/N_i = 0.06, and ε = 4.65 eV [12]. F_1, F_2, F_3 are calculated to be 0.019, 0.021, 0.0006, respectively, and F = 0.041.

3. Electron Drift Velocity and Diffusion Coefficient

Long electron drift distance under electric field in liquid xenon is essential to the detection of the ionization signal. P. Benetti *et al*. have measured the electron lifetime and several milliseconds drift time has been achieved [49]. The drift velocity of electrons in liquid xenon depends on both the applied electric field and temperature. The drift velocity decreases almost linearly with the temperature with a slope of 1.2×10^3 $cm\cdot s^{-1}\cdot{}^oC^{-1}$. This indicates that the temperature stability is a very important factor to achieve good time resolution in liquid xenon. The field dependence of the drift velocity in solid and liquid xenon near the triple point has three main features: linear at low field below 100 V/cm; drift velocity varies as $E^{1/2}$ as the electric field (E) increases up to 5 kV/cm; drift velocity is completely saturated in the high field region: $v_{sat} = 2.86\times10^5$

cm/sec [78]. As a result, the electron drift length in liquid xenon could be 3-5 meters (for 2-3 ms lifetime estimates) assuming the electric field is 1 kV/cm.

While the electron cluster produced by the ionization radiation drifting under the electric field in liquid xenon, the cluster gradually spreads by diffusion. The longitudinal diffusion will affect the pulse width of the secondary signal and the diffusion in the transversal direction will blur the horizontal position of the electron cluster. The spread of the electron group is proportional to $(Dt)^{1/2} = (Dd/\mu E)^{1/2}$, where D is the diffusion coeffiecient, t is the time, d is the drift distance, μ is the mobility and E is the electric field strength. If the electron drift velocity or the electron mobility in the liquid xenon is known, we can get the diffusion coefficient by using Einstein's relation:

$$eD/u = kT = 2 < \varepsilon > /3 \tag{2.6}$$

where $<\varepsilon>$ is the agitation energy. The measurement of $<\varepsilon>$ for gas xenon and liquid xenon has been performed by E. Shibamura et al.[79]. Figure 12 shows the field dependence of the diffusion coefficients of electrons in liquid xenon obtained from the data of [79].

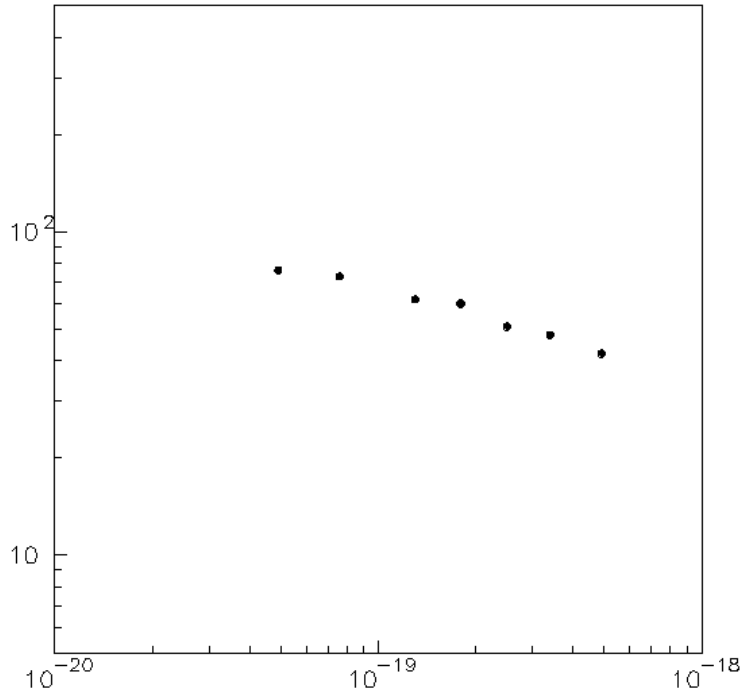

Figure 12: Diffusion coefficient of electrons in liquid xenon as the function of density-normalized electric field. Figure derived from [79].

4. Electron Extraction from Liquid Xenon

The emission of electrons from non-polar dielectrics can be treated as a threshold process with correlation between the energy of the electrons V_0 and the electric field E_0 [80]. Electron emission from liquid xenon has been observed at $E > E_0$, The total number of electron emission is determined by the lifetime of electrons before their capture. The field dependence of electron emission in liquid xenon is measured in [81]. For the extraction field higher than 10 kV/cm, all excess electrons can be extracted from the liquid xenon to the gas xenon.

5. Electroluminescence Light Yield

Electrons extracted from liquid xenon get accelerated under electric field in the gas phase. If the electron energy gained from the electric potential energy during a mean free path is larger than the xenon excitation energy, the drifting electron will excite xenon molecules and produce proportional electroluminescence light (characteristic 175nm UV light). The number of UV photons produced in the process depends on the drift distance *d*, the electric field *E* and the gas pressure *p*, which is well approximated by:

$$N_{ph} = 70 \times \left[\frac{E}{p} - 1.0 \right] \times pd \tag{2.7}$$

where N_{ph} is the number of photons produced by one electron, the units for *E*, *p*, and *d* are kV/cm, atm, and cm, respectively.

E. Detector Construction

The ZEPLIN II detector layout is shown in Fig. 13. The target contains 32 kg (27kg fiducial) liquid Xe. The seven quartz window 5-inch diameter ETL low-activity D742QKFLB PMTs [82] are supported inside the copper target vessel in a hexagonal pattern (Fig. 14). A tapered PTFE basin gives an excellent light collection efficiency of ~1.4 photoelectrons per keV for the primary scintillation, and prevents charge trapping which allows all charge to be drifted to the liquid surface. Ten pure copper field rings are used to shape the electron drift field in the liquid (Fig. 15). The target vessel, including PMTs, PTFE basin, field rings, liquid xenon, and fine HV meshes, is contained in an oxygen free copper cast. The vacuum vessel is a stainless steel cast. Electrical and

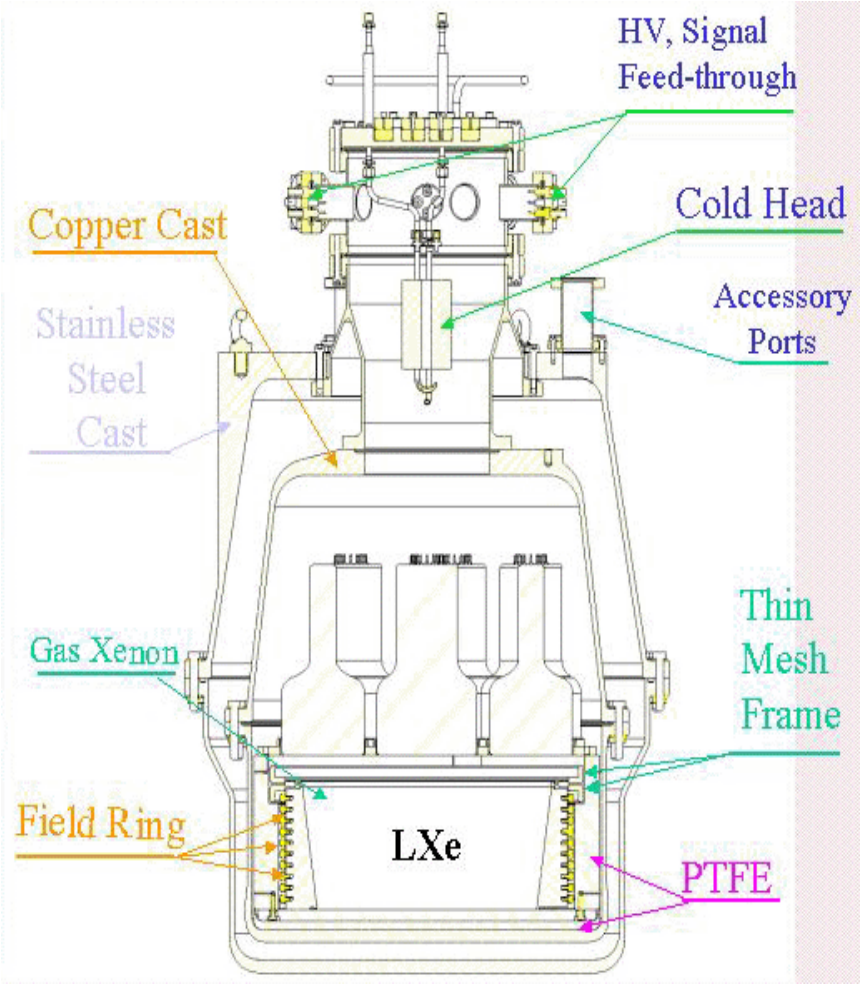

Figure 13: A schematic diagram of the ZEPLIN II detector with target copper vessel and stainless steel vacuum vessel. Xenon liquefaction occurs on the cold head and liquid xenon drips down a copper shield to fill the target volume.

cryogenic connections emerge through the top of the vessels and pass through the shielding. The whole detector is surrounded by liquid scintillator and a lead shield (Fig. 16). The detector is located in the Boulby Underground Lab (3.3 km water equivalent underground) at U.K. (Fig. 17-18).

Figure 14: ZEPLIN II 7 UV sensitive low temperature PMTs assembly.

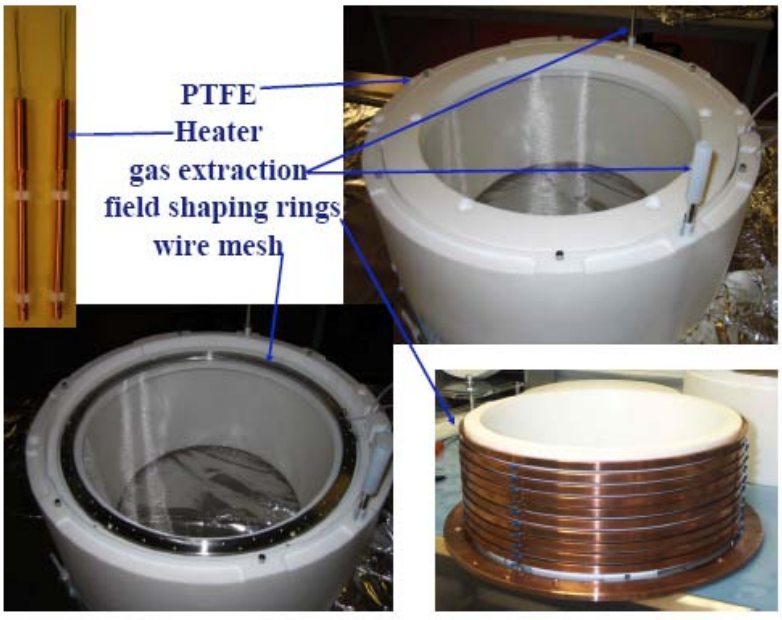

Figure 15: ZEPLIN II detector: PTFE basin, wire grids, and field rings.

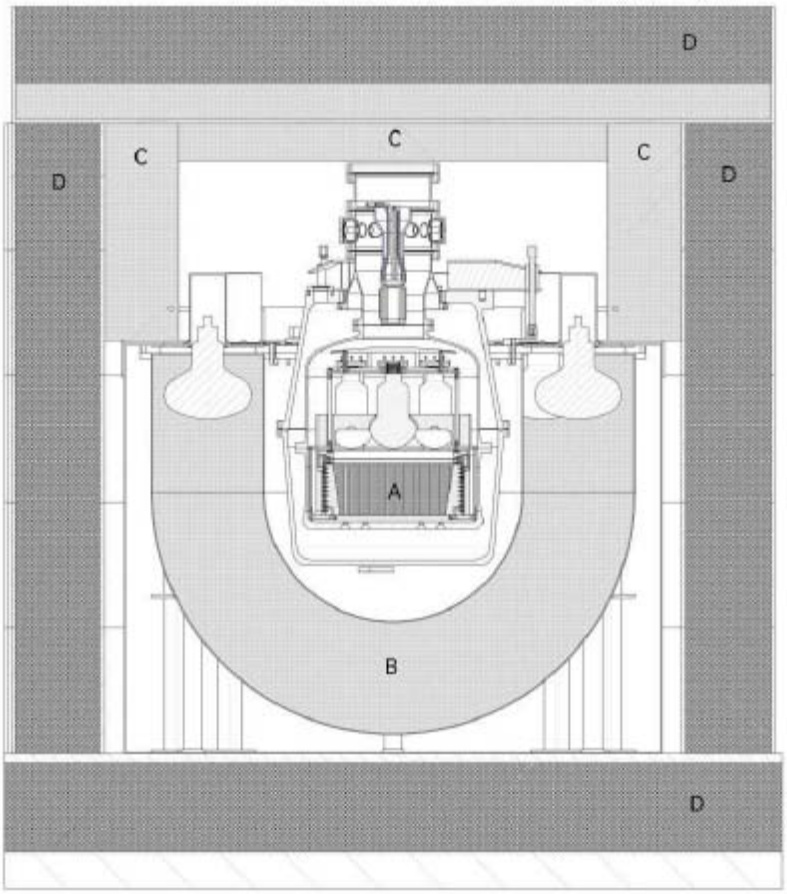

Figure 16: Layout of ZEPLIN II experiment within the gamma and neutron shielding. The detector is located in a 30 cm thick liquid scintillator veto (B) of mass 1 ton. Also shown are 30 cm polypropylene hydrocarbon (C) shielding and the surrounding 25 cm lead gamma ray shielding (D).

Figure 17: A view of the entire ZEPLIN II detector.

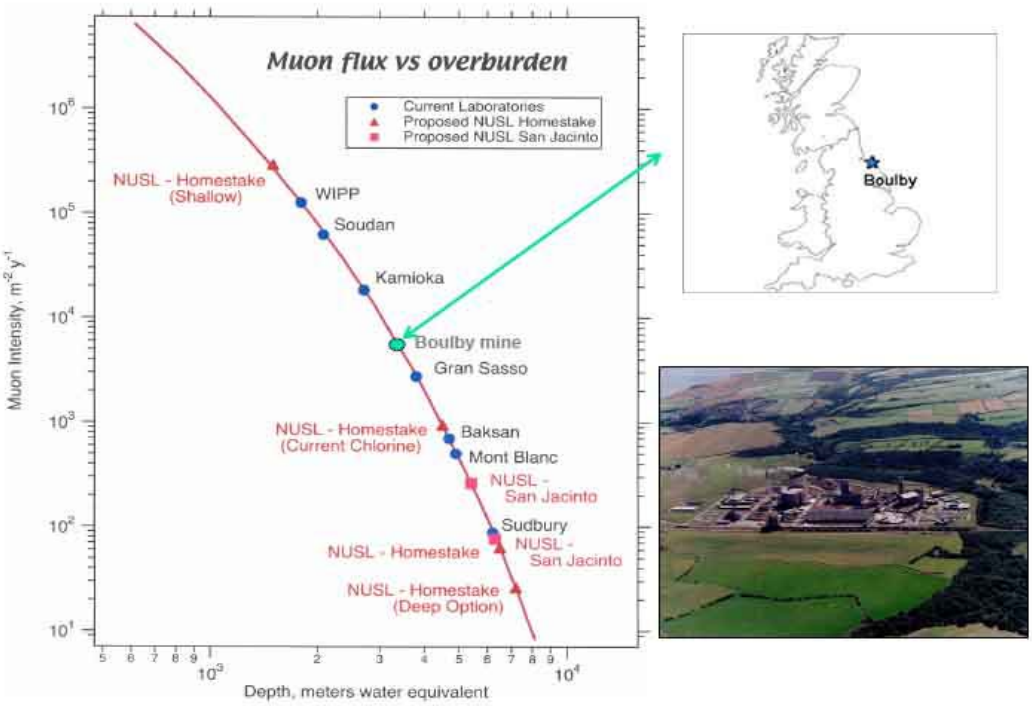

Figure 18: The Boulby mine underground laboratory located at U.K.

CHAPTER III

DATA ACQUISITION AND DATA REDUCTION

A. Data Acquisition System

1. Data Acquisition Hardware

The ZEPLIN II readout equipment includes two categories: monitoring the target parameters through slow-control based on intelligent compact modules interfaced through the serial port; and high speed waveform acquisition based on CompacPCI technology. The run time environmental parameters such as temperature and pressure are monitored by a 64 channel Datascan [83] module. The data acquisition (DAQ) electronics chain is best understood by following the path of the analog signals from the seven PMTs to the digital information stored on magnetic tape. Fig. 19 is a schematic of the DAQ system, traced from the target and veto PMTs to the digitizers via trigger electronics. The signals from the inner target PMTs (-110 ^{o}C) go through the upper head of the target vessel and the are split through a Suhner 4901.01.A 2 GHz 50 Ω divider, with one signal fed to create the trigger and the other to the digitizer. As shown in Fig. 19, the split signals are amplified 10 times larger before entering the discriminator which produces 50 mV/channel for each input signal above a threshold of approximated 2/5 of the single photon electron (SPE) value and sends out the sum to another discriminator. A NIM pulse is sent out when the summed input signals exceed five fold coincidence output. For higher energy events that can heavily saturate the digitizer the electroluminescence signal produces single photo electron emissions that can fire

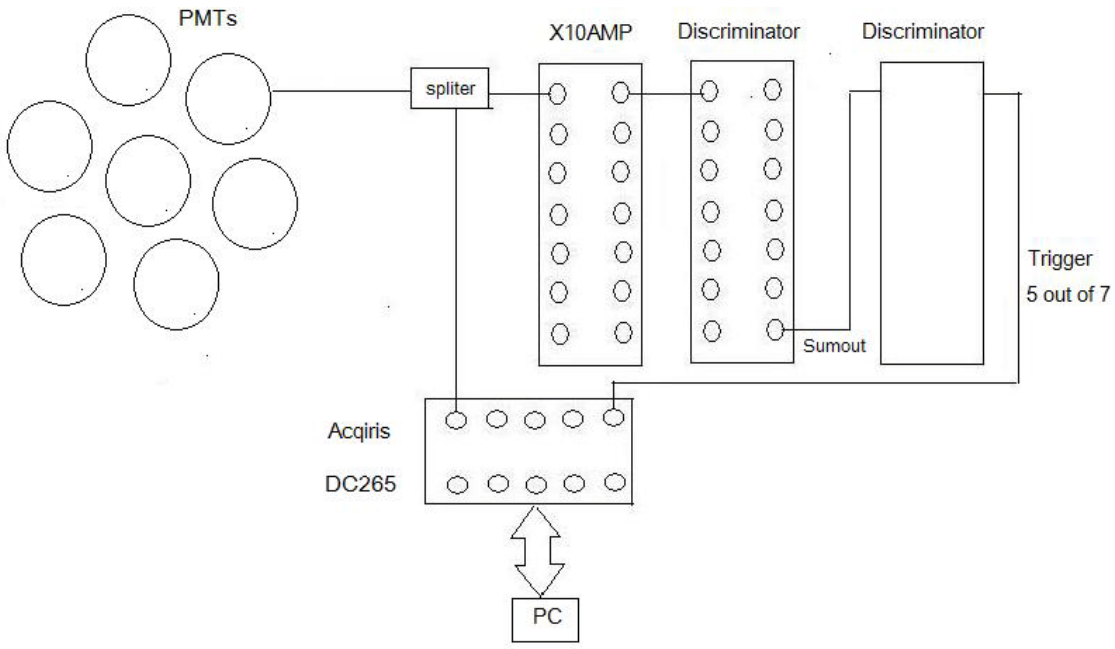

Figure 19: ZEPLIN II data acquisition system.

multiple triggers for tens of μs after the S2 signal. The central PMT (PMT1) sees a larger fraction of scintillation light on average than the other six PMTs. The signal from PMT1 was used to veto high energy feed back signals from triggering the system by sending a 1 ms inhibit signal to the discriminator. The dead time caused by trigger saturation and event rate was measured. For the case of the background rate of 2 Hz, the trigger efficiency was 90% (10% loss due to dead time).

a. The Acqiris Digitizer

Signals from PMTs are digitized using DC265 Acqiris digitizers [84] embedded in a CC103 Acqiris crate. The digitizers (Fig. 20) are CompactPCI/PXI compliant and are fully programmable (LabView and C++) over the PCI bus and deliver oscilloscope-like performance. Data captured by the digitizer can be transferred to a host processor in

the crate over the PCI bus at speeds up to 100 Mbytes/s. The properties of the model are summarized in Table IV.

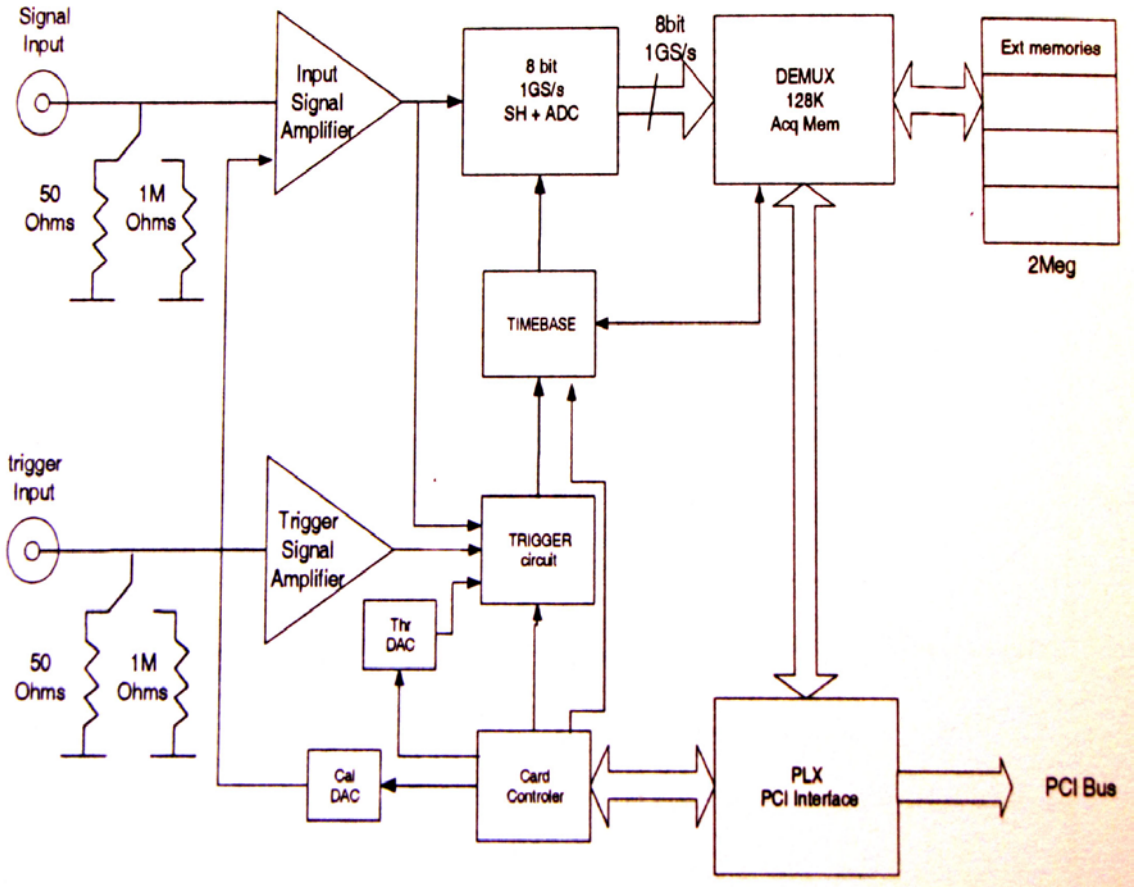

Figure 20: Overview of DC256 Acqiris Digitizer [84].

Table IV: Properties of DC256 Acqiris Digitizer.

Maximum Sampling Rate	500 MS/s
Acquisition Memory	2 Mpoints/channel
Resolution	8-bits (256 levels)
Bandwidth	250 MHz
Trigger Time Interpolator	5 ps
Coupling	AC and DC
Impedance	50 Ω or 1MΩ
DC Accuracy	±1% of the input voltage full scale
Acquisition Modes	Single and Sequential storage modes

As indicated in Table IV, the digitizer provides two acquisition modes: single and sequential. The single mode executes a direct waveform transfer from the memory to the PC buffer, for a single segment at a time using direct-to-memory access (DMA), which is very time-efficient for segments of large samples (10,000 or more). However, when the segments are short, the transfer overhead starts to dominate the overall transfer time because each segment requires a DMA setup. The sequential mode reduces the overhead time by transferring with a single DMA a complete digitizer memory image to the PC memory. Formula for the transfer times of the two modes are:

Single mode: $T_1 = M \cdot Ovhd_{DMA} + M \cdot N \cdot Xfr$

Sequential mode:

$T_2 = Ovhd_{DMA} + M \cdot Ovhd_{buffer} + M \cdot (N + Extra) \cdot Xfr + M \cdot N \cdot Cpy$

with the following definitions:

M	Number of segments
N	Number of sample per segment
Xfr	Transfer time per sample in μs, typically 0.01
$Ovhd_{DMA}$	DMA overhead time (per segment) in μs
$Ovhd_{buffer}$	Circular buffer analysis overhead time (per segment) in μs
$Extra$	Number of 'overhead' data points per segment
Cpy	Time to copy a sample in μs

The DMA overhead time $Ovhd_{DMA}$ is approximately (50000 μs) / (CPU speed in MHz). The Circular buffer analysis overhead time $Ovhd_{buffer}$ is approximately (2500 μs) / (CPU speed in MHz). The *Extra* number depends on the smapling interval (in ns): *extra* = 240 / sampInterval + 96. And the copying time *Cpy* per 8-bit sample is about (5 μs) / (CPU speed in MHz).

To transfer single records of 100,000 samples, recorded at 500 MSamples/s from the DC250 digitizer to computer with 2GHz Pentium CPU, the transferring time is estimated below:

$M = 1$, $N = 100000$, $Xfr = 0.01$, $Cpy = 0.0025$,

$Ovhd_{DMA} = 25$, $Ovhd_{buffer} = 1.25$, $Extra = 120 + 96 = 216$

$$T_1 = M \cdot Ovhd_{DMA} + M \cdot N \cdot Xfr = 25 + 1000 = 1025\ \mu s$$

$$T_2 = Ovhd_{DMA} + M \cdot Ovhd_{buffer} + M \cdot (N + Extra) \cdot Xfr + M \cdot N \cdot Cpy$$

$$= 25 + 1.25 + 100216 \cdot 0.01 + 100000 \cdot 0.0025 = 1278\ \mu s$$

2. Data Acquisition Software [85]

The Linux based DAQ software contains two parts: the controller (*daq_ctl*) and the acquisition process (*daq*). The controller contains a GTK-based graphical user interface (GUI) and basically "logs" into the *daq* to get its status and to control it. The GUI is built with glade and the main interface window is shown in Fig. 21.

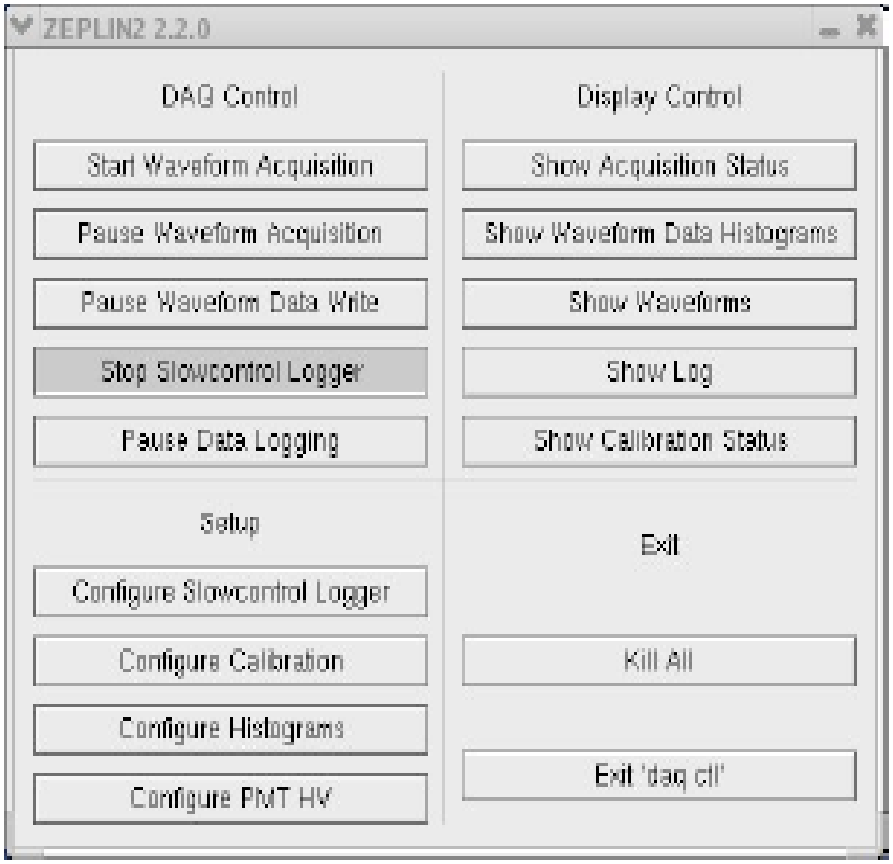

.

Figure 21: Data acquisition software GUI main window.

The *daq* starts four individual threads and handles inter-thread communications:

- *Acquisition* waits for an acquisition instruction and then regulates all the data taking, including waveform hardware communication, getting events, dealing with data files and histogram management.
- *Slowcontrol* reads the temperatures and pressures and writes the logfile.
- *Calibration* manages the manual and automatic calibration and the source position.
- *Remot* is the server to which *daq_ctl* communicates

One can treat *daq* as a server and the *daq_ctl* is a client interface. Through the GUI shown in Fig. 21, one can select “Start Waveform Acquisition” and then setup trigger and channel parameters in the pop-up window as shown in Fig. 22 to start taking data.

The data acquisition using the digitizer is implemented with the setup of trigger and channels. The trigger settings for data acquisition are used to determine the time at which the device will stop acquiring data. The various trigger settings are listed below:

- Trigger source, can be a signal applied to either the input channel or an external trigger input.
- Trigger coupling includes AC LFReject and DC. The AC mode couples signals capacitively and removes the DC component of the input signal and signals below 50 KHz. While DC mode allows all signal components to pass through.
- Trigger level is defined as a set voltage. For external trigger, the trigger level must be set within the range of ± 3 V. For internal triggers, the trigger level is in percentage of digitizer’s full range scale, and must be a value within ±60%.

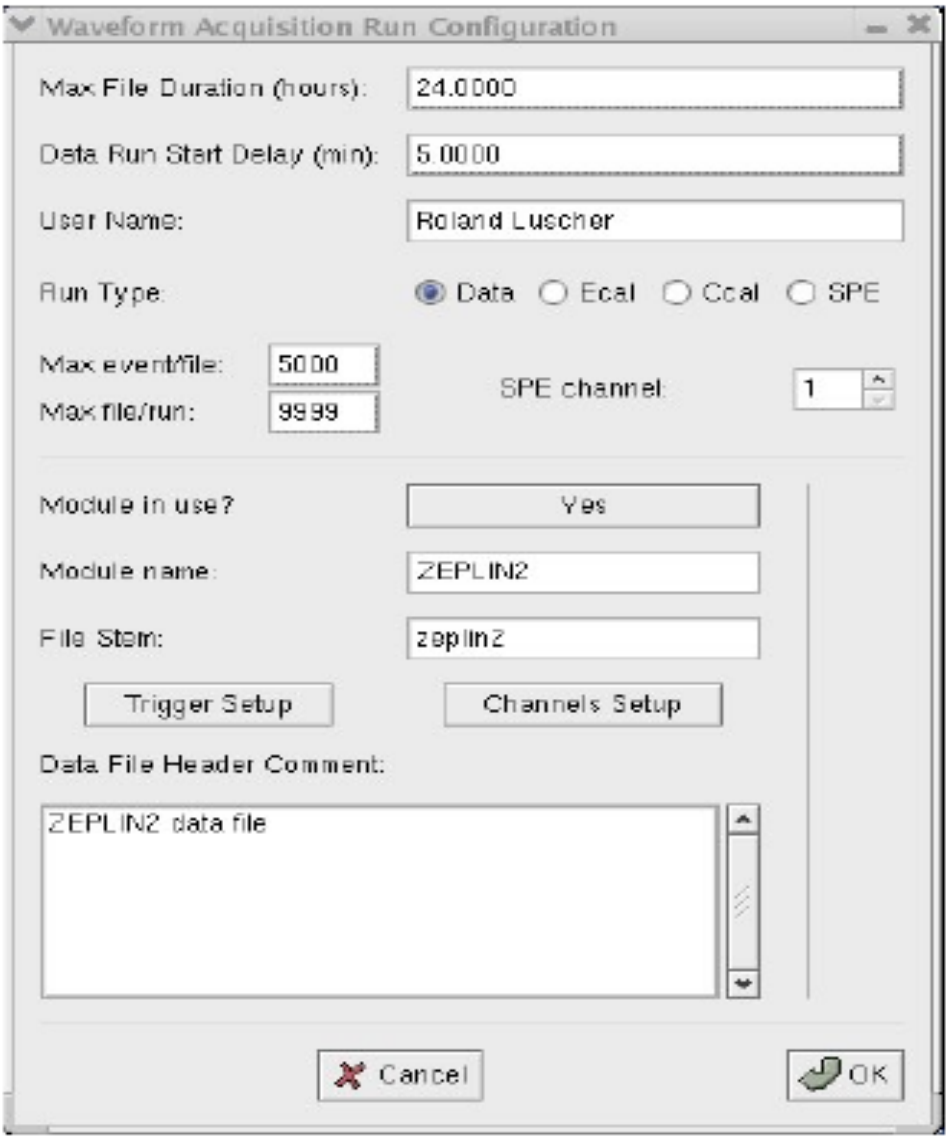

Figure 22: Waveform acquisition configuration.

- Trigger slope has two options: positive and negative. Positive slope indicates the triggering signal is rising when it passes through the trigger level. While negative slope indicates the signal is transitioning from a higher voltage to a lower voltage
- Trigger delay accepts pre- and post-trigger by defining post-trigger setting as a

positive number and pre-trigger setting as a negative number.

- Trigger channel can be any signal channel for internal trigger. There is a separate front panel input for external trigger input. The external input provides a full trigger setup feature as for the internal triggering source.

The channel setups include

- Full range scale (FRS): can be 50 mv, 100 mv, 200 mv, 500 mv, 1 V, 2 V, 5V
- Offset: within ± (FRS/2)
- Coupling: includes both AC and DC coupling modes. AC coupling removes component of the signal below 10 Hz.
- Impedance: 50 Ω or 1MΩ input termination. The 50 Ω coupling mode offers high quality termination with better than ±1% precision. The 1MΩ coupling mode features low capacitance (10 pF) that minimizes loading effects that can occur when probing high frequency circuits.

Other functions provided by *daq_ctl* software are configuration of slow control, calibrations, histograms and PMT HV, as well as display control (Fig. 21).

Configuration of slow-control gives users the chance to allocate TC-module parts to detector modules: Datascan channels are numbered starting from 1 and which tells how many of them attributed to any detector. Configuration of calibration allows users to start manual calibration run or set a time period for automatic calibration runs. The display control reads some status out of a running *daq* such as:

- Acquisition Status. This is the fastest way to get information as only a few numbers are transferred from *daq*. These numbers contain information on

number of events obtained in the present run, current event and trigger rate.

- Waveform data histograms. This makes plots of current content of histograms for energy and time.
- Waveforms display for all channels. The CPU priority is given to the acquisition of data instead of the online display. The program only shows waveforms of a small part of events.
- Log of temperatures up to the last 10 hours
- And calibration status showing the current setting of the calibration mode.

B. Data Reduction

1. Raw Data

The trigger point could be either on the primary scintillation signal or the secondary scintillation. The maximum drift time of the ionized electrons in the liquid xenon is ~80 μs, thus to ensure the full depth of the xenon volume will be covered, whether the trigger is on the primary or secondary, the digitizers are set to acquire data 100 μs before and after the trigger point. An event has seven waveforms from target PMTs and one from shielding veto PMTs, with each waveform having 100 k points, thus an event has 0.8 M points. A raw data file with 2000 events has 1600 M points, each point represented by an 8-bit character. The file is then compressed to approximately 250 MB before saving to storage media (magnetic digital tape capable of storing 100 GB of data). The ZEPLIN II experiment records approximately 25 GB of WIMP search data each day during the active run time. The data are transferred to network clusters based on Linux OS for reduction. The raw data file format is shown in Table V.

Table V: Raw data file format.

File Header	head_id	char[4] = “H004”
	daq_id	char[8] = “CompPCI”
	version_id	short[3] = {2,2,0}
	runtype_str	char[4] = DATA, ECAL, or SPE
	runtype_id	short = 0, 1, 2, 3
	username	char[32]
	start_time	char[32]
	stop_time	char[32]
	detector.trigger	trigger_t
	detector.channels	channel_setup_t
	detector.comments	char[1024]
Event	head_id	char[4] = “H004”
	time_sec	long
	time_usec	long
	temp_target	short
	temp_ambient	short
	waveform.dat[i]	char[detector.trigger.nbr_samples]

In the table, the start_time and stop_time are written as “%d-%m-%y %H:%M:%S”. The trigger_t and channel_setup_t are defined as follows:

```
typedef struct{
    double sampling;
    long nbr_samples, nbr_segments;
        double delay;
    long channel, coupleing, slop;
    double level;
}trigger_t;
Typedef struct {
        double gain[LIMIT_CHAN], offset[LIMIT_CHAN];
```

```
        long coupling[LIMIT_CHAN];
        short saved[LIMIT_CHAN];
        double min_amp_cut[LIMIT_CHAN];
        short in_range[LIMIT_CHAN];
        short satur_cut[LIMIT_CHAN];
        char label [LIMIT_CHAN ][LABEL_LENGTH];
} channel_setup_t;
```

where LIMIT_CHAN is the number of channels in any (multi)instrument. The waveform is written only if the specific channel is saved.

2. Data Reduction

Raw data is analyzed by a Linux-based GUI application built with qt, the UNZAP2, as shown in Fig. 23. The software reads binary raw data and has two main functions: event waveform display with random access and data reduction.

The reduction code processes the waveforms from each channel and the summed channel, which is used to identify pulse signals with smoothing algorithm. For nuclear recoils the S2 signal can be small and appear as a cluster of separate peaks spread out over several μs as shown in Fig. 24. Smoothing and clustering are applied to separate a valid S2 pulse from noise. The smoothed amplitude of each sample is:

$$h_s = \sum_{t=-t_{sm}/2}^{t_{sm}/2} h_t \Big/ N$$

where t_{sm} is the smoothing timescale, N is the number of samples over the interval, and h_t is the amplitude of each sample. Peaks within a cluster are then grouped together to form a single pulse.

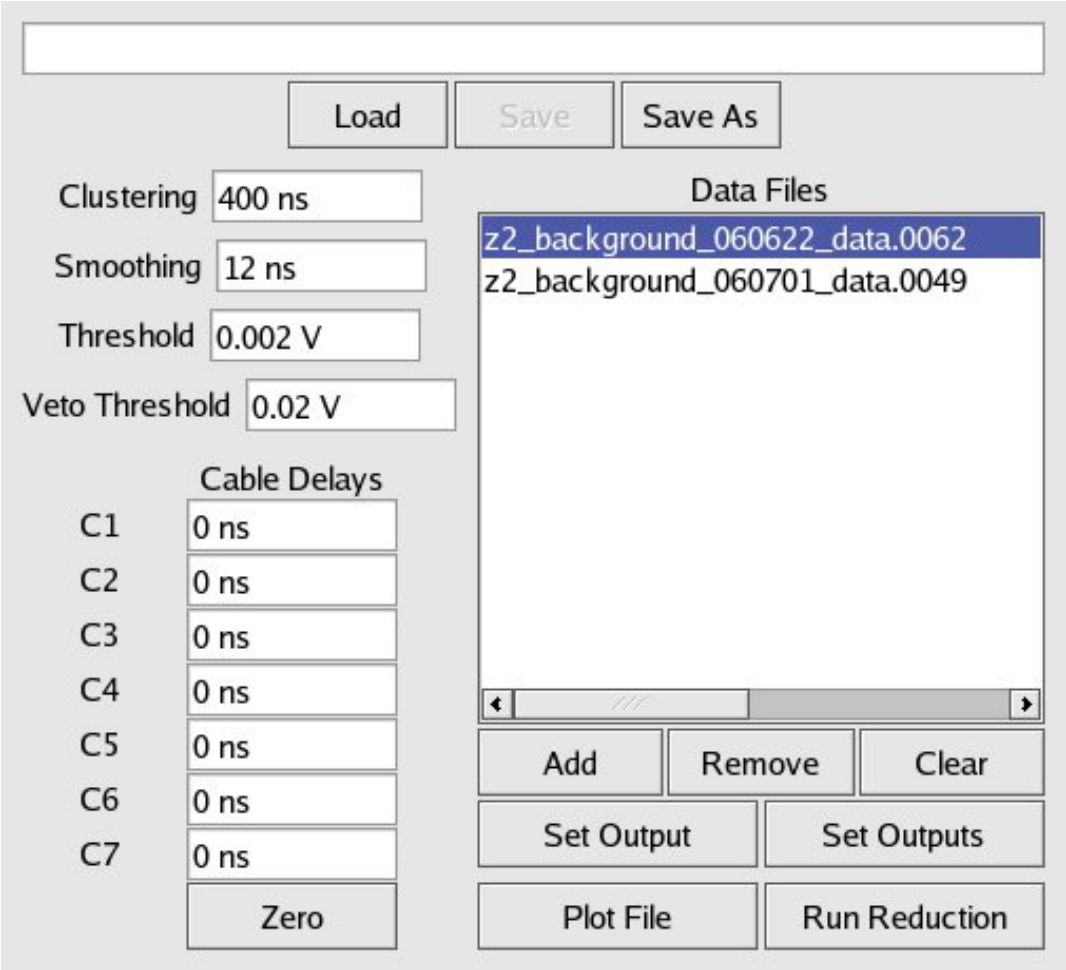

Figure 23: Data reduction software, the UNZAP2.

A number of parameters are needed to perform the data reduction as shown in Fig 23. The clustering and smoothing parameters discussed above were determined by SPE calibration data with value of 400 ns and 12 ns. The smoothed waveform is only used to identify the pulses on the summed channel. Original waveform is used for all other data reduction. The threshold depends on the full rang scale (FRS) of the digitizer. For the data acquired with a FRS of 200 mV the threshold is set to 2 mV, which is about ½ pe and well above the digitizer resolution 0.8 mV.

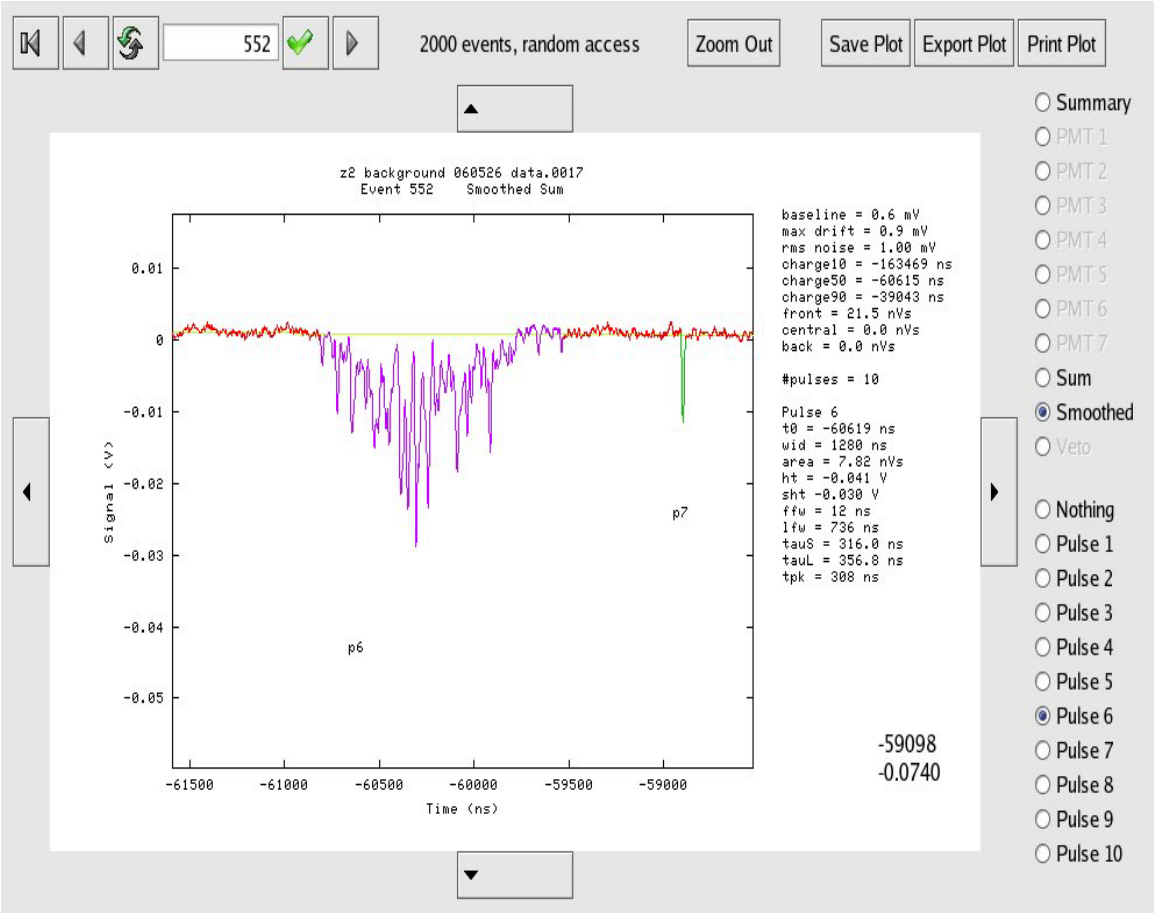

Figure 24: Event waveform display of a secondary ionization pulse. P6 is a cluster of pulses that form the S2 signal while p7 is a separated single pulse.

Cable delay parameters are needed to define the pulses since the summed channel is used and uncorrected delay can be up to 10 ns. This can result in wrong parameterization of S2 identification and timing. The cable delay values are obtained by evaluating the signal delay between each PMT and the central PMT. When c1 = 0 ns, c2 = 3.927 ns, c3 = 7.941 ns, c4 = 8.737 ns, c5 = 10.07 ns, c6 = 6.294 ns, and c7 = 6.916 ns are used, the delay peak between the channels is very close to zero.

Given the input parameters discussed above, the UNZAP2 produces a reduced data file in HBOOK ntuple format including the following parameters:

- Baseline level. The baseline is calculated for each channel of each event using the first 500 samples for the first round reduction. Due to the wandering effect of the baseline during the event a "smart" baseline is also calculated for each channel within a window of 5 μs excluding data points greater than 5 RMS noise from the current value of the baseline.
- RMS noise level for each channel. $\text{Noise}_{\text{RMS}} = \sqrt{\frac{\sum h_t^2}{N}}$, where N is the number of samples in the pre-trigger region.
- Start time of all pulses on each waveform. The start time is define as the time when the smoothed pulses rises above the threshold
- Time of arrival of 10% of the pulsecharge, t_0 at which 10% of the total charge of the pulse is detected
- Width of each pulse in each channel. The pulse width is defined as the difference between the actual start time t_p (when smoothed pulse rises above the base line) and the actual end time.
- Area of each pulse in each channel. Pulse area (Vns) is defined as the integrated area of the pulse in the time window and is associated with the measurement of total charge of the signal. $A = \sum_{t}^{width} A_t$. Where A_t is the discrete area at time t.
- Height of each pulse (V) in each channel.

- Pulse FWHM measured from maximum pulse height. The width of a pulse at half of the maximum height.
- Charge mean arrival time

$$\tau = \frac{\sum_{t=t_0}^{t_p+width} h_t \cdot (t - t_0)}{\sum_{t=t_0}^{t_t+width} h_t}$$

- Start time of veto pulse
- Height of veto pulse
- Integrated area of veto pulse

CHAPTER IV

DATA SELECTION AND EFFICIENCES

The data streams and selection cuts used for both the ZEPLIN II published limit and the analysis presented in the next chapter were kept identical and are described in the following sections.

A. Data Streams

Three types of data were taken during the underground data run: gamma ray calibration data, neutron calibration data and WIMP search data.

Gamma calibration runs were performed daily using a ^{57}Co source. Typically twenty thousand events were taken within a few minutes. Two groups of data were taken that were trigged on primary and secondary scintillation, respectively. The primary (S1) spectrum of ^{57}Co γ-ray was used to determine the photoelectron yield and the energy resolution of the detector. The secondary (S2) signal was used to calibrate the position reconstruction as shown below. The ^{57}Co source was placed underneath the detector inner vessel; where the 122 keV and 136 keV gamma rays could penetrate through thinned places (holes) in the copper base. These gammas react within ~1 cm of the bottom. A ^{60}Co source producing 661 keV gammas was used to define the gamma band based on the ratio of ionization yield to scintillation light (S2/S1).

Neutron calibration was performed with AmBe sources to determine the nuclear recoil band. The discrimination power of nuclear recoils against gamma rays was

determined comparing the ^{60}Co and AmBe neutron data. This was used to define the nuclear recoil acceptance region for the WIMP search.

The WIMP search data analyzed in this dissertation consists of 3206 raw data files starting from 060515 through 060707, corresponding to a calendar time of 54 days. Each raw data file has 2000 events and a typical run lasting 18-20 hours. The livetime, defined as the sum of the time period of all analyzed events apart from maintenance and other calibration runs and test runs, was 31 days. The majority events are gamma ray background from radioactivity of contaminants in the detector components, surroundings and ^{85}Kr in xenon.

All of the data were taken underground at Boulby mine and processed with the software described in Chapter III.

B. Overview

Data analysis includes data processing, evaluation of detector performance, blind analysis, exposure determination, background estimation, and searching for the WIMP signal.

Three layers of science data were produced and analyzed. The first two were raw data and reduced ntuples (a database containing multiple records, with each record represents a group of physical variables for an event) as described in Chapter IV. The third derived ntuples contain only so called “golden” events which required that an event have one (and only one) S1 and one (and only one) S2. This rule applied to WIMP search data, AmBe neutron data and ^{60}Co gamma calibration data. ^{57}Co data, alpha events in the WIMP search data, and apparatus monitoring data were used to evaluate

the performance of the detector, including PMT response, noise, purity, pressure, electric field strength, diffusion and liquid level. S1 and S2 signals vary with these parameters and are also position dependent. In order to obtain homogeneous physical values, corrections were applied to the golden data before it was written out. Cut efficiencies were determined using calibration data, ten percent of the WIMP search data and simulations. To obtain unbiased cuts, a procedure of blind analysis was adopted so that potential WIMP signal events in the nuclear recoil region could not be examined until the cut definitions, cut efficiencies, and background estimation were finalized. Once data selection was finished and cuts (including the fiducial cuts) were defined, the effective exposure was determined. Neutron backgrounds from cosmic rays and radioactivity in rock at the depth of the Boulby Mine were simulated in detail. Other NR backgrounds caused by uranium or thorium decays and from radon daughter products were also estimated. The overlapping edge of the gamma band and possible small nuclear recoil background from the PTFE walls were thought to be the major backgrounds in the data.

C. Event Selection [86]

A good event is defined as having one and only one primary and one and only one secondary pulse as previously stated – the golden rule [86]. Valid events are defined by primary (S1) cuts and secondary (S2) cuts which are described in the following subsections. Events satisfying the golden rule are filtered into golden ntuples, which retains most of the information from the original ntuple plus several additional variables. Most importantly the ntuple includes corrections for pressure, purity, and liquid level. After that, fiducial cuts are applied.

In the golden ntuple, events are labeled by the unique identifier eventide which consists of an integer which concatenates the date, ntuple number and original event number, e.g. eventide=6061500091008 represents event 1008 in ntuple file 0009 from date 060615. The smaller integer evtdate and evtfile together with existing evnum provide a unique identify method while using interactive analysis tools. Figure 25 shows the content of the golden ntuple data.

1. Primary Pulse Cuts

a. Three-fold Coincidence

The primary S1 signal was required to be seen by at least 3 phototubes in coincidence. A cut at 1.7 mV applies to individual channels. Simulations show the efficiencies depend on size of the pulse. The efficiency is >95% for 12 keV_{ee} ($_{ee}$ refers to electron equivalent energy, the energy that would be observed from a recoiling electron) and higher energy bins.

b. First Pass S1 Depth Cut

This cut requires the time period between S1 and S2 is smaller than 73 us to remove non-physical events. Since the maximum drift time is ~80 μs. Efficiency ~100%.

Var numb	Type	Packing	Range	Block	Name
1	I*4			EVENT	EVNUM
2	R*8			EVENT	TIME
3	R*4			EVENT	TTARGET
4	R*4			EVENT	TAMBIENT
5	R*4			EVENT	PRESSURE
1	R*4			CHANS	BASELINE(8)
2	R*4			CHANS	NOISE(8)
3	R*4			CHANS	CHARGE10(8)
4	R*4			CHANS	CHARGE50(8)
5	R*4			CHANS	CHARGE90(8)
6	R*4			CHANS	FRONT(8)
7	R*4			CHANS	CENTRAL(8)
8	R*4			CHANS	BACK(8)
9	I*4			CHANS	NPULSES(8)
1	I*4		[0,10]	PULSES	NUMPULSES
2	R*4			PULSES	POSN(8,NUMPULSES)
3	R*4			PULSES	WIDTH(8,NUMPULSES)
4	R*4			PULSES	AREA(8,NUMPULSES)
5	R*4			PULSES	HEIGHT(8,NUMPULSES)
6	R*4			PULSES	TZERO(8,NUMPULSES)
7	R*4			PULSES	FFWHM(8,NUMPULSES)
8	R*4			PULSES	LFWHM(8,NUMPULSES)
9	R*4			PULSES	TAU(8,NUMPULSES)
10	R*4			PULSES	TPEAK(8,NUMPULSES)
11	I*4			PULSES	OFFEND(8,NUMPULSES)
12	I*4			PULSES	SAT(8,NUMPULSES)
13	R*4			PULSES	SHEIGHT(NUMPULSES)
1	R*4			VETO	VBASELINE
2	R*4			VETO	VNOISE
3	I*4		[0,10]	VETO	VNPULSES
4	R*4			VETO	VPOSN(VNPULSES)
5	R*4			VETO	VHEIGHT(VNPULSES)
6	R*4			VETO	VCHARGE(VNPULSES)
7	I*4			VETO	VLOGIC(VNPULSES)
1	R*8			S1S2	eventid
2	I*4			S1S2	evtdate
3	I*4			S1S2	evtfile
4	I*4			S1S2	s1id
5	I*4			S1S2	s2id
1	R*4			CORR	peakpmts1
2	R*4			CORR	peakpmts2
3	R*4			CORR	corchan(7)
4	R*4			CORR	coryieldz
5	R*4			CORR	energy
6	R*4			CORR	corpurity
7	R*4			CORR	corpressure
8	R*4			CORR	corfield
9	R*4			CORR	cordiffusion
10	R*4			CORR	corlevel
11	R*4			CORR	s1cal
12	R*4			CORR	s2cal
13	R*4			CORR	estar
14	R*4			CORR	s1weighted
15	R*4			CORR	s2weighted
16	R*4			CORR	s1area
17	R*4			CORR	s1tau
18	R*4			CORR	s2area
19	R*4			CORR	s2tau
20	R*4			CORR	dtime

Figure 25: Physical variables in “Golden Ntuple”.

c. Second Pass S1 Position Cut

Excludes the layer of xenon above the extraction grid. The electric field in that region is different from the bulk. This is only applied after the multiplicity cut, i.e. it removes events with a single S1. Efficiency ~100%.

d. Sparklers

Sparklers are fast pulses with high peaks. The nominal rate is ~100/hour at nominal field. The sparkler cut is actually NOT required since neutrons also cause pulses with short time duration. Fortunately other cuts reject these signals with high efficiency: the position cut removes 72% of sparklers; adding the 3 fold coincidence leaves 0.6%. These are likely to have another S1 and are not likely to have a valid secondary.

e. S1 Timing

Single photo electron (SPE) data shows a minimum width (tau) of S1 of 3 ns, confirmed by zero-field neutron data. Science data shows that real primaries are faster than 50 ns. This cut is used to removed certain S1-like signals showing a fast pulse and a slower tail, consistent with a primary in near coincidence with single-electron extraction ("S1e1" events) have time duration 50 ns<tau<150 ns. Very few S1e1 pulses have an additional good secondary. This may suggest that these pulses consist of a sparkler plus single electron extraction, or very low energy primaries on top of a small secondary, perhaps due to PMT x-rays interacting at the Xe surface. Efficiency is ~100% for 3 ns<tau<50 ns.

f. S1 Multiplicity Cut

The S1 multiplicity was studied by plotting the number of primaries when a

single secondary is observed. Including all energies, an efficiency of 96.5% is obtained (fraction of events with a single primary to those with any number of primaries). In the 5-50 keV_{ee} (electron equivalent) energy range, the efficiency rises to 98.7%.

2. Secondary Pulse Cuts

a. S2 "Size" (Energy) Cut

This cut requires S2 area greater than 1 Vns so it removes very small electroluminescence pulses caused by single electrons extracted from the LXe These occur in spite of valid S2 pulses and can be seen as late as tens of milliseconds after large S2 pulses from high-energy gammas. 1Vns corresponds to ~27 photo electrons. The efficiency is 90.3% for 5-10 keV_{ee}, 99.7% for 10-15 keV_{ee} and ~100% for higher energy bins.

b. S2 Width Cut

The width of the S2 pulse is determined by the time duration of the electro-fluorescence caused by the cluster of ionization electrons moving from the LXe surface to the anode. The width of the point-like ionization deposits grows as a function of drift time because of diffusion. A first pass width cut between 200 and 600 ns selects secondaries with 100% efficiency. After selection of golden events, the diffusion correction is applied and the tails in the diffusion-corrected widths are cut (requiring the width between 250 ns and 400 ns) to retain about 90% efficiency. This was calculated from Am-Be data after applying the first pass cuts, using events below 30 keV in 5<drift time<65. Efficiency of this cut is 90.2%.

c. S2 Timing Cut

The secondary drift time can only vary between the trigger point and ~73 us after the trigger point. This is not a fiducial or depth cut, it is used to remove non-physical drift times from, for example, overlapping events. Efficiency is 100%.

3. Data Corrections

Once events pass the golden selection cuts several corrections are applied before the ntuple is written out. The following corrections and calibrations are applied and stored in new variables.

a. PMT Equalization

SPE areas were equalized to first order by adjusting the high voltage and the PMTs. They are equalized further in software so that summed signals do not depend on the light distribution in the PMTs. The relative PMT quantum efficiencies are also used to adjust the pulse areas.

b. S1 Z-dependence Correction

Simulations predict a slight increase in light collection towards the bottom of the target, depending on the LXe purity (photon absorption length). However, the S1 yield from alpha events distributed throughout the liquid shows little variation with z for data with good to very good electron lifetime. The yield is slightly higher in the middle, decreasing toward the top and bottom. Although better purity does improve the yield from the bottom of the basin, this effect is very minor.

c. Energy Calibration

The light yield is quite constant over the relevant period of time. A single value

(122.06/2.53 keV_{ee}/Vns) obtained from 122.06 keV ^{57}Co line is used to convert the pulses area to energy.

d. Purity Correction

Ionization electrons are absorbed while drifting toward the gate due to electro-negative contaminants in the LXe, resulting a reduced S2 signal. The S2 signal is corrected with a factor exp(dtime/lifetime). The lifetime is read out from a database derived from two-point exponential fits (using recoil events from the extraction cathode grids) to 4-5 hr bins. It must be noted that the electric field for recoils near these two grids should be significantly higher than in the bulk. However, the median lifetime in the database is in very good agreement with that obtained by looking at the combined purity of the whole golden dataset.

e. Pressure Correction

The pressure affects the S2 light yield and causes the liquid level to vary. It was first thought that the pressure variation was too quick for the liquid temperature to follow (near-isothermal conditions). However, the system was near thermal equilibrium. The S2/S1 for nuclear recoil background varies with pressure in a similar way to ^{57}Co data. AmBe and ^{60}Co data were not pressure corrected – this was taken care of by S2 absolute correction in the two datasets as described below.

f. Diffusion Correction

The pulse width parameter tau as a function of drift time shows a clear variation due to increased vertical charge diffusion with depth. The width is corrected with a factor: $1./(1.+4.8\cdot10^{-6}\cdot dtime)$. This correction is applied as follows: the uncorrected tau

parameter is used for an initial S2 selection, with practically unity efficiency. Then tau is re-calculated and a narrower cut is applied so that only 90% of events are retained.

g. Anti-correlation Correction

Ionisation electrons produced at the interaction site contributes to either S1 or S2 – these signals are anti-correlated. If an electron remains free, it contributes to S2, if it recombined it contributes to S1. An approximate correction assumes that both S1 and S2 channels have the same electron gain, i.e. one recombining electrons added to S1 is exactly one inoisation electron removed from S2. Although this is not strictly correct, this assumption improves the energy resolution considerably. The S1 and S2 peaks obtained with the ^{57}Co calibration provide a method to calculate a new estimator for the energy deposited.

h. Liquid Level Correction

Xenon temperature variations lead to thermal expansion and contraction of the liquid which affect the gas gap and therefore S2 gain. Liquid level variations are correlated to pressure variations, i.e. changes in S2 yield through liquid level can be corrected through the pressure itself.

i. S2 Absolute Corrections

S2 gain corrections excluding pressure/level are done using the NR population from the cathode – which we assume inject a constant charge spectrum with time. This deals with the very important “charging correction”, which is vital when the grids are first turned on, as well as more general field variations, and imperfect purity, pressure and level corrections. Double Gaussians are fitted to S2/S1 in cathode events with drift

time > 65 μs and 0.2<area<0.8 (10<keV$_{ee}$<40). A database of <S2/S1> (t) of time-sliced cathode spectra was produced. These values are then corrected for the mean lifetime measured for each database entry and then pressure-corrected using the mean pressure. At this stage the database contains bottom recoils at infinite purity normalized to 1.5 bar. The ntuples are then corrected event-by-event by interpolating between adjacent database entries.

4. Fiducial Cuts

a. Fiducial Cut in Z

This cut requires drift time less than 64 μs. To calculate the fiducial mass, an average equilibrium pressure of 1.6 bar (for which the LXe density is 2.88g/cm^3) was used. The drift time from the cathode grid is 73 us, and about 3 us from the bottom grid – so the net drift time for the 14 cm total drift region is 70 us, corresponding to a speed of 2.0 mm/us (at 1 kV/cm).

The total mass is calculated a for a conical frustum between R_1 = 143mm (bottom) and R_2 = 162 mm (top), with height h = 140 mm:

$$V = (1/3)\pi h\left(R_1^2 + R_2^2 + R_1 R_2\right) \tag{4.1}$$

The total mass inside the PTFE is ≈ 31kg (0-field operation), and 26 kg for 4<dtime<64 us. (Δz = 120 mm).

b. Fiducial Cut in X, Y

X and y are reconstructed as $\sum_i^7 c_i x_i \Big/ \sum_i^7 c_i$ and $\sum_i^7 c_i y_i \Big/ \sum_i^7 c_i$, where x_i, y_i are positions of 7 PMTs and c_i are S2 areas detected in the PMTs. Most wall events can be

rejected with a cut at $r_w=\sqrt{x^2+y^2}$ <0.467. Using the function, the centers of the inner holes at the bottom of the Xe vessel (75mm radius) appear at 0.444.

A new position reconstruction algorithm using Geant4 simulations will be discussed in the next chapter.

c. Nuclear Recoil Acceptance Window

The acceptance window extends between 5-20 keV_{ee} in energy and up from S2/S1 = 40 to achieve an acceptance fraction F in each energy bin. Alternative windows can be calculated with the help of Table VI, for NR acceptance between S2/S1 = 40 and an arbitrary fraction of the nuclear recoil population from Am-Be data. The parameters S2/S1 and σ in Table VI were produced by slicing and Gaussian fitting of the energy ranges. The table also shows the S2/S1 values which solve the following equation.

$$F = \int_{40}^{x} \frac{1}{\sqrt{2\pi\sigma}} \exp\left(-\frac{\left(x' - x_0\right)^2}{2\sigma^2} \right) dx' \tag{4.2}$$

The NR band and acceptance box is plotted in Fig. 26.

Table VI: S2/S1 values for given NR acceptance from S2/S1>40.

keV_{ee}	S2/S1	σ	50% 40% 30% 20% 10%
5-7	124.7±6.8	74.9±6.6	149.4 130.2 111.3 91.6 69.1
7-9	119.9±3.4	56.9±3.0	131.4 117.1 102.6 86.8 67.9
9-11	112.1±3.0	49.6±3.1	121.2 108.7 96.0 82.1 65.4
11-13	99.8±2.4	37.4±2.2	105.0 95.5 85.9 75.1 61.8
13-15	105.1±2.2	32.6±2.2	107.0 98.8 90.1 80.2 67.3
15-17	95.1±2.8	34.0±3.5	99.6 91.1 82.2 72.5 60.2
17-19	92.2±2.2	26.5±2.2	93.8 87.2 80.2 72.2 61.7
19-21	88.3±1.9	24.5±1.6	89.8 83.7 77.2 69.8 60.0
21-23	89.0±2.6	27.1±2.9	91.4 84.6 77.5 69.4 59.1
23-25	80.9±2.3	23.4±2.0	83.3 77.4 71.3 64.4 55.7

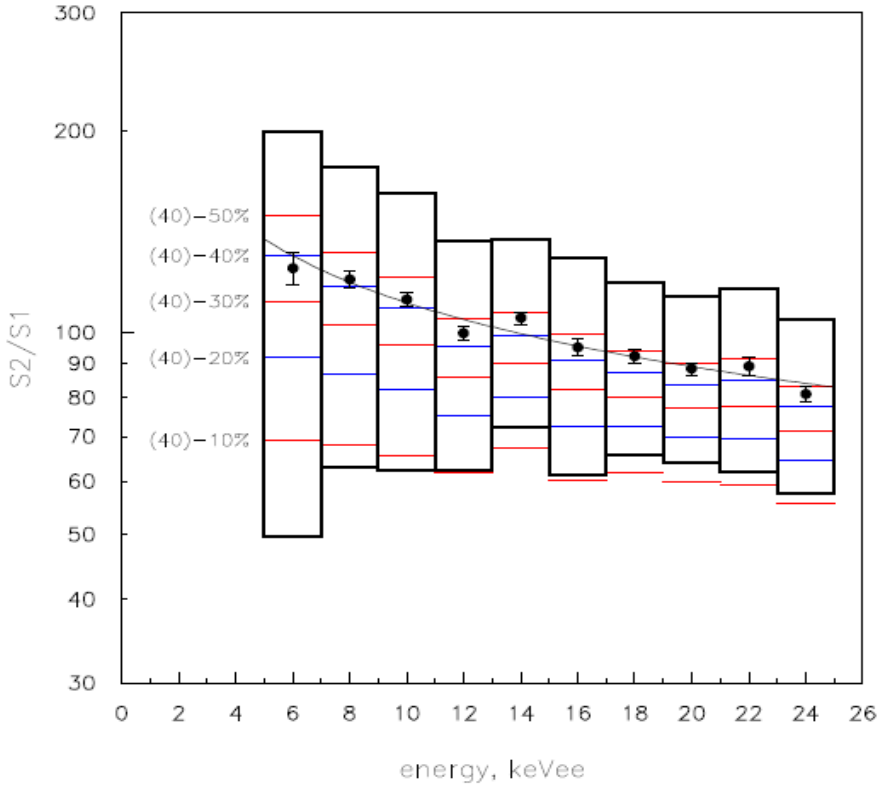

Figure 26: Nuclear recoil band from AmBe calibration. The black dots are mean value of Gaussian-fitted slices with width of 2 keVee. Rectangles the width of the distributions of each slice. The colored bars show the S2/S1 value where the distribution integrates to a certain percentage from S2/S1=40 [86].

5. Hardware Cuts

a. Saturation Cut

The hardware and software saturation cuts eliminates signals exceedging the limit of the digitizers and thus affect signals above the energy range of interest. The effect is quantified as a function of energy as shown in Fig. 27. Efficiency is 100% up to 30 keV_{ee} [86].

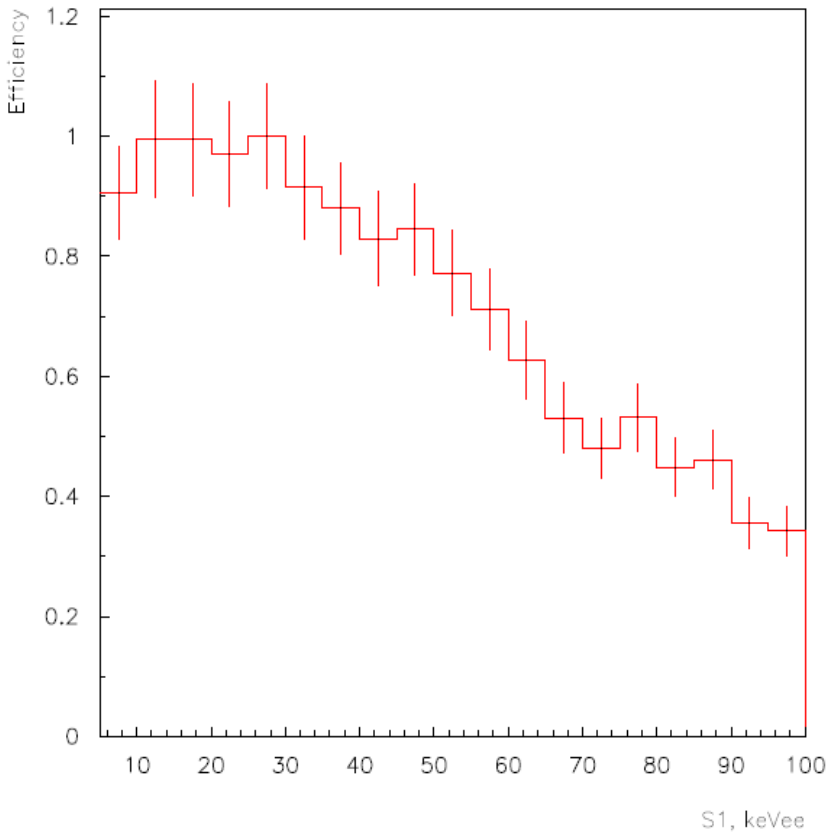

Figure 27: DAQ saturation cut efficiency.

b. Dead Time

In WIMP search runs, the dead-time fraction from the Acqiris-PCI bottleneck (hard disk write time) is small but not negligible especially for two-phase Am-Be and ^{60}Co calibration data. In a non-paralysable model (dead-time not extended by events occurring within the inhibit time) the measured rate, m, is given by $m = n / (1+n\tau)$, where τ is the dead-time and n is the true event rate. Conversely, $n = m / (1-m\tau)$. The fraction of events retained efficiency is then $m/n = 1/ (1+n\tau)$.

The maximum observed rate in the dataset is 20 Hz (τ = 50 ms) for events

triggering the Acqiris. Applying this value to data runs, with a recorded rate m~ 2 Hz, the dead-time fraction is ~ 10% (efficiency = 90%).

c. Veto

A large population of events with veto signals in near coincidence with the primary is due to neutrons and gammas double scattering in the target and the veto counter. A smaller population with an exponential fall-off after the primary is due to neutron capture in the veto. Efficiencies are derived from the probability of accidental coincidence. The probability of a random coincidence between the liquid scintillator Compton veto and target is calculated from the veto rate, the veto trigger pulse width and the search window defined around a primary. From the measured veto trigger rate, the true trigger rate is calculated (see section on deadtime) and used to generate the Poissonian probability of seeing no random veto events during the specified search window. Although the veto pulse is taken into account by calculating the true rate, a conservative approach is to assume that another event could have occurred at any time during the 400 ns veto pulse. To account for this the search window and veto pulse width are added in quadrature. Efficiencies are 99.2% for WIMP data.

6. Additional Software Cuts

Some additional cuts are applied after generation of the golden ntuples as follows.

a. Trigger Point Cut

In a golden event either S1 or S2 should trigger the DAQ with high probability. Efficiency is ~ 100%.

b. Cathode Cut

This cut removes events from the cathode which have a small, twofold primary and are therefore too small for golden primary cuts. For some events, a random coincidence occurs with another primary (with no secondary) and this primary is wrongly associated with the secondary, producing a wrong drift time. This is much more likely to occur with events from the cathode, as the recoil primaries from the cathode can be very small. The function searches a region of drift time between 66 and 73 us before S2, and looks for two-fold coincidence is found, the event is cut, as this would lead to two primaries, excluding it by the golden rule.

This cut was tested by moving the 7us search window along the timeline to different drift times. Only 0.3% of golden events are cut when applying the function to the fiducial bulk – and we assume this to be the NR efficiency – with many more events being correctly cut at the cathode.

7. Combined Efficiencies

Take nuclear recoil energy keVnr = keV_{ee} / QF * (f_e / f_n), where QF =0.19 is the zero field quenching factor, f_e =1/2.02 is the field induced suppression of scintillation for electron recoils obtained from ^{57}Co calibration, and f_n = 0.93 at 1 kV/cm is the field induced suppression for nuclear recoil scintillation. Hence:

keVnr = 2.8 * keV_{ee} .

The overall efficiency is shown in Fig. 28 as a function of $keV_{ee.}$

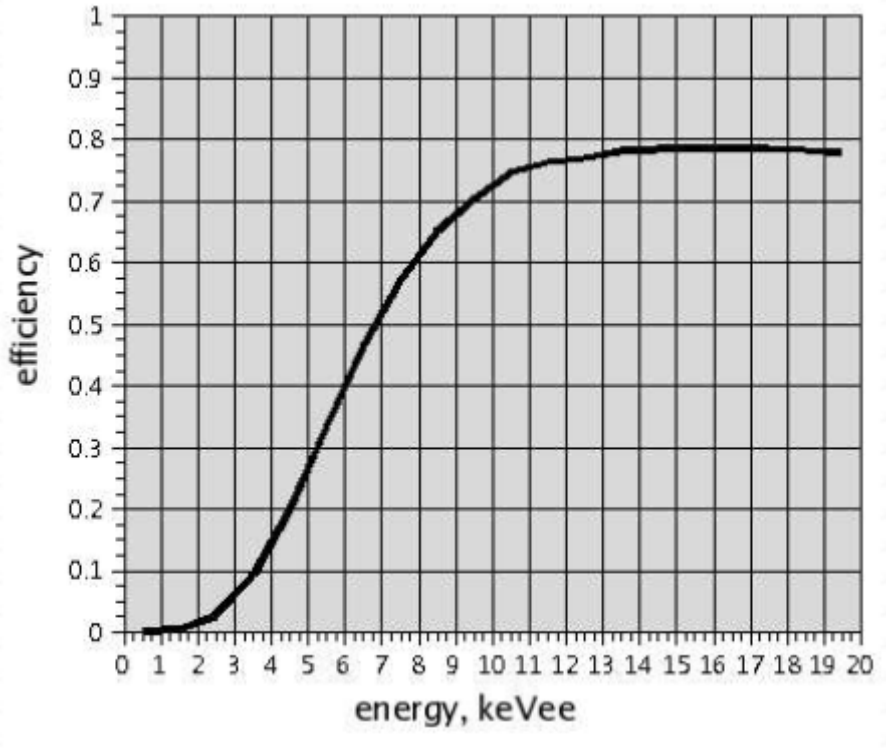

Figure 28: Summary of efficiencies [86].

CHAPTER V

POSITION RECONSTRUCTION USING A χ^2 METHOD

The ZEPLIN II data is reanalyzed with a new x,y position reconstruction based on a χ^2 method. This was done for two important reasons. The first was to verify that the fiducial volume determined for the ZEPLIN II limit [87] was correct within uncertainties. And second, to investigate the origin of the small S2 events. The new approach should have significantly improved resolution near the walls and therefore provide a method to remove such events.

An S2 signal is recorded by 7 PMTs at the top of the detector. The fractional light observed by the PMTs is unique for an individual position in the xy plane of the electro-luminescence region. The distribution of S2 in the PMTs is determined by the properties of the detector, including the geometry and optical properties of the PTFE walls, the material near the PMTs, and the transmission of the grids. The position reconstruction discussed in the previous section was based on a simple weighted method. Because of the size of the PMT photocathode and the limited number of PMTs, the xy reconstruction is nonlinear and distorted. This section focuses on the how detector properties affect the light collection and uses a χ^2 method for event position construction based on Geant4 simulation. Golden data are used and the result is compared to the result obtained from the weighted position reconstruction.

A. The Geant4 Simulation

Particle transport simulation code such as Greant4 [88] simulates the passage of

particles through matter in the experimental set-up and track the energy deposition. The Geant4 tool kit provides all aspects of the simulation process including: the geometry of the system, the materials involved, the particles definition, the generation of primary events, the tracking of particles through materials and electromagnetic fields, the physics process governing particle interactions, the response of sensitive detector components, the generation of event data, the storage of events and tracks, the visualization of the detector and particle trajectories and the capture and analysis of simulation data at different levels of detail and refinement. A Geant4 user encodes the experimental configuration using a structure of geometrical volumes by defining the shape, material and tracking-medium parameters, and then simulates the transport of particles drawing physical processes detailing their interactions with matter. An event includes all processes, including the production and interactions of secondary particles, that occur between successive throws of a primary particle. An ntuple saves information about all events that cause energy to be deposited in the detectors. This includes information about the type of incident particle and its energy, as well as the energy deposited in the detectors by the particles for that event.

B. Set up the Geometry

The first step in Geant4 simulation is to model the experimental construction. For the simulation of ZEPLIN II, the modeling involved almost every single component in the detector starting from the outside vacuum vessel. A critical part of the simulation is the tracking of scintillation light from production to arrival at the PMTs. This depends strongly on the optical properties of the various PTFE surfaces and the absorption in the

grids. An example event simulation is displayed in Fig. 29.

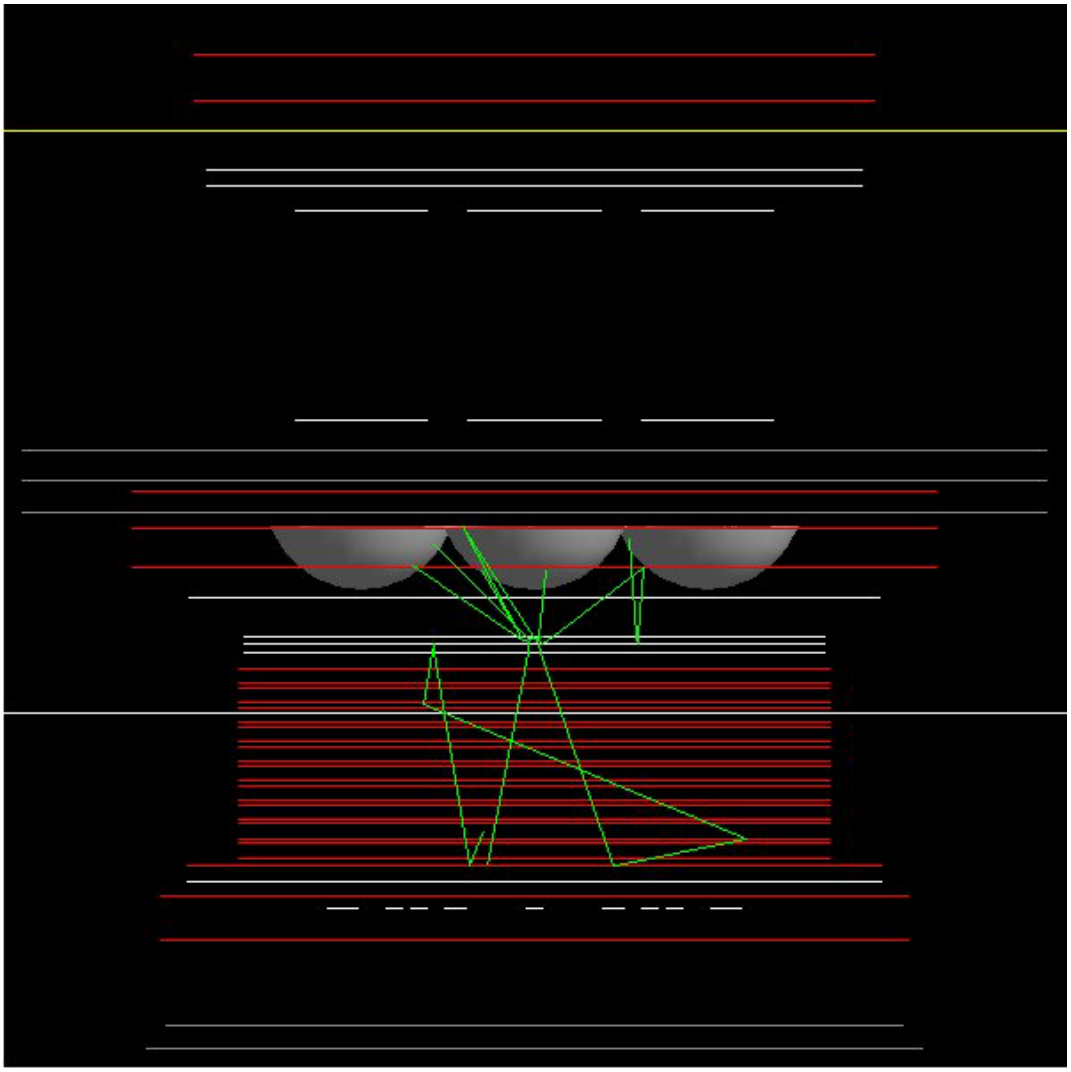

Figure 29: An example of ZEPLIN II Geant4 simulation event display. The grey hemispheres are PMTs. Red lines under the PMTs are field rings surrounding the target. The ten green lines are transport trajectories of the optical photons.

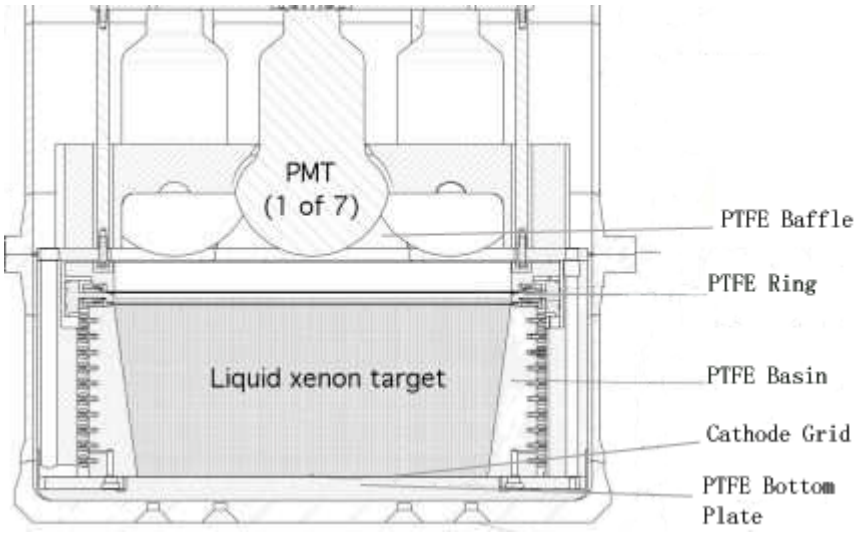

Figure 30: Inner parts of the detector that affect light collection efficiency.

1. Reflectivity of PTFE Surfaces

The surfaces surrounding the target xenon include the PTFE basin, the PTFE bottom plate, the upper PTFE baffle that holds the PMTs, the PTFE ring holding the anode and extraction grids that sit on top of the basin, and the PTFE ring between the baffle and the anode grid (Fig. 30). The reflectance properties of PTFE were measured for a spectral range of 200 to 2500 nm [89]. From a simple extrapolation, the reflectance at 175 nm is expected to be 95%. The diffuse reflectance is 82.6% according to Miyajima et al [90] and specular reflection makes up the difference. The actual value of reflectivity and diffusion for the PTFE used in ZEPLINII can be affected by the procedure of manufacturing and the dirt or oil on the surface. To simulate the optical boundary process, the UNIFIED model [91] was used. It applies to dielectric-dielectric interfaces and tries to provide a realistic simulation which deals with all aspects of surface finish and reflector coating. The surface may be assumed as smooth and covered

with a metallized coating representing a specular reflector with given reflection coefficient, or painted with a diffuse reflecting material where Lambertian reflection occurs. The surfaces may or may not be in optical contact with another component and most importantly, one may consider a surface to be made up of micro-facets with normal vectors that follow given distributions around the nominal normal for the volume at the impact point. For very rough surfaces, it is possible for the photon interact with the surface more than once at the same location.

In the UNIFIED model the specular lobe constant represents the reflection probability about the normal of a micro facet. The specular spike constant, in turn, illustrates the probability of reflection about the average surface normal. The diffuse lobe constant is for the probability of internal Lambertian reflection, and finally the back-scatter spike constant is for the case of several reflections within a deep groove with the ultimate result of exact back-scattering. The four probabilities must add up to one, with the diffuse lobe constant being implicit.

C. Determination of the Optical Properties of the PTFE

In the study presented here, the optical properties including diffuse reflectivity, specular reflectivity, and grid transmissivity were varied to find the best fit to the ^{57}Co calibration data. Millions of optical photons are generated from a small region between the anode grid and the extraction grid with fixed x and y position, and the number of photons detected by each PMT is recorded. This process is repeated for a lattice of 3284 points with 0.5 cm spacing in both x and y directions. A data file is created that contains the 3284 positions with mean PMT response for each position. To evaluate each set of

parameters, a χ^2 was defined for events in the golden and calibration data and in simulated data as following:

$$\chi^2 = \frac{1}{N-1}\sum_{i=1}^{7}\frac{\left[S_i - S_i^{'}\right]^2}{S_i^{'}} \tag{4.3}$$

where N-1=7-1 is the number of degrees of freedom, S_i is the normalized (in fraction of total S2) S2 signal for i-th PMT in the real data, and $S_i^{'}$ is the normalized S2 signal for i-th PMT from simulation.

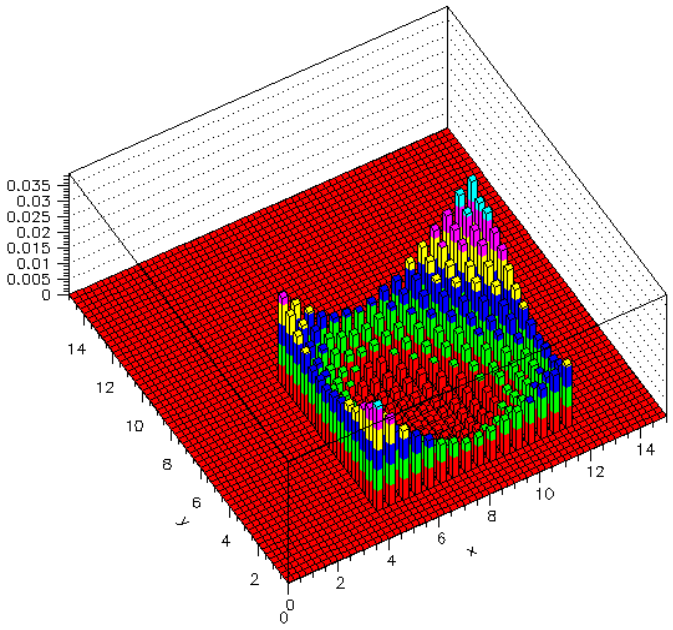

Figure 31: Lego plot of χ^2 for an event.

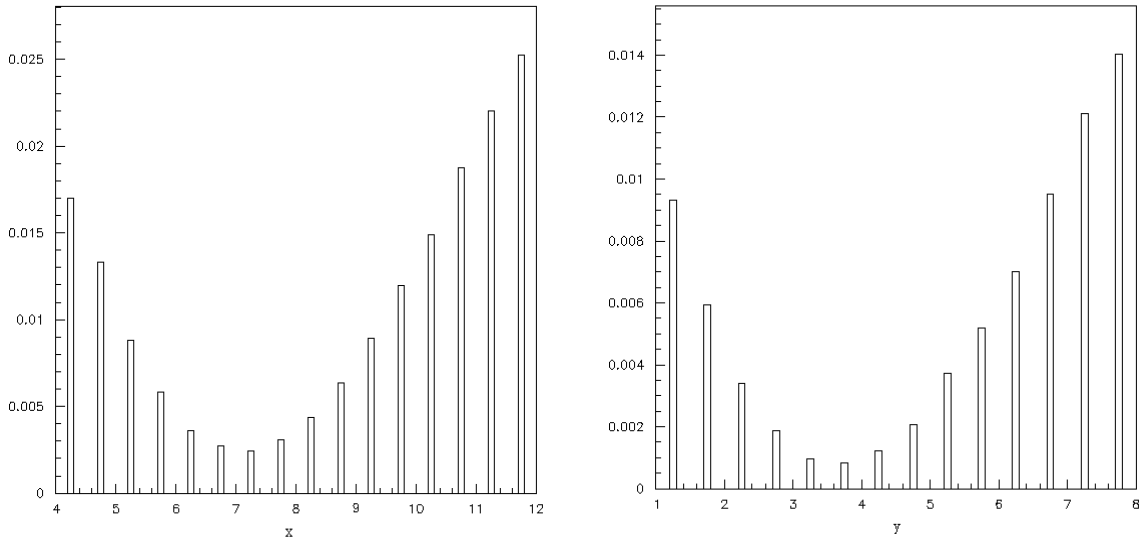

Figure 32: Slice view of χ^2 distribution along x and y.

Figure 31 is an example of the χ^2 distribution of an event as a function of x and y. A minimum is clearly evident. Figure 32 shows the x and y slices through the minimum. To find the minimum χ^2, a grid search method was used. It starts from the center and searches for the smallest χ^2 along x axis, then searches along the y axis to find the least χ^2. The procedure is iterated until it finds the smallest χ^2. Then the adjacent three positions are used to do a parabolic fit to return the minimal χ^2, along with the extrapolated x and y positions. For each set of parameters a distribution of χ^2 is obtained that can then be tested. Figure 33 shows a comparison of the χ^2 distribution for two sets of parameters. Results of the different chosen parameter sets are presented in Table VII.

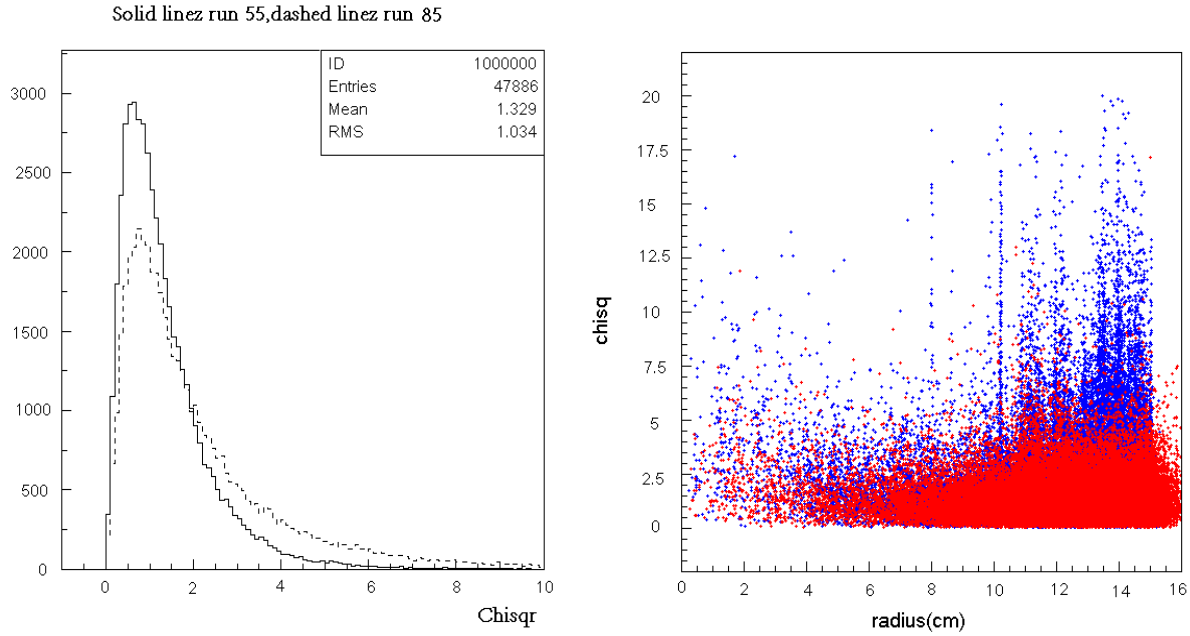

(a) (b)

Figure 33: Comparison of χ^2 test for two sets of parameters. (a) shows the distributions of χ^2 for simulation run 55 (solid) and 85 (dashed) as indicated in Table VII. (b) shows the distribution as a function of distance from the center. Red events are from run 55 and blue ones from run 85.

Table VII: List of simulations with different parameters of optical properties and χ^2 test. Rt is the total reflectivity of the all the PTFE parts except the PTFE ring that supports the anode and extraction grid; Tc is the cathode transmissivity; Rr is the ring reflectivity; D is the percentage of diffuse reflection on cone, the baffle, and the ring.

Simulation Run Number	Rt (%)	Tc (%)	Rr (%)	D (%)	χ^2 (mean)
84	90	90	90	100	1.876
85	90	90	90	80	1.993
86	90	90	90	60	1.836
81	90	90	0	100	1.666

Table VII. Cintinued

Simulation Run Number	Rt (%)	Tc (%)	Rr (%)	D (%)	χ^2 (mean)
82	90	90	0	80	1.725
83	90	90	0	60	1.964
31s	90	90	10	80	1.516
34s	90	90	10	60	1.624
37s	90	90	10	40	1.610
40s	90	90	10	0	1.687
74	90	75	90	100	1.630
75	90	75	90	80	1.663
76	90	75	90	60	1.735
71	90	75	0	100	1.454
72	90	75	0	80	1.464
73	90	75	0	60	1.580
32s	90	75	10	80	1.425
35s	90	75	10	60	1.504
38s	90	75	10	40	1.486
41s	90	75	10	0	1.537
54	90	60	90	100	1.549
55	90	60	90	80	1.542
56	90	60	90	60	1.617
51	90	60	0	100	1.458
52	90	60	0	80	1.444

Table VII. Cintinued

Simulation Run Number	Rt (%)	Tc (%)	Rr (%)	D (%)	χ^2 (mean)
53	90	60	0	60	1.376
33s	90	60	10	80	1.444
36s	90	60	10	60	1.470
39s	90	60	10	40	1.513
42s	90	60	10	0	1.484
64	75	90	75	100	1.564
65	75	90	75	80	1.619
66	75	90	75	60	1.862
61	75	90	0	100	1.650
62	75	90	0	80	1.498
63	75	90	0	60	1.489
44	75	75	75	100	1.513
45	75	75	75	80	1.488
46	75	75	75	60	1.532
41	75	75	0	100	1.458
42	75	75	0	80	1.444
43	75	75	0	60	1.429
34	75	60	75	100	1.461
35	75	60	75	80	1.463
36	75	60	75	60	1.489
31	75	60	0	100	1.520

Table VII. Cintinued

Simulation Run Number	Rt (%)	Tc (%)	Rr (%)	D (%)	χ^2 (mean)
32	75	60	0	80	1.469
33	75	60	0	60	1.456
24	60	90	60	100	1.543
25	60	90	60	80	1.490
26	60	90	60	60	1.676
21	60	90	0	100	1.565
22	60	90	0	80	1.547
23	60	90	0	60	1.479
14	60	75	60	100	1.565
15	60	75	60	80	1.568
16	60	75	60	60	1.512
11	60	75	0	100	1.628
12	60	75	0	80	1.600
13	60	75	0	60	1.575
4	60	60	60	100	1.645
5	60	60	60	80	1.590
6	60	60	60	60	1.604
1	60	60	0	100	1.668
2	60	60	0	80	1.666
3	60	60	0	60	1.606

Table VIII: List of parameters of optical properties and χ^2 test for the best ten combinations. The selected simulations were performed again with more data and therefore have better results.

Simulation run number	Rt (%)	Tc (%)	Rr (%)	D (%)	χ^2 (mean)
33	90	60	10	80	1.397
55	90	60	90	80	1.459
71	90	75	0	100	1.360
72	90	75	0	80	1.389
32	90	75	10	80	1.459
42	75	75	0	80	1.356
43	75	75	0	60	1.338
52	90	60	0	80	1.321
53	90	60	0	60	1.317
51	90	60	0	100	1.329

The ten combinations of parameters that gave best χ^2 were processed again with improved statistics. They are listed in Table VIII. The χ^2 distribution for run 55 is shown in Fig. 34 along with the χ^2distribution of the 29 WIMP candidate events.

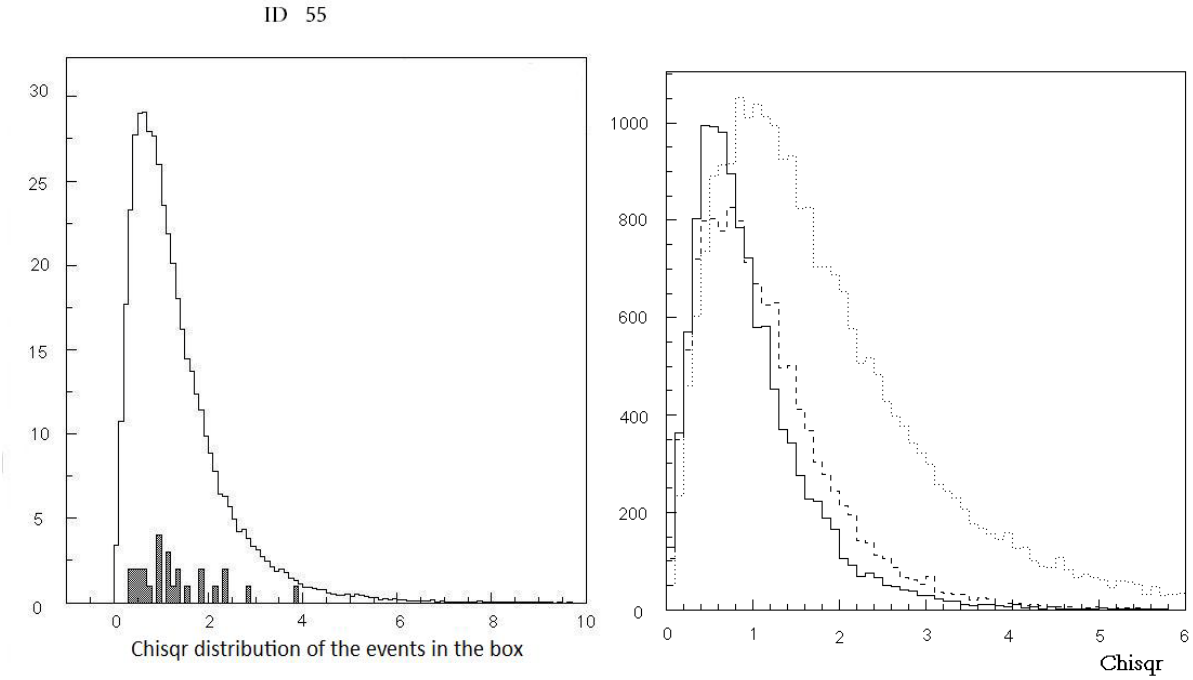

(a) (b)

Figure 34: χ^2 distribution for run 55 along with the χ^2distribution of the 29 WIMP candidate events. (a) is the χ^2 distribution of the 29 events in the WIMP acceptance window (shadowed events). (b) shows the χ^2 distribution for events grouped in different energy ranges: solid line s2<6 (V·ns); dashed line 6(V·ns)<s2<30(V·ns), and dotted line s2>30 (V·ns).

The results show an interesting effect that the simulation prefers low light reflection for the PTFE ring that is located between the PMT supporting baffle and the top of the main PTFE basin. Further simulations showed that it gave an even better result if there is an absorber near the top of the PTFE ring (Fig. 35). The cause could be dust that is floating on the surface of the LXe close to the PTFE ring. This would greatly reduce the reflectivity.

The results also show that total internal reflection (TIF) on the PTFE is negligible although the refractive index is 1.56 for LXe and 1.35 for PTFE. However this depends

on the type of PTFE. PTFE is produced in two distinct types designated "granular PTFE" and "fine powder PTFE" which have quite different properties. Also whether the surface is machined or produced by rolling makes a difference. TIR has been observed on a “fine” powder PTFE. The cathode transmission rate is less than 85% (the percentage of open area of the cathode grid), which indicates that the reflectivity on the bottom PTFE plate is reduced due to the dirt with high density that settled on the bottom.

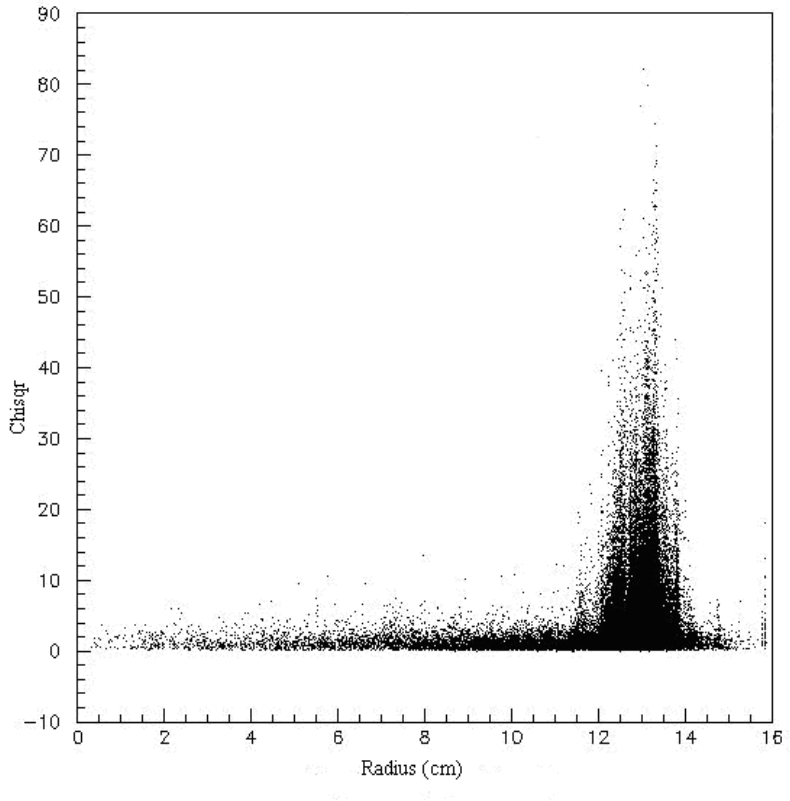

Figure 35: χ^2 distribution as a function of radius r for a simulation in which the PTFE baffle has zero reflectivity (photons reached the baffle were absorbed) and the PTFE ring between the PMTs and the grids was missing.

CHAPTER VI

RESULTS AND CONCLUSION

WIMP search data from the complete 225 kg·day exposure are applied with all the data cuts, secondary signal corrections and normalizations as described in Chapter IV. The data are shown in Fig. 36 with the nuclear recoil acceptance window. In total 29 events are seen within this window. More information of the WIMP candidate events is listed in Appendix A. These events are believed to consist of the overlapping edge of the γ-ray band at the top of the acceptance region along with a population of small S2 events at the bottom. These events at the bottom of the band were believed to be derived from radon nuclei decaying within the active volume. The subsequent alpha decays along the Rn-chain cause recoiling nuclei to enter the liquid xenon volume from the PTFE wall. Due to either the incomplete charge extraction on the wall or the charge stripping as the electron cloud drifts to the xenon surface, the S2 signal is reduced. As a result, these events have poor position reconstruction accuracy.

A. The Fiducial XY Cut and the Limit

Once the optimal optical parameters were found as described in the previous chapter, new x,y positions were obtained to check the resolution and efficiency of the method. A Monte Carlo (MC) set was generated with random position and energy in the range of 0-2 keV_{ee}. The reconstructed positions are compared to the generated positions in Fig. 37.

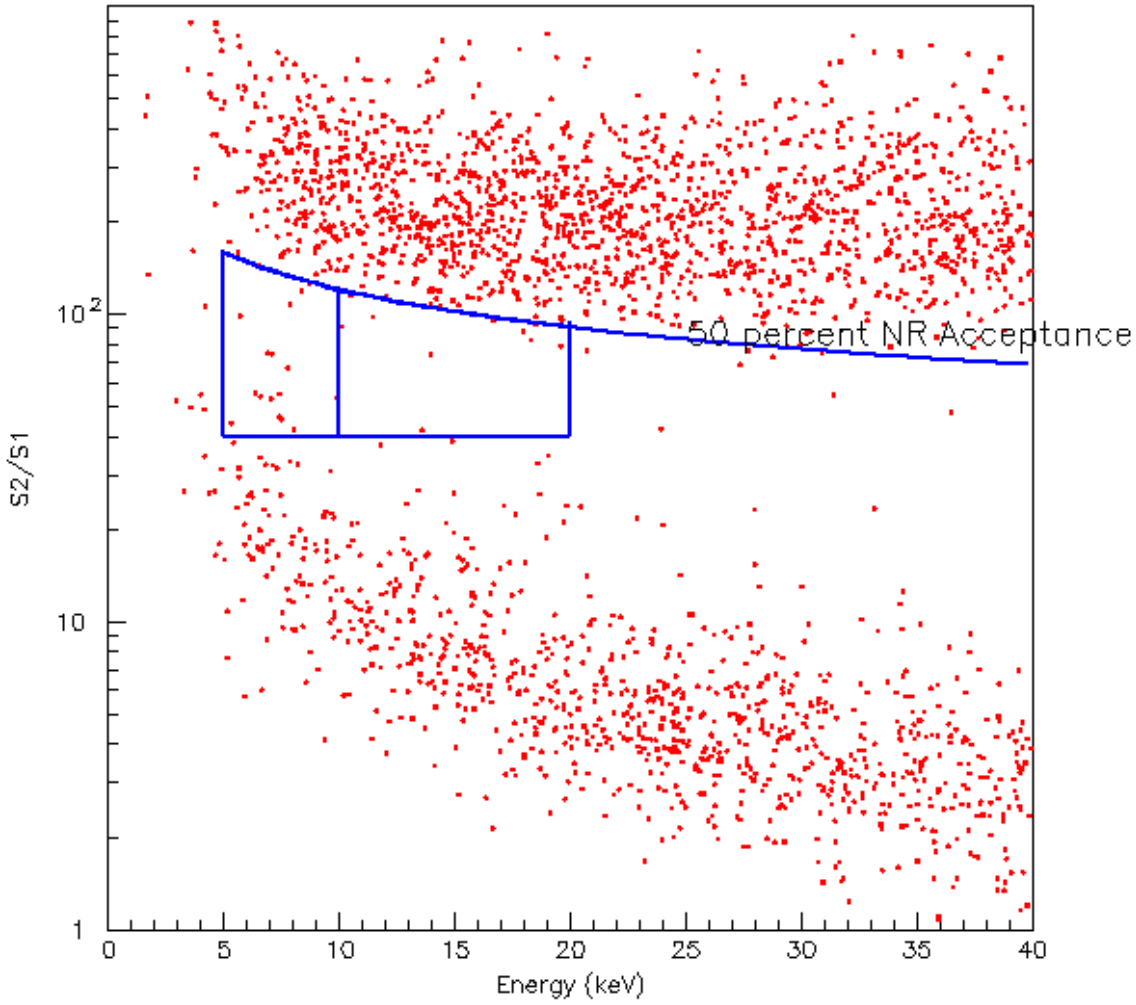

Figure 36: ZEPLIN II complete 225 kg·day exposure result. The acceptance box was determined using 10% of the WIMP search data along with neutron calibration data.

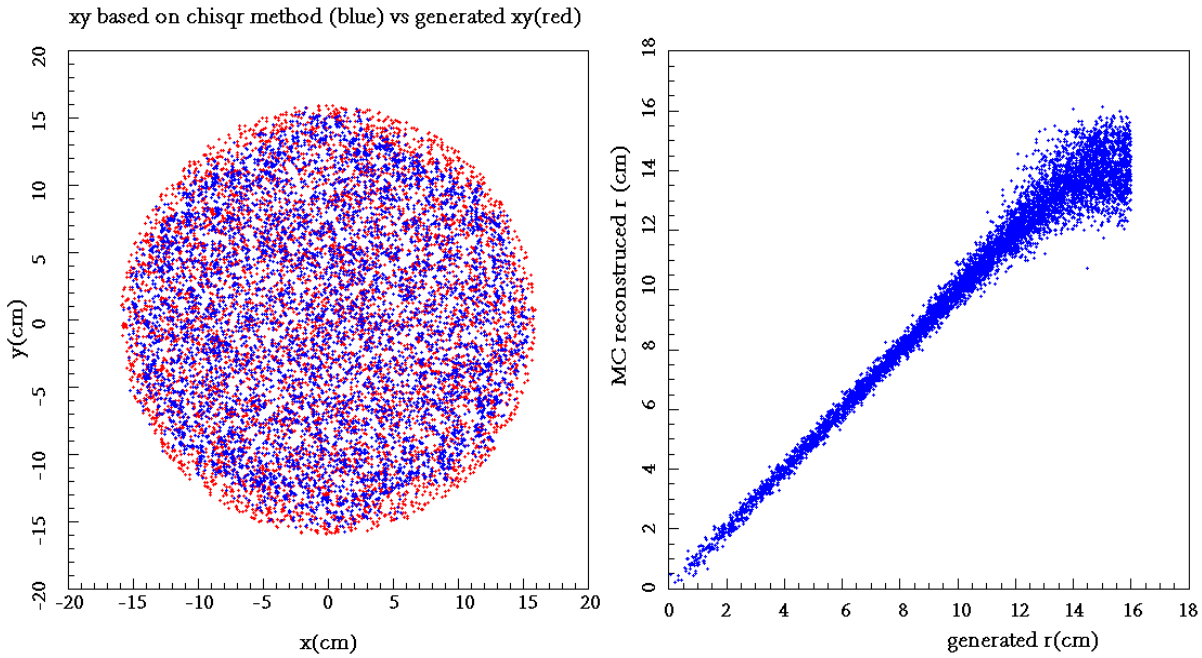

(a) (b)

Figure 37: Comparison of reconstructed positions to the generated positions. (a) shows the reconstructed positions (blue) compared to the generated positions (red). (b) shows the reconstructed radius vs the generated radius. The grid searching algorithm for minimal χ^2 at the edge the target becomes inefficient because the searching iterations sometimes do not return the minimum value. The radius cut for the ZEPLIN II published limit corresponds to approximately 8 cm as can be seen in the next figure.

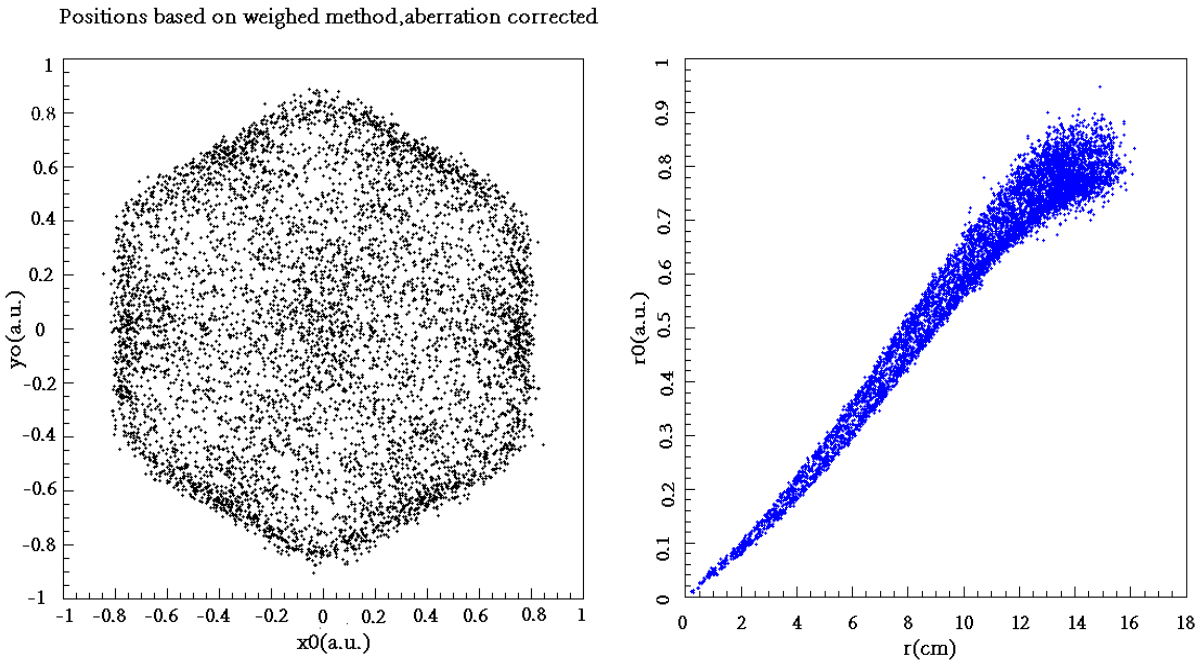

(a) (b)

Figure 38: Reconstructed positions using weighted method. (a) shows the positions reconstructed with the weighted method for all the MC generated events evenly distributed in the detector. The PMT position in the MC are (0,0), (2,0), (1, -1.73), (-1, -1.73), (-2,0), (-1, 1.73), (1,1.73). The hexagon shape shows event positions shrink under the PMTs. (b) shows the scatter plot of reconstructed radius using the weighted method vs the generated radius. The radius cut for the published limit was r0 < 0.467 which corresponds to roughly 8 cm.

Similarly, the position of the MC events were determined using the weighted method is shown in Fig. 38. The χ^2 method was also used to analyze the ^{57}Co γ-ray calibration data. The reconstructed positions of ^{57}Co γ-rays are shown in Fig 39. The inner ring of holes appears at the true radius of 7.5 cm and the outer ring appears at the correct value of 13 cm.

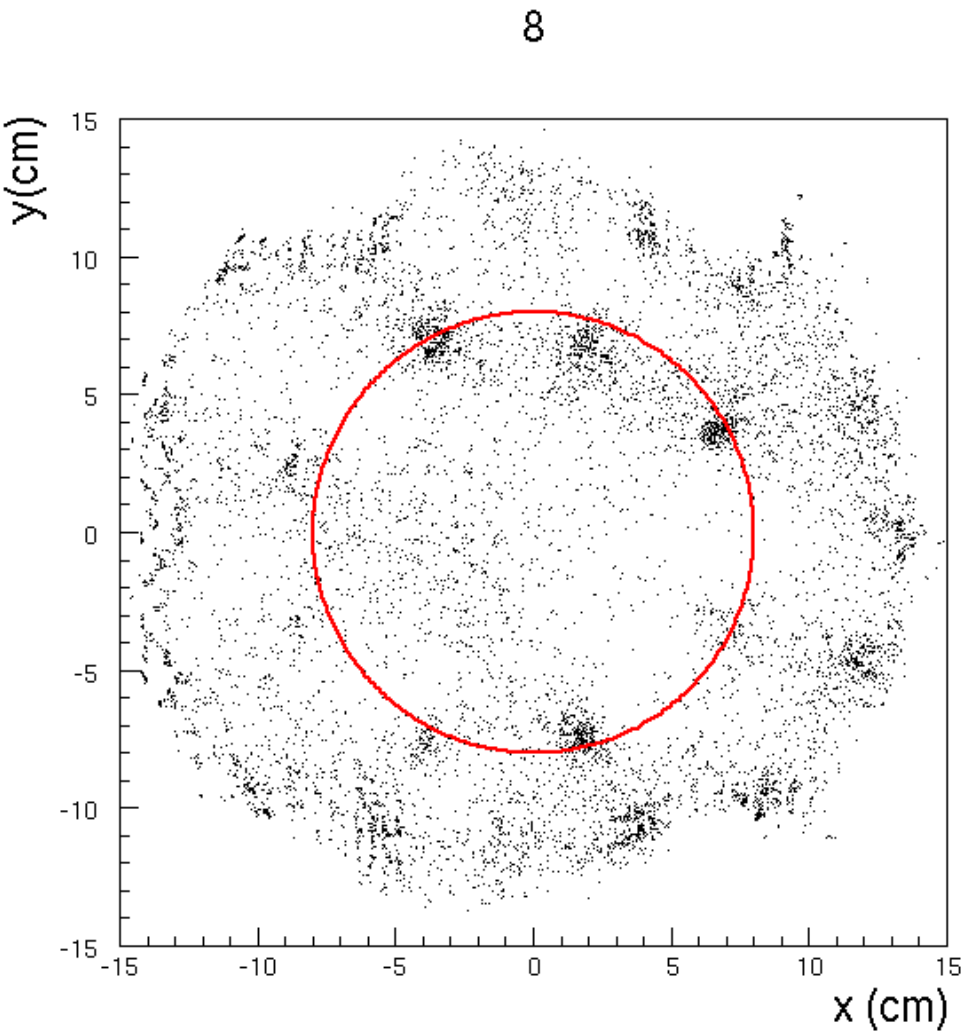

Figure 39: Position reconstruction of ^{57}Co γ-rays, showing the pits in the copper base plate that allow the γ-rays to enter the sensitive volume in the radius of 7.5 cm.

A comparison of the xy positions reconstructed with the χ^2 and weighted methods of events in the golden data are shown in Fig. 40. Note that the actual circular geometry is mapped into a hexagon as was observed in the MC generated data (Fig. 38).

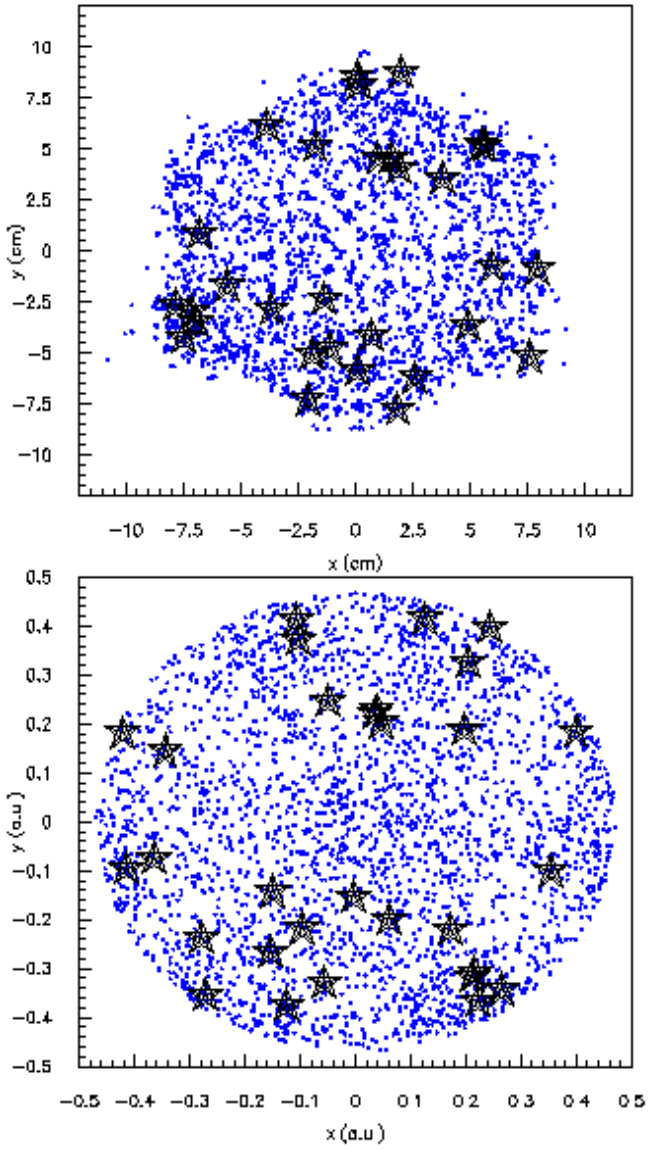

Figure 40: Event position mapping from the single weight method (bottom) to the χ^2 method (top). The black enlarged stars are events that passed all the cuts including the radial cut: $\sqrt{x_w^2 + y_w^2}$ <0.467.

According to the relation of r_w and $r_{\chi 2}$ (Fig. 41), the radial cut $r_w = \sqrt{x_w^2 + y_w^2}$ <0.467 a.u. corresponds to the inner circle of holes in the base plate of radius 8.3 cm (Fig. 42).

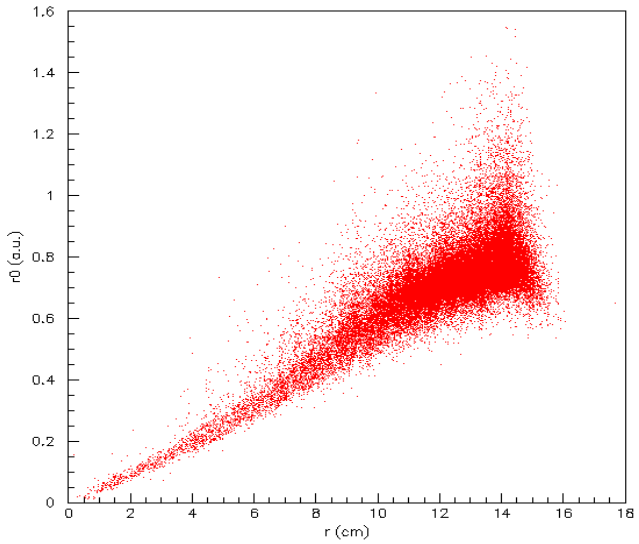

Figure 41: The correlation between $r_{\chi 2}$, reconstructed from the χ^2 method versus r_w, reconstructed from the weighted method.

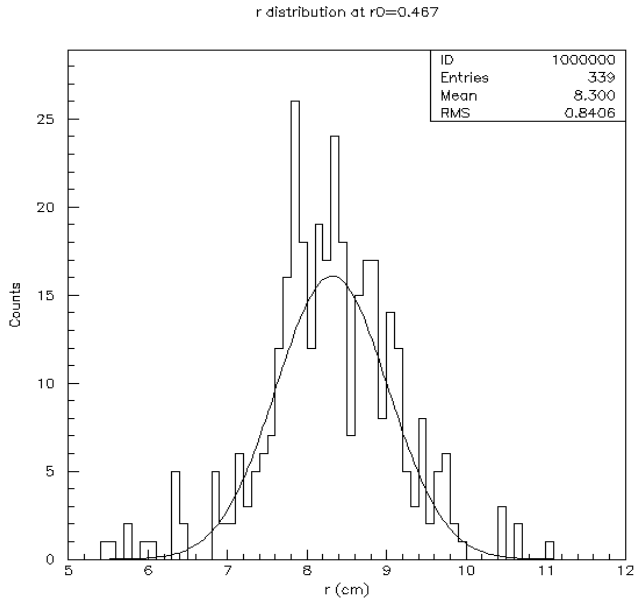

Figure 42: r_w slice of r_{χ^2} - r_w distribution shown in Fig. 41 at the range of -0.01<r_w-0.467<0.01.

Table IX: Change of number of events based on two different radial cuts.

MC run #	Removed events (r >8 cm and r_0<0.467) (Evt ID, scaned)	Added events (r_0>0.467 and r <8 cm) (Evt. ID, scaned)	Number of events removed	Number of events added
33	6837, 21832, 30742, 34830	3638,4049,5984, 10428, 35886,37887, 38439, 46098	4	8
55	6837, 12436, 18112, 21832, 30742, 45674	15209, 18360, 37876, 46098	6	4
71	6837, 12855, 18112, 21832, 30742, 40823, 45674	4049, 18360, 37887, 46098	7	4
72	6837, 12436, 18112, 21832, 30742, 40823	4049, 18360, 37887, 46098	6	4
32	6837, 12436, 18112, 21832, 30742, 45674	15209, 18360, 37876, 46098	6	4
42	6837, 7876, 18112, 21832, 30742, 34830	4049, 15209, 18360, 37887, 46098	6	5
43	6837, 7876,, 21832, 30742,, 34830, 45674	3638, 4049, 5984, 10428, 18360, 20170	6	6
52	6837, 7876,12855, 18112, 21832, 30742	3638, 4049, 18360, 20170, 30470, 46098	6	6
53	6837, 7876, 18112, 21832, 30742	3200, 3638, 15209, 19575, 37887, 46098	5	6
51	6837, 18112, 21832, 30742, 40823	3200, 4049, 5984, 15209, 18360, 46098	5	6

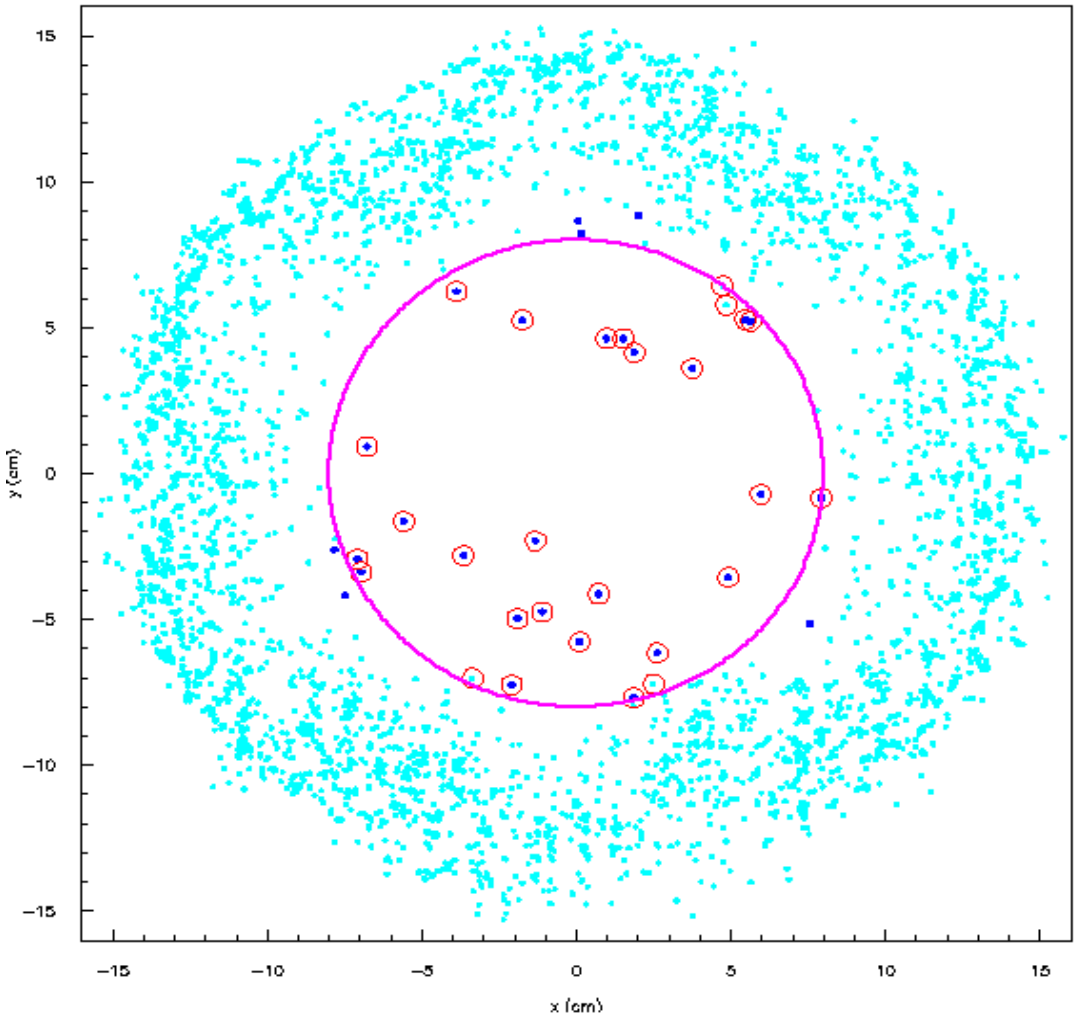

Figure 43: Position distribution of the golden data based on χ^2 method. With the new xy, 6 events are removed while 4 events are added by the fiducial cut r<8cm.

An individual event satisfying r_w<0.467 does not necessarily obey $r_{\chi 2}$ <8 cm, because the mapping is distorted. Table IX shows the number of events that moved in and out of the fiducial radius using the ten best parameterss as listed in Table VIII (in the same order).

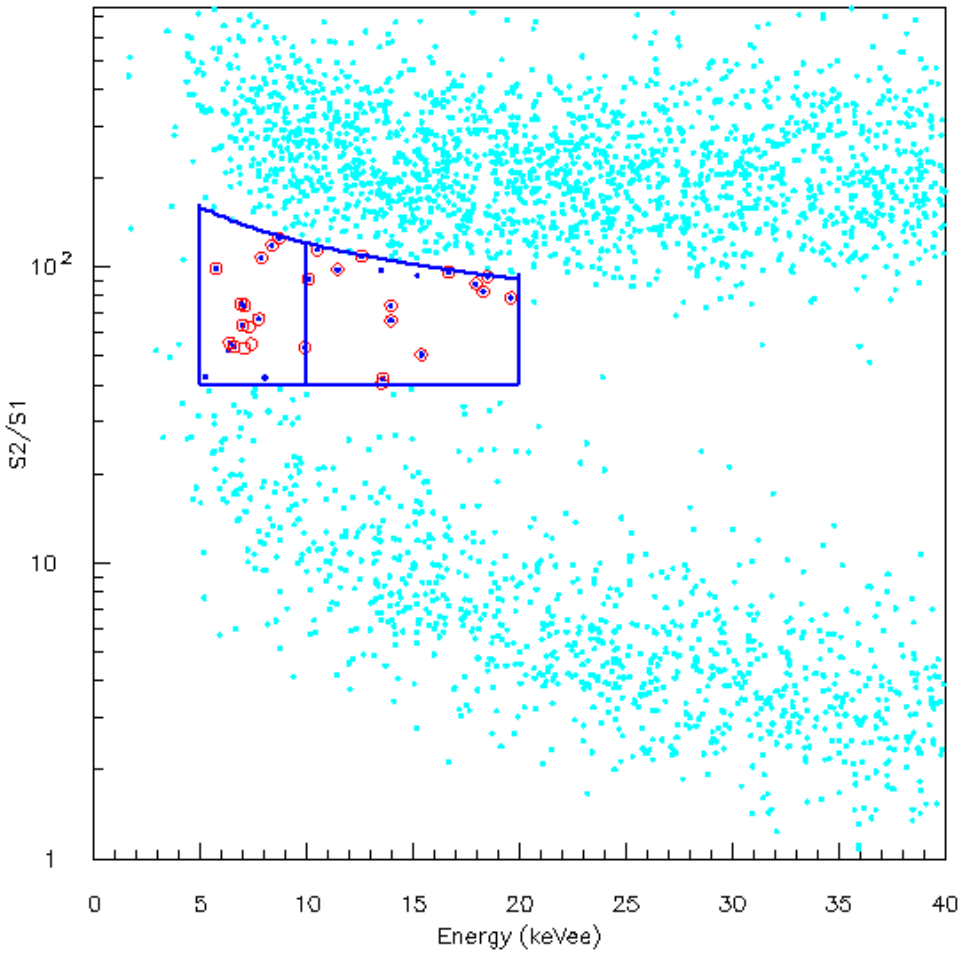

Figure 44: Golden data with the acceptance window. The red diamonds are events with fiducial cut $r_{\chi 2}$ < 8 cm, while the blue dots are events with r_w<0.467.

For the simulation using PTFE total reflectivity 0.9 (for all PTFE parts, including the cone, the bottom plate, the ring ,and the top baffle), cathode transmission 0.6, and 80% diffusive reflectivity, the x y distribution along with the radial cut at 8.3 cm is shown in Fig. 43. The dataset in the acceptance window is shown in Fig. 44.

As can be seen, the events in the box appear to be leakage from the γ-band and from the low S2 band. Expectation calculations for these two populations yield a prediction of 28.6±4.3 background events in the box. From the observed and expected background event count given in Table X, a WIMP nucleon cross-section upper limit can be derived using the Feldman-Cousins method [92]. Following the standard WIMP-nucleon cross-section limit setting procedure of Smith [93] (A brief description of the calculation process is in Appendix B), the spin-independent limits are shown in Fig 45 using both the weighted x,y fiducial volume and for parameter set 55 (in Table VIII) using the new χ^2 method. As can be seen in Table IX, the number of events in the fiducial volume increase or decrease very slightly depending on the set of parameters, and this illustrates that the improved position resolution does not significantly change the original result.

Table X: Overall expectation values in the NR acceptance window compared to observed events.

Energy Range	Observed	γ-ray(^{60}Co) (1)	γ-ray (data)	Rn-initiated (2)	Total(1+2)
5-10 keV_{ee}	16	4.2±2.4	5.6±4.6	10.2±2.2	14.4±3.3
10-20 keV_{ee}	13	11.9±2.7	13.0±6.0	2.3±0.5	14.2±2.7

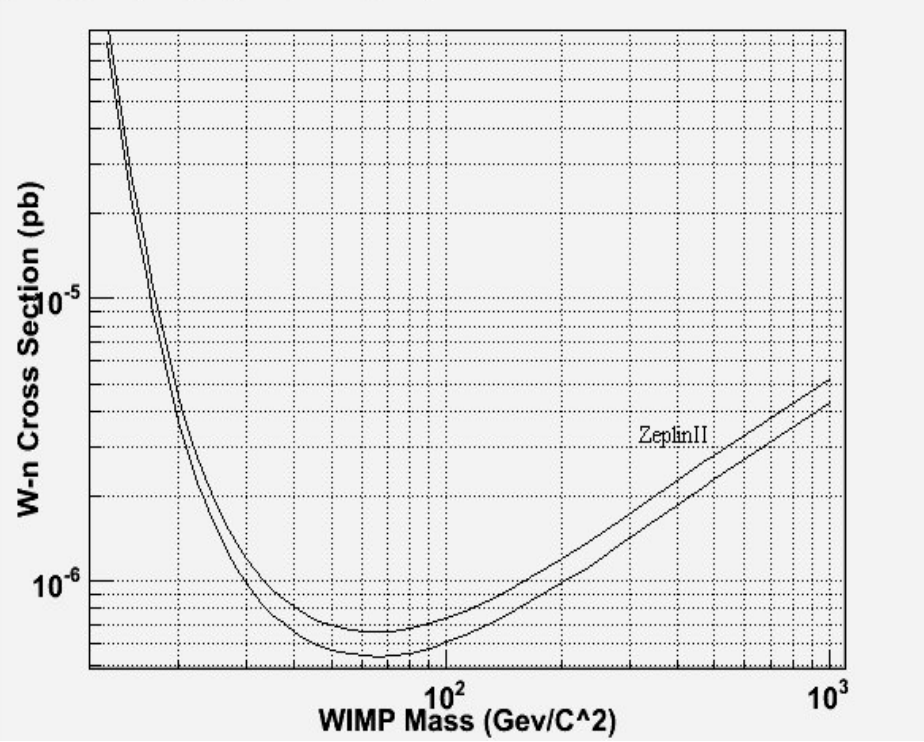

Figure 45: The 90% CL upper limit on the cross-section of WIMP-nucleon spin independent interactions. Also shown is the published ZEPLIN II limit (upper curve).

B. Discussion of the Wall Events

The hypothesis that the population of events in the low S2 band shown in Fig. 29 and Fig. 44 originated from radon nuclei decay on the surface of the walls can now be investigated. As mentioned, these events were thought to be wrongly placed in the fiducial volume due to poor xy reconstruction. However, as can be seen from the correlation between $r_{\chi 2}$ and r_w in Fig. 41, it appears the events are not all wall events.

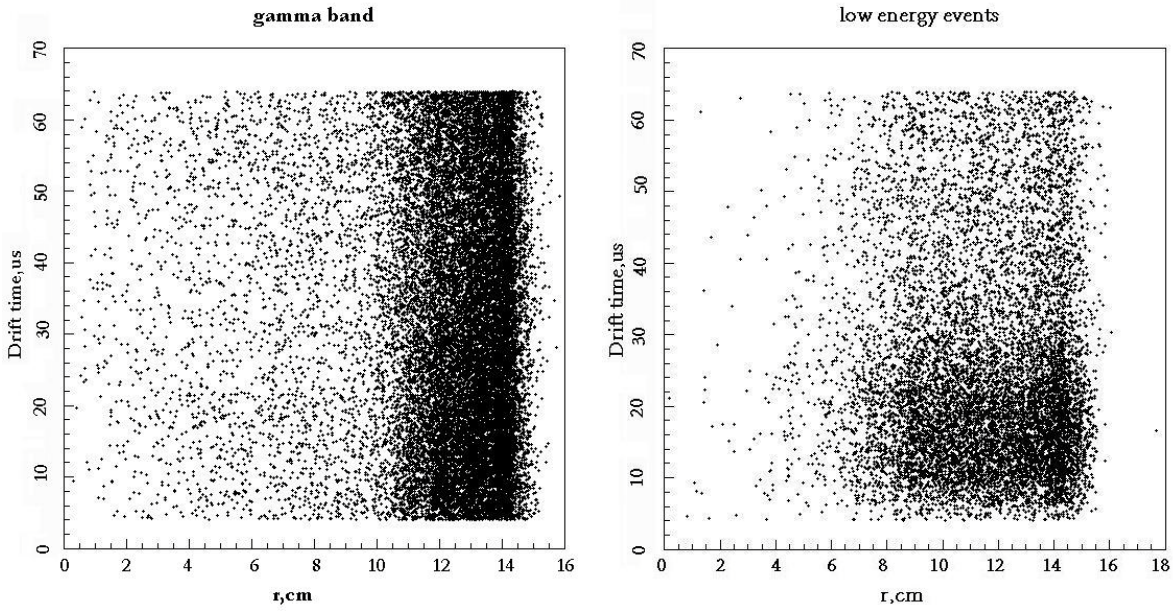

(a) (b)

Figure 46: Scatter plot of drift time vs $r_{\chi 2}$ for (a) gamma events and (b) low energy NR-like events. (a) shows an uniform distribution in drift time but (b) shows a large population at short drift time.

As can be seen in Fig. 46, events in the γ-band are evenly distributed in z (drift time), but events in the low S2 band are more dense with drift times < 30 μs. These events appear to be due to background gamma interactions in the gas between the anode grid and the PMTs as shown in Fig. 47. A study with a gaseous xenon 7-PMT prototype shows that interactions in the region above the anode grid can produce secondary light if the ionized electrons diffuse to the high field region near the wires of the anode grid [94]. These events have large S1 and small S2 as shown in Fig. 48.

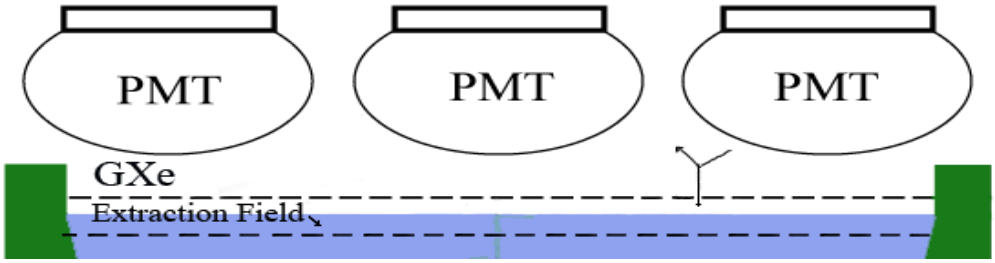

Figure 47: An example of gamma event above the anode grid. The electric field between the PMTs and the anode is close to zero, but the ionization electrons can diffuse to the anode with a characteristic time <~ 30 μs.

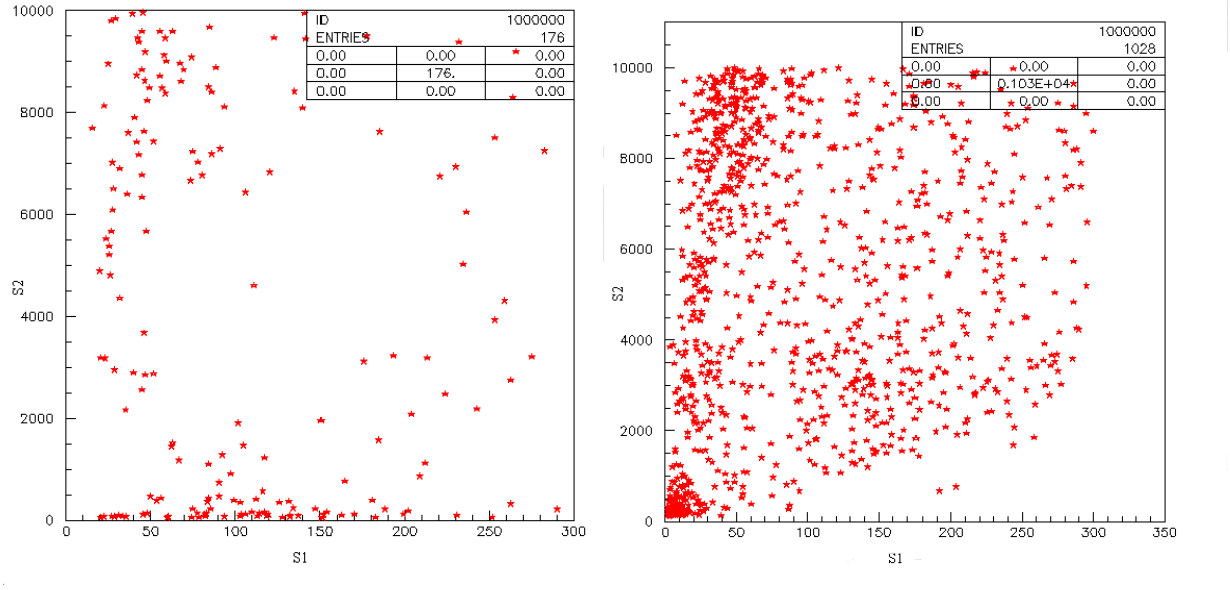

(a) (b)

Figure 48: Scatter plot of S2 vs S1 for events from a 7-PMT gaseous xenon prototype with an AmBe source. The voltage of the top grid is at ground (0V) in figure (a). There are a few events with small S2 and large S1. When the voltage of the top grid is -200 V, this group of events disappear (b). This shows they are events are from the region above the top grid.

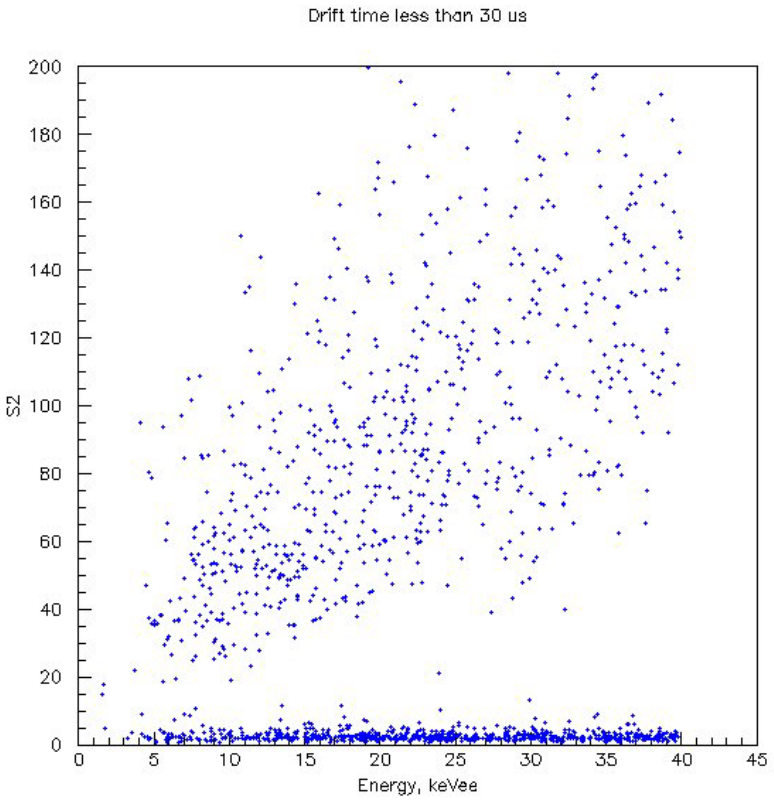

Figure 49: Scatter plot of S2 vs S1 for the ZEPLIN II events in the low energy band with drift time smaller than 30 μs. The events with small S2 and large S1 are events in the gas above the anode.

The scatter plot of S2 versus S1 for the ZEPLIN II events of the low energy band near the grids is shown in Fig. 49. Again, the population of events with very low S2 have small drift time and are mostly gamma events in the gas above the anode as in Fig. 48 (a).

C. Conclusions

ZEPLIN II was the world's first dark matter search experiment to employ the two-phase xenon approach. A number of critical technical issues were identified and solved, and the world's first limit using this approach was produced.

In this dissertation, optical properties of the PTFE parts and the grids of the ZEPLIN II detector were investigated by simulation. Based on the amount of light reaching the different PMTs as a function of event position, an improved x y position determination using a χ^2 approach was developed. The best χ^2 distributions are achieved for a reduced light reflectivity on the PTFE rings near the surface of the liquid xenon and the PTFE baffle surrounding the PMTs.

The number of events in the box were seen to fluctuate slightly up and down depending on the parameter set, so new limits using the improved x y positioning are consistent with the original result. The significant finding is that the events in the bottom of the box from the low S2 band are not in the fiducial volume because they are poorly reconstructed but are from a different source. Therefore the hypothesis that they are wall events is incorrect.

An investigation of the source of the low S2 events revealed that they are mostly due to interactions in the gas above the anode. Such events can be eliminated with a choice of voltage settings that repel electrons above the anode.

REFERENCES

[1] D. Clowe, A. Gonzalez, and M. Markevitch, Astrophys. J. **604**, 596 (2004).

[2] C. L. Sarazin, *X-Ray Emission from Clusters of Galaxies* (Cambridge University Press, Cambridge 1988).

[3] M. Girardi, G. Giuricin, F. Mardirossian, M. Mezzetti, and W. Boschin, Astrophys. J. **505**, 74 (1998).

[4] D. A. White, C. Jones, and W. Forman, Mon. Not. R. Astron. Soc. **292**, 419 (1997).

[5] V.C. Rubin, N. Thonnard, and W. K. Ford, Astrophys. J. **238**, 471(1980).

[6] A. Bosma, Astron. J. **86**, 1825 (1981).

[7] S.M. Faber and J.S. Gallagher, Ann. Rev. Astron. Astrophys. **17**,135 (1979).

[8] M. Persic, P. Salucci, and F. Stel, Mon. Not. R. Astron. Soc. **281**, 27 (1996).

[9] M. Lowewnstein and R. E. White, Astrophys. J. **518**, 50 (1999).

[10] D. P. Clemens, Astrophys. J. **295**, 422 (1985).

[11] M. J. Geller and J. P. Huchra, Science **246,** 897 (1989).

[12] G. F. Smoot, C. L. Bennett, A. Kogut, E. L. Wright, and J. Aymon *et al.*, Astrophys. J. **396,** L1 (1992).

[13] C. L. Bennett, A. Banday, K. M. Gorski, G. Hinshaw, and P. Jackson *et al.*, Astrophys. J. **464,** L1 (1996).

[14] E. F. Bunn and M. White, Astrophys. J. **480,** 6 (1997).

[15] C.L Bennett, M. Halpern, G. Hinshaw, N. Jarosik, A. Kogut *et al.*, Astrophys. J. Suppl. Ser. **148,** 1 (2003).

[16] A. Jenkins, C. S. Frenk, F. R. Pearce, P. A. Thomas, J. M. Colberg *et al.*, Astrophys. J. **499,** 20 (1998).

[17] M. Kamionkowski and D. N. Spergel, Astrophys. J. **432,** 7 (1994) .

[18] C. Alcock, R. A. Allsman, D. R. Alves, T. S. Axelrod, A. C. Becker *et al.*, Astrophys. J. **541,** 734 (2000).

[19] F. H. Shu, *The Physical Universe: An Introduction to Astronomy* (University Science Books, Mill Valley, CA, 1982).

[20] J. C. Mather, E. S. Cheng, R. A. Shafer, C. L. Bennett, and N. W. Boggess *et al.*, Astrophys. J. **354,** L37 (1990).

[21] D. N. Spergel, L. Verde, H. V. Peiris, E. Komatsu, M. R. Nolta *et al*., Astrophys. J. Suppl. Ser. **148**, 175 (2003).

[22] S. Weinberg, Phys. Rev. Lett. **40,** 223(1978); F. Wilczek, Phys. Rev. Lett. **40,** 279 (1978).

[23] H. Peng, S. Asztalos, E. Daw, N. A. Golubev, C. Hagmann *et al*., Nucl. Instrum. & Methods **A444**, 569 (1999).

[24] S. J. Asztalos, Phys. Rev. D **69**, 011101(R) (2004).

[25] M. Fich and S. Tremaine, Ann. Rev. Astron. Astrophys **29,** 405 (1991).

[26] A. M. Green, Phys. Rev. D **66**, 083003 (2002).

[27] G. Jungman, M. Kamionkowski, and K. Griest, Phys. Rep. **267,** 195 (1996).

[28] J. Engel, Phys. Lett. B **264**, 114 (1991).

[29] J.G. Learned and K. Mannheim, Annu. Rev. Nucl. Part. Sci. **50**, 679 (2000).

[30] M.M. Boliev, E.V. Bugaev, A.V. Butkevich, A.E. Chudakov, S.P. Mikheyev *et al*. (BAKSAN Collaboration), Nucl. Phys. B (Proc. Suppl.) **48**, 83 (1996).

[31] M. Ambrosio, R. Antolini, C. Aramo, G. Auriemma, A. Baldini *et al*. (MACRO Collaboration), Phys. Rev. D **60**, 082002 (1999).

[32] S. Desai, Y. Ashie, S. Fukuda, K. Ishihara, Y. Itow *et al*. (Super-Kamiokande Collaboration), Phys. Rev. D **70**, 083523 (2004).

[33] M. Ackermann, J. Ahrens, X. Bai, M. Bartelt, S.W. Barwick *et al.* (The AMANDA Collaboration), Astropart. Phys. **24**, 459 (2006).

[34] A. Cesarini, F. Fucito, A. Lionetto, A. Morselli, and P. Ullio, Astropart. Phys. **21,** 267 (2004).

[35] G. Zaharijas and D. Hooper, Phys. Rev. D **73**, 103501 (2006).

[36] Y. Asaoka, Y. Shikaze, K. Abe, K. Anraku, M. Fujikawa *et al.*, Phys. Rev. Lett. **88**, 051101 (2002).

[37] S. Coutu, S. W. Barwick, J. J. Beatty, A. Bhattacharyya, C. R. Bower *et al.*, Astropart. Phys. **11**, 429 (1999).

[38] S. R. Golwala, Ph.D. dissertation, University of California, Berkeley, 2000 (http://cdms.berkeley.edu/Dissertations/).

[39] R. Bernabei, P. Belli, F. Cappella, R. Cerulli, F. Montecchia *et al.*, Riv. Nuovo Cim., **26**, 1 (2003).

[40] D. S. Akerib, M. S. Armel-Funkhouser, M. J. Attisha, C. N. Bailey, L. Baudis *et al*. (CDMS Collaboration), Phys. Rev. D **72**, 052009 (2005).

[41] C. Copi and L. Krauss, Phys. Rev. D **67**, 103507 (2003).

[42] A. Benoit, L. Bergé, A. Broniatowski, B. Chambon, M. Chapellier *et al.* (EDELWEISS Collaboration), Phys. Lett. B **513**, 15 (2001).

[43] A. Benoit, L. Bergé, A. Broniatowski, B. Chambon, M. Chapellier *et al.* (EDELWEISS Collaboration), Phys. Lett. B **545**, 43 (2002).

[44] D. Cline, Y. Seo, F. Sergiampietri, H. Wang, J. T. White *et al.* (ZEPLIN Collaboration), in *Proceedings of 4th International Workshop on Identification of Dark Matter, York, England 2002*, edited by N. J. C. Spooner (World Sci., Singapore, 2003), p.302.

[45] G. Angloher, C. Bucci, P. Christ, C. Cozzini, F. von Feilitzsch *et al.*, Astropart. Phys. **23**, 325 (2005).

[46] E. Aprile, K. L. Giboni, P. Majewski, K. Ni, M. Yamashita *et al*, New Astro. Rev. **49**, 289 (2005).

[47] J. Angle, E. Aprile, F. Arneodo, L. Baudis, A. Bernstein *et al.* (XENON Collaboration), Phys. Rev. Lett. **100**, 021303 (2008).

[48] P. Benetti, E. Calligarich, R. Dolfini, A. Gigli Berzolari, F. Mauri *et al.*, Nucl. Instrum. & Methods A **327**, 203 (1993).

[49] P. Benetti, A. Bettini, E. Calligarich, F. Casagrande, P. Casoli *et al.*, Nucl. Instrum. & Methods A **329**, 361 (1993).

[50] D. Cline, A. Curioni, A. Lamarina, G. Mannocchi, S. Otwinowski *et al.*, Astropart. Phys. **12**, 373 (2000).

[51] F. Arneodo, B. Baiboussinov, A. Badertscher, P. Benetti, E. Bernardini *et al.*, Nucl. Instrum. & Methods A **449,** 147 (2000).

[52] D. R. Lide, *Handbook of Chemistry and Physics,* 85th edition (CRC Press, Boca Raton, FL, 2004).

[53] V. A. Rabinovich and T. B. Selover, *Thermophysical Properties of Neon,Aargon, Krypton, and Xenon* (Hemisphere Publ. Corp., Washington, DC, 1988).

[54] M. Miyajima, S. Sasaki, and H. Tawara, IEEE Trans. Nucl. Sci. **41**, 835 (1994).

[55] M. J. Terry, J. T. Lynch, M. Bunclark, R. K. Mansell, and L. A. K. Staveley, J. Chem. Thermodynamics **1**, 413 (1969).

[56] A. J. Leadbetter and H. E. Thomas, Trans. Faraday Soc. **61**, 10 (1965).

[57] W. B. Streett, L. S. Sagan, and L. A. L. Staveley, J. Chem. Thermodynamics **5**, 633 (1973).

[58] F. Theeuwes and R. J. Bearman, J. Chem. Thermodynamics **2**, 507 (1970).

[59] L.M. Barkov, A. A. Grebenuk, N. M. Ryskulov, P. Yu. Stepanov, and S. G. Zverev, Nucl. Instrum. & Methods A **379**, 482 (1996).

[60] V. N. Solotov, V. Chepel, M. I. Lopes, A. Hitachi, R. Ferreira Marques *et al.*, Nucl. Instrum. & Methods A **516**, 462 (2004).

[61] J. H. Hubbell and S. M. Seltzer, *Tables of X-Ray Mass Attenuation Coefficients and Mass Energy-Absorption Coefficients* (version 1.4, National Institute of Standards and Technology, Gaithersburg, MD, 2004).

[62] T. Doke, Port. Phys., **12**, 9 (1981).

[63] J. Seguinot, J. Tischhauser, and T. Ypsilantis, Nucl. Instrum. & Methods A **354**, 280 (1995).

[64] T. Doke and K. Masuda, Nucl. Instrum. & Methods A **420**, 62 (1999).

[65] J. Lindhard, V. Nielsen, M. Scharff, and P. V. Thomsen, Mat. Fys. Medd. Dan. Vid. Selsk. **33**, 10 (1963).

[66] R.Bernabei, P. Belli, F. Montecchia, A. Incicchitti, D. Prosperi *et al*., Phys.Lett.B **436**, 379 (1998).

[67] F.Arneodo, B. Baiboussinov, A. Badertscher, P. Benetti, E. Bernardini *et al*., NIM A **449**, 147 (2000).

[68] D. Akimov, A. Bewick, D. Davidge, J. Dawson, A. S. Howard *et al.*, Phys. Lett. B **524**, 245 (2002).

[69] E. Aprile, K. L. Giboni, P. Majewski, K. Ni, M. Yamashita *et al.*, Phys. Rev. D **72**, 072006 (2005).

[70] V. Chepel, V. Solovov, F. Neves, A. Pereira, P.J. Mendes *et al.*, Astropart. Phys. **26**, 58 (2006).

[71] E. Aprile, R. Mukherjee, and M. Suzuki, Nucl. Instrum. & Methods A **307**, 119 (1991).

[72] E. Aprile, C. E. Dahl, L. de Viveiros, R. J. Gaitskell, K. L. Giboni *et al.*, Phys. Rev. Lett. **97**, 081302 (2006).

[73] A Baldini, C. Bemporad, F. Cei, T. Doke, M. Grassi *et al.*, Nucl. Instrum. & Methods A **545**, 753 (2005).

[74] U. Rossier, Phys. Status Solidi B **42,** 345 (1970), B **45,** 483 (1971).

[75] G. Keitel, Ph.D. thesis, University of Hamburg, Deutsches Elektronen-Synchrotron DESY, DESY Internal Report F41-70/7, 1970 (unpublished) P. Schreber, Ph.D. thesis, University of Hamburg, Deutsches Elektronen-Synchrotron DESY, DESY Internal Report F41-70/5, 1970 (unpublished).

[76] R.L. Platzman, Int. J. Appl. Rad. Isotopes, **10**, 116 (1961).

[77] T. Takahashi, S. Konno, T. Hamada, M. Miyajima, S. Kubota *et al.* Phys. Rev. A **12**, 1771 (1975).

[78] L.S. Miller, S. Howe, and W.E. Spear, Phys. Rev. **166**, 871 (1968).

[79] E. Shibamura, S. Kubota, T. Takahashi and T. Doke, in *Proceedings of the International Seminar on Swarm Experiments in Atomic Collision Research, Tokyo, 1979*, edited by I. Ogawa (Rikkyo University, Tokyo, 1979), p. 47.

[80] A.I. Bolozdynya, Nucl. Instrum. & Methods A **422**, 314 (1999).

[81] E. Aprile, K. L. Giboni, P. Majewski, K. Ni, and M. Yamashita, IEEE Trans. Nucl. Sci. **51**, 1986 (2004).

[82] Model Ha4 7TA Electron Tubes Inc., Ruislip, U.K.

[83] Measurement Systems Ltd., http://www.msl-datascan.com/

[84] Acqiris Corporation, *Acqiris Digitizers User Manual* (Version 1.22, Acqiris Corporation, Monroe, NY, 2000).

[85] R. Luscher, S. P. Hart, M. J. Lehner, M. Robinson and M. J. Carson, *The CompactPCI Daq User Guide*, ZEPLINII Internal Memo, 2005, (unpublished).

[86] G. J. Alner, H.M. Araújo, A. Bewick, C. Bungau, B. Camanzi *et al*. (ZEPLIN II Collaboration), ZEPLIN II Finalcuts Note, 2007, (unpublished).

[87] G. J. Alner, H.M. Araújo, A. Bewick, C. Bungau, B. Camanzi *et al*. (ZEPLIN II Collaboration), Astropart. Phys. **28**, 287 (2007).

[88] Geant4 Collaboration, Nucl. Instrum. & Methods A **506**, 250 (2003).

[89] V.R. Weidner and J.J. Hsia, J. Opt. Soc. Am. **71**, 856 (1981).

[90] M. Miyajima, S. Sasaki, and E. Shibamura, Nucl. Instrum. & Methods B **63**, 297 (1992).

[91] A. Levin and C. Moisan, in *Proceedings of IEEE, Anaheim, CA,1996,* Nuclear Science Symposium (Institute of Electrical &Electronics Enginee, Anaheim, 1996), p. 702.

[92] G.J. Feldman and R.D. Cousins, Phys. Rev. D**57**, 3873 (1998).

[93] J.D. Lewin and P.F. Smith, Astropart. Phys. **6**, 87 (1996).

[94] J. T. White and H. Wang, ZEPLIN II Report No. DRep005a, 2005 (unpublished).

APPENDIX A

LIST OF WIMP CANDIDATE EVENTS

Table A1: List of ZEPLINII WIMP candidate events

ID	Event (Golden)	Eventide	S2/S1	Energy (keV_{ee})	Dtime (μs)	x_w	y_y
1	51162	6052000270566	114.7	10.47	38.19	-0.345	0.147
2	80899	6052100370509	97.7	13.49	24.19	0.221	-0.364
3	96259	6052200251823	91.3	10.07	15.98	-0.154	-0.265
4	122719	6052300400384	96.1	16.67	33.02	0.0340	0.225
5	155472	6052500580706	42.3	8.03	22.33	0.204	0.328
6	163076	6052600170552	50.6	15.38	35.2	-0.108	0.416
7	170690	6052600370592	74.9	6.88	51.57	-0.104	0.373
8	192510	6052700400364	74.3	7.08	56.76	0.045	0.205
9	220171	6052800481657	54.0	6.57	33.34	-0.002	-0.149
10	243785	6052900421504	109.01	12.55	44.94	0.216	-0.306
11	252592	6060100091386	52.5	6.32	18.74	0.126	0.418
12	260517	6060100321229	42.0	13.57	55.09	-0.056	-0.327
13	307568	6060500401659	53.4	9.89	52.48	-0.150	-0.141
14	327491	6060600340420	97.1	16.65	15.84	0.265	-0.341
15	377762	6061701081667	98.3	11.44	10.38	0.399	0.185
16	380500	6061701301281	118.6	8.35	45.65	0.061	-0.196
17	393175	6061801000759	98.6	5.71	55.79	-0.051	0.248
18	433449	6062000671853	78.7	19.59	35.95	0.353	-0.099
19	446145	6062100191228	93.7	15.19	13.36	0.244	0.397
20	473595	6062200621971	74.1	13.94	47.19	-0.280	-0.234
21	500369	6062300881437	66.9	7.75	6.63	-0.123	-0.373
22	502289	6062300961460	63.6	6.99	18.67	0.209	-0.315
23	514583	6062400540083	87.8	17.95	58.72	0.038	0.229
24	546219	6062900060780	107.6	7.84	45.13	0.195	0.192
25	584474	6063000571271	125.6	8.68	53.92	-0.097	-0.216
26	594508	6070100110234	82.4	18.28	51.74	-0.272	-0.351
27	597751	6070100220370	55.6	6.37	17.36	-0.413	-0.093
28	671674	6070700341464	42.5	5.24	58.48	-0.366	-0.073
29	696944	6070600570981	92.8	18.49	34.60	0.171	-0.219

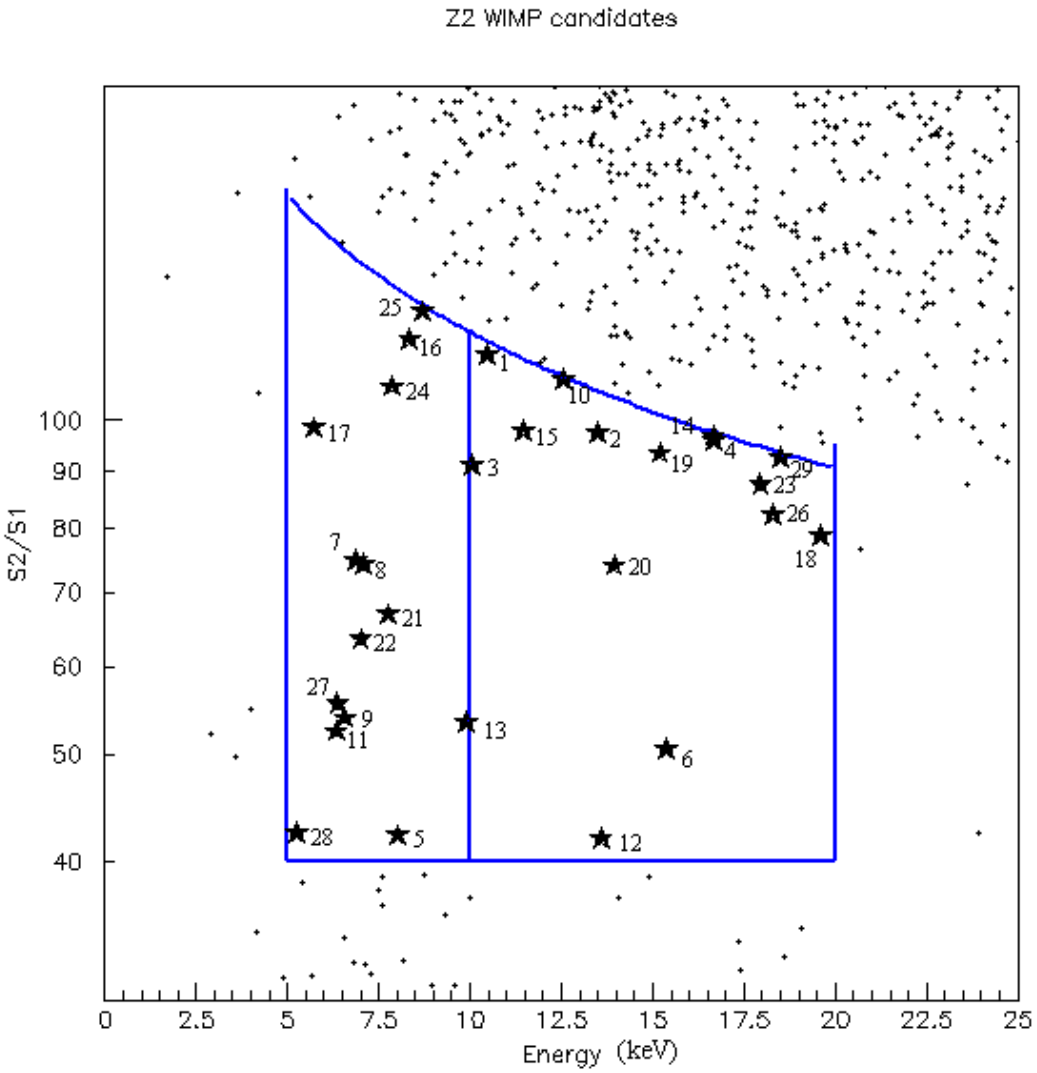

Figure A.1 ZEPLIN II WIMP candidate events. The numbers represent the event ID listed in Table A.1.

APPENDIX B

PROCEDURE OF LIMIT CALCULATION

A. Data and Cuts Used

Data and cuts used are discussed in Chapter IV.

B. Conversion to Spreadsheet form

Events are binned in the quantities S1 photoelectrons and log(S2/S1). The S1 bins are in intervals 0-1 to interval 99-100. The log(S2/S1) bins are in intervals 0.1 from interval 0-0.1 to interval 2.9-3.0

C. Shape of S2/S1 Distribution

Define r = log(S2/S1). The distribution of dN/dr can be parameterized by dN/dr = exp(ar)/[1+c exp((a+b) r)] with a normalizing factor to the total number of events. Define the peak position $r_p = [1/(a+b)]\ln(a/bc)$, then

$$dN/dr = \exp(ar)/[1+(a/b)\exp(a+b)(r-r_p)] \quad (1)$$

The distribution is characterized by r_p, the peak position, a, the initial exponential rise, and b, the final exponential fall.

The ratio of b/a can be determined by fitting to gamma and AmBe data. The Ambe distribution can be fitted by two distributions with the same a and b, but different peak positions.

D. Mean Signal and 90% Confidence Limit

For each pe range, one determines the position of the gamma peak in the data and multiply by the ratio of the neutron and gamma peaks, this provides the expected position of a nuclear recoil peak. The most probable amplitude can be obtained for a

signal shaped as eq. (1). Since the overlap of the distribution of gammas and neutrons is large, the analysis is in Gaussian regime rather than Poisson. A sensitivity estimate is obtained by integrating the events N up to an optimum value of log(S2/S1), and taking the one-sided 90% confidence limit to be $1.3N^{1/2}$. The resulting event limits for different pe ranges are converted into event limits in keV ranges. The energy intervals are chosen in order to group the data into wider ranges as energy increases. These event limits can be converted to limits on the dark matter rate and hence cross section as a function of dark matter particle mass. At this stage matrices can be applied to the column vector of theoretical spectral terms to allow for mixing between energy bins through the energy resolution. The position-dependent light collection is assumed to be unit matrix based on ZEPLIN II simulations. The rebinning matrix can be calculated based on the energy resolution of $\pm 1.8E^{1/2}$. The above information is now sufficient to obtain a limit on nuclear recoil rate, and the WIMP-nucleon cross-section as a function of WIMP mass for each energy range by following the procedure set out in §9 in the ZEPLIN I paper (Astropart. Phys. 23, 444(2005).)

VITA

Name: Jianting Gao

Address: Nanfei Quarters, Section 8, Building 43, Unit 3, 602
Nanchang, Jiangxi, 330024, China

Email Address: gaojianting@gmail.com

Education: B.S., Physics, Nanjing University, Nanjing, China, 1997
M.S., Physics, Institute of High Energy Physics, Chinese Academy of Sciences, Beijing, China, 2000